Characterisation of L-band Differential Low Noise Amplifiers

by

David Schalk Van der Merwe Prinsloo

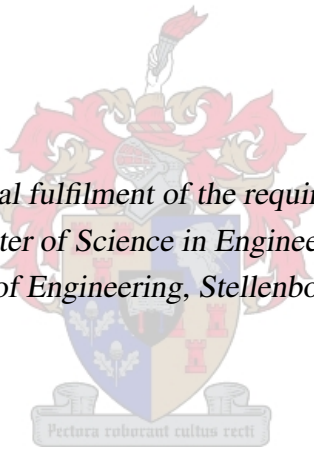

Thesis presented in partial fulfilment of the requirements for the degree of
Master of Science in Engineering
at the Faculty of Engineering, Stellenbosch University

Supervisors:

Prof. Petrie Meyer
Department of Electrical and Electronic Engineering

Dr. Dirk de Villiers
Department of Electrical and Electronic Engineering

December 2011

Declaration

By submitting this thesis electronically, I declare that the entirety of the work contained therein is my own, original work, that I am the sole author thereof (save to the extent explicitly otherwise stated), that reproduction and publication thereof by Stellenbosch University will not infringe any third party rights and that I have not previously in its entirety or in part submitted it for obtaining any qualification.

Date: December 2011

Abstract

Keywords - Noise, Noise Parameters, Correlation Matrix, Scattering Parameters, Multi-port Network, Mixed-mode, Hybrid Coupler , Differential Low Noise Amplifier (dLNA), Low Noise Amplifier (LNA), Noise measurement, Differential Noise Figure, Noise Figure.

This thesis addresses the complications that are encountered when characterising the performance of differential microwave LNAs. The predominant sources of noise in electronic circuits are introduced and equivalent two-port noise models for active devices are derived. Correlation between noise generators are defined by means of the noise correlation matrix and existing network theory is adapted to include noise analysis of two-port and multi-port networks. Mixed-mode scattering parameters are introduced in order to define the signal performance of differential and common-mode propagation in multi-port networks and, by applying the same theory, the mixed-mode correlation matrix for a three-port dLNA is derived. Furthermore, an expression is derived for de-embedding the differential noise figure of a three-port dLNA using two single ended measurements. Two dLNA designs, both incorporating wideband 180°-Hybrid ring couplers, are discussed and the differential signal and noise performance of the dLNAs are compared to that of their constituent single ended LNAs.

Opsomming

Sleutelwoorde - Ruis, Ruisparameters, Korrelasiematriks, S-parameters, Multipoortnetwerke , Gemengde-modus, Differensiaalkoppelaar , Differensiële Laeruis Versterker, Laeruis Versterker, Ruismeting, Differensiäleruissyfer, Ruissyfer.

Hierdie tesis behandel die komplikasies wat ontwerpers in die gesig staar tydens die karakterisering van mikrogolf differensiële laeruis versterkers. Die hoof ruisbronne in stroombane word bespreek en ekwivalente tweepoortnetwerkmodelle vir aktiewe toestelle word afgelei. Korrelasie tussen ruisbronne word gedefnieer deur middel van ruiskorrelasiematrikse en bestaande tweepoort- en multipoort-netwerkteorie word aangepas om ruismodelle in te sluit. Weens die feit dat differensiële- en gemene-wyse voortplanting van seine voorkom in multipoortnetwerke word gemengde-modus S-parameters behandel. Dieselfde teorie maak dit vervolgens moontlik om die gemengde-modus ruiskorrelasiematriks van ’n drie-poort differensiële laeruis versterker af te lei. Verder word daar ’n wyse voorgestel waarmee die differensiëleruissyfer van ’n drie-poort differensiële laeruis versterker vanuit twee enkel ruissyfermetings bereken kan word. Twee differensiële laeruis versterker ontwerpe, waarvan beide wyeband 180°-differensiaalkoppelaars implementeer, word bespreek en die differensiëlesein- asook die differensiëleruis-werking word vergelyk met die werking van die omsluite ongebalanseerde laeruis versterkers.

Acknowledgements

- Prof. Petrie Meyer and Dr. Dirk de Villiers, for their invaluable guidance and advice throughout the project.
- Prof. Keith Palmer and Prof. PW van der Walt, for the insightful discussions during the early stages of the project.
- Wessel Croukamp, Wynand van Eeden and Ashley Cupido, for their patience and expertise that made it possible to bring my designs to life.
- Shamim, Sunelle, Madelé, David, Phillip, and Theunis, for making Van, Werner, Charlie and myself feel right at home in Stellenbosch.
- My parents, for never ceasing to believe in me.
- My brother, for administrating my life when it seemed that I had forgotten how.
- My friends, for keeping my life in balance throughout the project.
- My cousin Rachelle, for helping me keep perspective at all times and celebrating each accomplishment with me.
- The NRF and SKA South Africa for funding this research.

"Like diseases,
noise is never eliminated,
just prevented, cured, or endured,
depending on its nature, seriousness,
and the costs/difficulty of treating it."
- D. H. Sheingold -

Table of Contents

List of Figures

List of Tables

List of Acronyms

ASKAP	Australian Square Kilometer Array Pathfinder
BJT	Bipolar Junction Transistor
CMRR	Common Mode Rejection Ratio
CPW	Coplanar Waveguide
CST	Computer Simulation Technology
DC	Direct Current
dLNA	Differential Low Noise Amplifier
DUT	Device Under Test
EM	Electromagnetic
EMBRACE	Electronic Multi Beam Radio Astronomy ConcEpt
ENR	Excess Noise Ratio
FET	Field Effect Transistor
FGCPW	Finite Ground Coplanar Waveguide
GaAs	Gallium Arsenide
HEMT	High Electron Mobility Transistor
JFET	Junction Field Effect Transistor
LNA	Low Noise Amplifier
LWA	Long Wavelength Array
MESFET	Metal Semiconductor Field Effect Transistor
MOSFET	Metal Oxide Semiconductor Field Effect Transistor
MWA	Murchison Widefield Array

MWO	Microwave Office
NFA	Noise Figure Analyser
PAF	Phased Array Feed
PCB	Printed Circuit Board
pHEMT	pseudomorphic High Electron Mobility Transistor
QFN	Quad-Flat-Non-Lead
RFE	Receiver Front End
S	Scattering
SKA	Square Kilometer Array
SMD	Surface Mount Device
SWR	Standing Wave Ratio
VNA	Vector Network Analyser
WBSPF	Wide-Band Single Pixel Feed

Chapter 1

Introduction

Everything radiates.
Be it a celestial or terrestrial body, all objects emit Electromagnetic (EM) energy that can be defined as either thermal or non-thermal in nature. In order to gain a better understanding of the universe, astronomers study both the thermal and non-thermal EM radiation of celestial bodies. As this radiation is normally at extremely low power levels when it reaches Earth, radio astronomy systems have two critical system parameters which determine their performance, namely receiving area and added noise. Together, these two aspects determine the sensitivity of the receivers, where

$$Sensitivity = \frac{Aperture\ Area}{System\ Temperature} \tag{1.0.1}$$

The proposed Square Kilometer Array (SKA) is intended to have the largest receiving area of any radio telescope in the world. This large collecting aperture is however of little use if the receivers following the antenna adds so much noise that the received signals cannot be identified. To ensure a sensitive system, it is therefore imperative that extremely Low Noise Amplifiers (LNAs) are used in the very first stage of the receiving chain since their noise contribute directly to the system temperature. This thesis focusses on the theory and design of these LNAs.

1.1 Background

1.1.1 SKA Telescope

The SKA telescope will have a total collecting area of approximately one square kilometre and will be able to receive frequencies ranging from 70 MHz up to 10 GHz. In order to observe such a wide band of frequencies, the SKA will comprise of three different antenna types: for the lower frequencies (70 MHz - 300 MHz) a sparse dipole array, for the mid-frequency range (300 MHz-1 GHz) a dense aperture array, and parabolic reflector antennas for the higher frequencies (1 - 10 GHz).

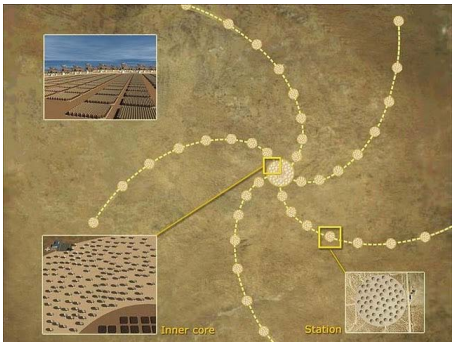

(a)

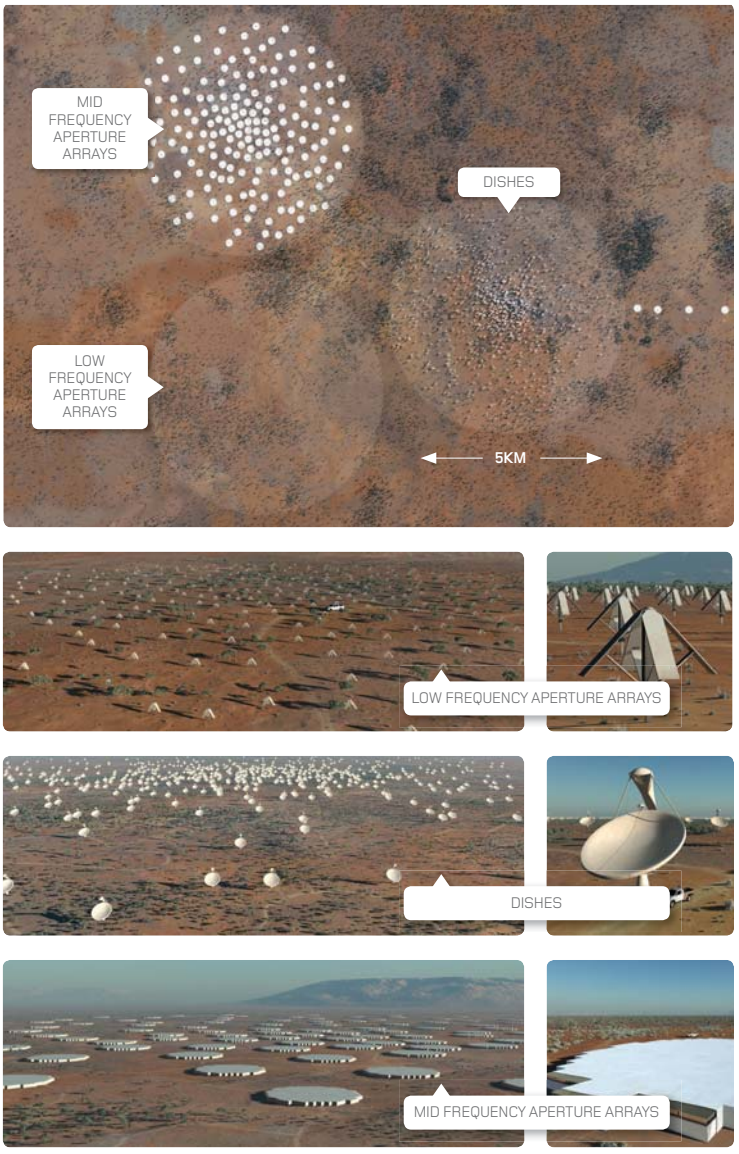

(b)

Figure 1.1: The proposed (a) layout of the SKA telescope illustrating (b) the three different antennas within the core, from [1].

The proposed layout of the SKA is shown in figure 1.1(a). It comprises of a central core, approximately 15 to 20 kilometres in diameter, containing the sparse and dense aperture arrays as well as almost half of the parabolic reflector antennas, as illustrated in figure 1.1(b). The remainder of the parabolic reflectors are situated in sub-stations spiralling outward to a distance of at least 3000 kilometres from the core site. This will allow for extremely long baselines and therefore excellent resolution. Two sites, Southern Africa and Australia, have been short-listed to host the SKA and both countries are currently working on SKA pathfinders. South Africa is building MeerKAT [6], a telescope that will consist of 64, 13.5 meter diameter Gregorian Offset reflector antennas and Australia is constructing the Australian Square Kilometer Array Pathfinder (ASKAP) [7] that will consist of 36, single reflector antennas, each with a diameter of 12 meters.

1.1.2 SKA Pathfinders

Apart from the two precursor telescopes being built on the candidate sites - MeerKAT and ASKAP - institutions around the globe are building other SKA pathfinders concentrating primarily on the sparse and dense aperture arrays. These include, amongst others [8]

- Murchison Widefield Array (MWA) - A phased array built in Australia, consisting of 16 dual-polarization dipoles operating over 80 - 300 MHz.
- Electronic Multi Beam Radio Astronomy ConcEpt (EMBRACE) - An aperture array concept being built in the Netherlands that will consist of an array of just over 20000 differentially fed antenna elements (possibly Vivaldi antennas) that conduct observations from 100 MHz up to 2 GHz.
- Long Wavelength Array (LWA) - Developed in the state of New Mexico, the LWA will consist of 53 phased array stations, each with 256 pairs of dipole type antennas, and operate over the frequency range of 10 - 80 MHz.

Two vastly different types of feeds are being considered for the reflector antennas of the precursor telescopes. MeerKAT will implement Wide-Band Single Pixel Feeds (WBSPFs) consisting of two dual-polarization dipoles and will support three receivers operating at 0.58 - 1.1015 GHz, 1 - 1.75 GHz, and 8 - 14.5 GHz. On the other hand ASKAP is investigating the implementation of Phased Array Feeds (PAFs) that consist of an array of more than 200 antenna elements, presently operating at a frequency range of 0.7 - 1.8 GHz with plans to extend the operating range to 0.5 - 10 GHz or even higher.

1.1.3 Differential Low Noise Amplifiers

Irrespective of the type of antenna implemented within each of the pathfinder telescopes for the SKA, the subsequent components within the Receiver Front End (RFE) presently all consist of single ended devices, even though all the antenna feeds are differential in nature. Until recently, baluns were implemented to connect the balanced antenna output to the single ended LNAs of the RFE but with the recent development of the SKA pathfinders such as MWA, EMBRACE, as well as ASKAP - each consisting of a large amount of differentially excited antenna elements - the possibility of using Differential Low Noise Amplifiers (dLNAs) has been drawing increasing interest from designers [9], [10], [7]. The loss introduced by any passive component placed between the antenna and the LNA contribute directly to the noise of the receiver system. Therefore, implementing dLNAs to feed the balanced antennas directly does away with the unnecessary noise added when connecting a balun to a single ended LNA. Furthermore, differential amplifiers display the inherent property of suppressing common-mode signals, reducing the receiver susceptibility to interference since interference - such as noise produced by biasing sources - generally couple in the common-mode. There are a number of disadvantages to implementing dLNAs in electronic circuits operating at microwave frequencies, some of which include an increase in LNA size as well as power consumption, but perhaps the most significant disadvantage is the increase in the complexity of the LNA design and characterisation.

1.2 Objectives

This thesis has as aim the study of the state-of-the-art techniques for the analysis of LNAs as well as the design and evaluation of an ultra low-noise dLNA in the L-band. The LNAs are aimed at the mid frequency band of the MeerKAT system, which at the time of design was at 1-1.75 GHz. This thesis includes the following aspects:

- A detailed study of classical noise theory, including the description of the predominant noise sources in electronic circuits and how these sources can be applied to existing small-signal models of active devices.
- Introduction of the noise correlation matrix. A powerful tool that can be used in conjunction with existing two-port and multi-port network theory to include noise during analysis.
- A study of the state-of-the-art techniques used to analyse differential LNAs, and the design thereof. This entails the definition of the differential and common-mode response as well as the differential noise performance of multi-port devices. Seeing that there is no definitive definition for the noise factor of multi-port differential devices - since the IRE/IEEE definition for noise factor only applies to two-port devices [5] - the noise characterisation of differential LNAs is not a trivial task.
- Presentation of techniques for very accurate measurement of dLNAs. Again, the introduction of differential aspects elevates the complexity of measurements substantially.

- The design of Differential Low Noise Amplifiers (dLNAs) using a balanced amplifier topology feeding a 180°-hybrid coupler. This topology allows for a direct connection between the LNA and the antenna feed, effectively reducing the unnecessary coupler losses by the gain of the amplifier. Due to the narrow bandwidth of planar hybrid couplers, techniques are investigated by which the operating bandwidth of these couplers can be increased.
- A dLNA with a noise figure below 0.6 dB was demonstrated successfully.

It will be seen that dLNAs introduce a number of advanced concepts not used in classical design, but critical in the understanding and design of dLNAs. This thesis aims to equip the reader with techniques by which the differential signal and noise performance of dLNAs can be calculated mathematically, predicted by means of simulations and finally validated using commercially available single ended measurements.

1.3 Overview

A brief history of the discovery and definition of the predominant sources of noise in electronic circuits is discussed in chapter 2. The concept of correlation between different noise generators is introduced in chapter 3 and the noise correlation matrix is defined, forming the basis for the derivation of the noise performance of multi-port networks. The differential and common-mode, referred to as mixed-mode, propagation of signals in multi-port differential networks are discussed in chapter 4 and the mixed-mode scattering matrix of a four-port differential device is derived. Noise figure measurement techniques of two-port as well as differential networks are discussed in chapter 5 and a method is derived by which the differential noise figure of a three-port dLNA can be de-embedded from two single ended noise figure measurements. This de-embedding method is verified with a differential LNA design, discussed in chapter 6. The work is concluded in chapter 7.

Chapter 2

Noise Circuit Analysis

As discovered by Robert Brown in 1827, molecular and sub molecular particles exist in a state of random motion. These random fluctuations, known as Brownian Movement, are observed in all applications be it mechanical, electrical or thermal in nature. In electrical systems, the effect similar to Brownian Movement is known as noise, and sets the limit for the magnitude of the smallest possible signal that can be observed, since any signal lower than this limit will be masked by the intrinsic noise [11]. It was only at the turn of the 20th century that engineers and physicists started characterising the intrinsic noise found in electrical systems. Through the work of Max Planck, based on the average energy of a system at thermal equilibrium, a theoretical expression for black body radiation was derived and the energy of radiated and absorbed electromagnetic quanta (photons) was quantified as hf, with h being Planck's constant [12]. With the implementation of active devices in electronic circuits (eg. amplifiers) additional sources of noise were introduced into electronic circuits. By the end of World War I the implementation of thermionic amplifiers had increased significantly especially in commercial and military phone systems. With numerous mechanical defects occurring during the production of the thermionic valves used in the amplifiers, Walter Schottky started to investigate the fluctuations in current due to faulty structures as well as methods to reduce or eliminate the noise generated due to these defects. What he found though was that there were two noise generators intrinsic to the nature of the thermionic valves that could not be attributed to manufacturing defects. In his paper published in 1918 he defines these two noise generators as *Shot Noise* and *Thermal Noise* [13].

The nature of these two noise sources are discussed in this chapter and various adaptations of transistor small signal models that include noise generators are introduced. These equivalent noise models can be represented as a noiseless two-port network with two equivalent noise sources applied to the input, providing a basis from which the two-port noise parameters can be determined. With these noise parameters known the noise performance of the transistor in any input termination can be predicted.

2.1 Noise Generators

In the analysis to follow all noise signals are considered as stochastic, band limited, signals around a stationary frequency, f_0, with random amplitude and phase, ie.

$$i(t) = A(t)e^{j(2\pi f_0 t + \phi(t))} \tag{2.1.1}$$

Since the noise signal defined in equation 2.1.1 is a stochastic signal its average value is zero and therefore the auto-correlation of the noise signal, with a zero time shift ($\tau = 0$) is considered where,

$$S_{ii^*} = \lim_{T\to\infty} \frac{1}{2T} \int_{-T}^{T} i(t+\tau)i^*(t)dt = < ii^* > \tag{2.1.2}$$

Equation 2.1.2 is also referred to as the spectral power density of the signal, defined as the total average power per ohm when integrated over the frequency domain and can be related to the total power dissipated per unit resistance, by

$$\overline{i^2} = 2\Delta f < ii^* > \tag{2.1.3}$$

where the factor of 2 is included due to the fact that noise signals are unilateral - only the positive part of the frequency spectrum is considered - and

$$\overline{i^2} = \frac{1}{T} \int_0^T i^2(t)dt \tag{2.1.4}$$

2.1.1 Shot Noise

Schottky ascribed the random fluctuations observed in the plate current in vacuum tubes to the discrete elementary nature of the Direct Current (DC) biasing current. He defined the fluctuations caused by the random arrival of each charge carrying electron as shot noise. In defining shot noise, Schottky made two significant simplifying assumptions. First he assumed that the transit time of each electron between the cathode and the plate is nearly instant, and that the pulse produced by each electron can be described by an impulse function. Shot noise therefore has an infinite flat frequency spectrum, known as *white noise*. Secondly he assumed that the only force acting on the electron in transit is the electrostatic force that exists between the cathode and the plate - an assumption that is only valid for a temperature limited plate current [14]. Taking these simplifications into account, Schottky expressed the shot noise generated at the plate as

$$\overline{i_{sn}^2} = 2qI_{DC}\Delta f \tag{2.1.5}$$

where q is the charge of an electron, I_{DC} is the DC biasing current flowing between the cathode and the anode, and Δf is the noise bandwidth. Although Schottky derived equation 2.1.5 for shot noise generated by the biasing current in vacuum tubes, exactly the same current impulses apply to the DC biasing current flowing through a pn-junction found in semiconductor devices.

2.1.2 Thermal Noise

According to Planck's law, the average radiated energy of a single black body propagation mode in thermal equilibrium is given by

$$W(f) = \frac{hf}{e^{\frac{hf}{kT}} - 1} \tag{2.1.6}$$

where k is Boltzmann's constant, T is the temperature in Kelvin, h is Plank's constant, and f denotes frequency [12]. For relatively low frequencies and high temperatures equation 2.1.6 can be simplified by applying the Rayleigh-Jeans approximation [15]. To illustrate this, consider the Taylor series expansion of

$$f(x = \frac{hf}{kT}) = e^x - 1 \tag{2.1.7}$$

$$f(x) = f(0) + f'(0)x + \frac{f''(0)}{2!}x^2 + \ldots \tag{2.1.8}$$

$$f(x) = e^x - 1 \approx x \tag{2.1.9}$$

Therefore, if $hf/kT \ll 1$ the average energy, within a bandwidth Δf, expressed by equation 2.1.6 can be approximated by

$$W(f) \approx kT \tag{2.1.10}$$

In his 1918 paper Schottky pointed out that intrinsic noise observed in thermionic amplifiers could be ascribed to two generators: *Shot noise* (Section 2.1.1) and *Thermal Noise*. He concluded that the effect of thermal noise would be masked by that of the shot noise and could therefore be neglected [13]. For nearly a decade engineers and physicist accepted Schottky's conclusion regarding thermal noise, until experiments performed by John B Johnson revealed that the thermal noise varied with the magnitude of the input resistance as well as temperature. Johnson published his findings in 1927 wherein he expressed the mean square electromotive force produced within a bandwidth Δf by thermal fluctuations within a piece of conductor with resistance R as

$$\overline{e_n^2} = 4kTR\Delta f \tag{2.1.11}$$

During this period Johnson discussed his findings with dr. H Nyquist and within the next year Nyquist pointed out that Johnson's experimental results conformed to Rayleigh-Jeans statistics and showed that for a matched load the average thermal noise power is equal to the average energy of a single black body propagation mode [11],

$$P = W(f)\Delta f = \frac{hf}{e^{\frac{hf}{kT}} - 1}\Delta f \tag{2.1.12}$$

From equation 2.1.12 it follows that, in terms of Planck's law, the mean square electromotive force of thermal noise generated by a conductor with resistance R within a bandwidth Δf is expressed as

$$\overline{e_n^2} = \frac{4Rhf}{e^{hf/kT} - 1}\Delta f \tag{2.1.13}$$

It is clear that equation 2.1.11 can easily be derived from equation 2.1.13 by applying the Rayleigh-Jeans approximation expressed in equation 2.1.9. It is therefore possible to represent any noisy resistor as either a noiseless Thévenin, or Norton, equivalent model as shown in figure 2.1, where the mean square thermal current generated by the conductance $G = 1/R$ is expressed as

$$\overline{i_n^2} = 4kTG\Delta f \tag{2.1.14}$$

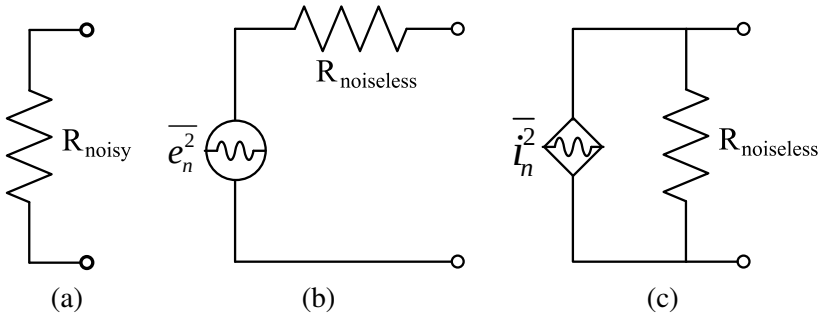

Figure 2.1: (a) Noisy Resistor, (b) Th*é*venin equivalent circuit, (c) Norton equivalent circuit.

2.1.3 Other Sources of Noise

Thermal and shot noise describe most of the noise generated within electronic devices at microwave frequencies. However there are many other sources of noise at other lower or higher frequencies and although these sources are not included in the models defined in the scope of this text, it is worth noting their existence. These sources include [16]:

- Flicker noise - observed in any circuit with DC signals, it displays a $\frac{1}{f}$ characteristic and is therefore neglected for amplifiers operating at microwave frequencies.
- Diffusion noise - Common in Field Effect Transistor (FET) models and describes the fluctuation in diffusion current due to the change in charge carrier velocities caused by collisions with impurities. This phenomenon is usually included in the definition of the channel thermal noise current calculated from the channel conductance [17].
- Generation-Recombination Noise - Impurities within a crystal lattice can trap charge carriers causing fluctuations in the amount of free carriers and therefore the conductivity of the material.
- Popcorn (Burst) Noise - Mostly associated with emitter junctions and observed as random bursts in collector current. It displays a $\frac{1}{f^2}$ characteristic and is therefore only important at very low frequencies.

2.2 Noise Circuit Models for Active Devices

In the years building up to World War II, William Shockley started researching the possibility of a semiconductor amplifier. As one of the notebook entries in [18] shows, Shockley had described amplification using a FET for the first time in 1940. His research was put on hold by the start of World War II, throughout which Shockley focused on semiconductor detectors for radar. During this time Germanium and Silicon semiconductors became the most widely used and improved methods of adding acceptor and donor impurities to semiconductors were developed, giving rise to the terms 'p- and n-type' semiconductors. Nearing the end of the war, Shockley returned to Bell Laboratories and continued his research in the semiconductor group along with John Bardeen and Walter Brattain and in December 1947 they demonstrated amplification using a junction transistor for the first time - starting a new era in electronics.
It soon became clear that there was one major drawback to the first junction transistors implemented in radio receivers: noise. First generation transistors were extremely noisy especially in the low kilohertz range where *Flicker Noise* was a strong component of the noise. With the improvement of transistor technology, this excessive noise was soon reduced to below a kilohertz, and it was realised that *Shot* and *Thermal* noise were the limiting factors in noise generated within transistors [16]. In the two sections that follow, the noise models of Bipolar Junction Transistors (BJTs) and FETs are introduced and methods of deriving an equivalent noiseless two-port for each device are discussed.

2.2.1 Bipolar Junction Transistors

With thermal noise already defined (Section 2.1.2) researchers turned their focus on the shot noise within p-n junctions and transistors and in 1955 A Van der Ziel published the first paper entitled: "'The theory of shot noise in junction diodes and transistors"' [19]. In this paper Van der Ziel illustrated the first equivalent circuit of a transistor, in common-base configuration, with its respective noise sources included. A year later Giacoletto published a noise equivalent model for the common-emitter configuration, containing three uncorrelated noise sources [20]. Giacoletto's model only showed the uncorrelated base and collector current shot noise generators with an additional noise source representing the noise caused by the diffusion of minority carriers through the base region. This was in contrast with the theory of Van der Ziel that included two partially correlated noise sources namely the collector and emitter shot noise generators. Nonetheless the theory of uncorrelated shot noise still conformed well to measurements. Fukui later transformed the common-base equivalent circuit of Van der Ziel into the common-emitter circuit of Giacoletto and expressed the conditions under which the base and collector shot noise generators can be considered uncorrelated [21]. In 1973 Motchenbacher developed a method to transform Giacoletto's noise equivalent circuit into a noiseless equivalent circuit of the transistor with two noise sources connected at the input, making it possible to determine the equivalent input noise produced by a transistor [17]. It is this method of Motchenbacher that is applied to the circuit of a BJT in this section.

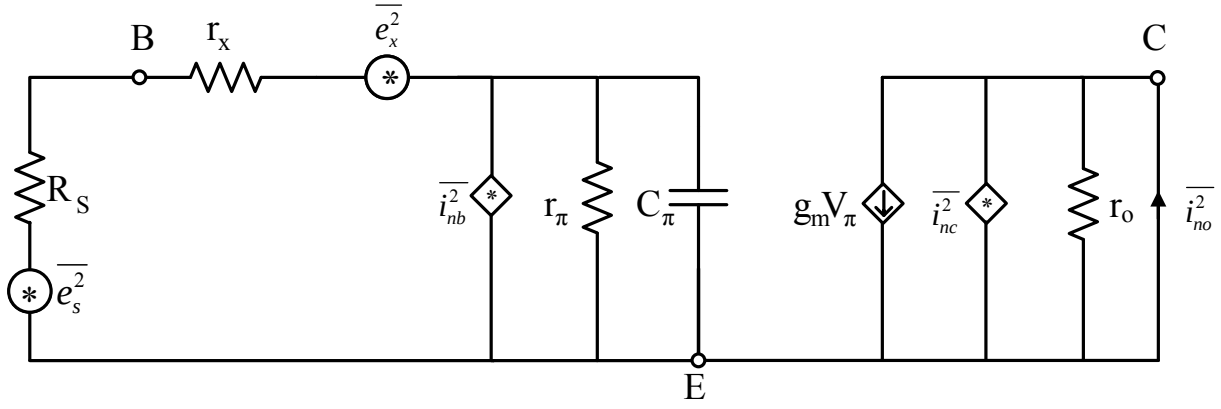

Figure 2.2: Giacoletto's noise equivalent model for a Bipolar Junction Transistor.

Figure 2.2 shows Giacoletto's general hybrid-π model for a BJT in the common-emitter configuration adopted by Motchenbacher. The model contains the well known elements that make up the small signal model of a BJT namely base-spreading resistance r_x, diffusion resistance r_π, forward-biased junction capacitance C_π, the voltage dependent current generator $g_m V_\pi$, and the dynamic output resistance r_o that is dependent on the Early voltage. Feedback elements C_μ and r_μ are not included in the model, limiting the validity of the model to frequencies under $\frac{f_T}{\sqrt{\beta_o}}$, with f_T the unity-gain frequency and β_o the low-frequency current gain of the transistor. Included in the model are the three major intrinsic noise sources of a BJT namely the thermal noise generator e_x generated by the physical base-spreading resistance r_x, and two shot noise generators i_{nb} and i_{nc} generated by fluctuations in the DC biasing current occurring at the base and collector junctions respectively. The complete model developed by Motchenbacher includes an additional flicker noise generator at the base of the transistor, since flicker noise is predominantly generated at the base-emitter junction [17]. However the designs considered within the scope of this text all operate at microwave frequencies, where the effect of flicker noise is negligible. The flicker noise source is therefore omitted from the model in figure 2.2.

As described in section 2.1 the mean square values of the three uncorrelated noise sources are given by

$$\overline{e_x^2} = 4kTr_x\Delta f \tag{2.2.1}$$

$$\overline{i_{nb}^2} = 2qI_B\Delta f \tag{2.2.2}$$

$$\overline{i_{nc}^2} = 2qI_C\Delta f \tag{2.2.3}$$

where I_B and I_C represent the DC currents flowing through the base and collector junctions. To gain a complete understanding of the noise performance of the transistor circuit the thermal noise, e_s, generated by the source resistance, R_s, connected to the base of the transistor is included in the model.

$$\overline{e_s^2} = 4kTR_s\Delta f \tag{2.2.4}$$

The method developed by Motchenbacher in [17] is now applied to the circuit in figure 2.2 to determine the equivalent input noise voltage, e_{ni}, of the four noise sources. In order to calculate the equivalent input noise voltage, the total short circuit output noise, i_{no}, as well as the transfer admittance, K, of the circuit has to be known. Since the transfer admittance relates the short circuit output current to a voltage signal at the input, as expressed in equation 2.2.5

$$K = \frac{I_o}{V_s} \tag{2.2.5}$$

the same factor can be used to determine the equivalent input noise voltage from the output noise current. Therefore

$$\overline{e_{ni}^2} = \frac{\overline{i_{no}^2}}{|K|^2}. \tag{2.2.6}$$

To determine the transfer admittance, the noise sources are first excluded from the model. By short-circuiting the collector, the output current is given by

$$I_o = g_m V_\pi \tag{2.2.7}$$

where the diffusion voltage V_π is expressed in terms of the input signal V_s as

$$V_\pi = \frac{Z_\pi}{R_s + r_x} V_s \tag{2.2.8}$$

with the impedance Z_π given by the parallel combination of r_π and C_π

$$Z_\pi = r_\pi // C_\pi \tag{2.2.9}$$

$$= \frac{r_\pi}{1 + \omega C_\pi r_\pi}. \tag{2.2.10}$$

By substituting equation 2.2.8 into equation 2.2.7 the transfer admittance given by equation 2.2.5 is solved as

$$K = \frac{g_m Z_\pi}{(Z_\pi + R_s + r_x)}. \tag{2.2.11}$$

Taking the noise sources into account, the short-circuited output noise current can be calculated from

$$\overline{i_{no}^2} = \overline{i_{nc}^2} + g_m^2 \overline{e_\pi^2} \tag{2.2.12}$$

where

$$\overline{e_\pi^2} = (\overline{e_x^2} + \overline{e_s^2}) \left[\frac{Z_\pi^2}{(R_s + r_x)^2} \right] + \overline{i_{nb}^2} \left[\frac{Z_\pi^2 (R_s + r_x)^2}{(Z_\pi + R_s + r_x)^2} \right] \tag{2.2.13}$$

as $\overline{i_{nc}^2}$, $\overline{e_x^2}$, and $\overline{e_\pi^2}$ are all uncorrelated. Substituting equation 2.2.13 into equation 2.2.12 yields the final expression for the output noise current due to all internal noise sources

$$\overline{i_{no}^2} = \overline{i_{nc}^2} + g_m^2 \left[\left(\overline{e_x^2} + \overline{e_s^2} \right) \left[\frac{Z_\pi^2}{(R_s + r_x)^2} \right] + \overline{i_{nb}^2} \left[\frac{Z_\pi^2 (R_s + r_x)^2}{(Z_\pi + R_s + r_x)^2} \right] \right] \tag{2.2.14}$$

Using equations 2.2.6, 2.2.11, and 2.2.14 the equivalent input noise can be expressed in terms of the transistors intrinsic noise sources

$$\overline{e_{ni}^2} = \overline{e_s^2} + \overline{e_x^2} + \overline{i_{nb}^2} (R_s + r_x)^2 + \overline{i_{nc}^2} \left[\frac{(Z_\pi + R_s + r_x)^2}{Z_\pi^2 g_m^2} \right]. \tag{2.2.15}$$

Consider the last term in equation 2.2.15. At low frequencies the impedance Z_π expressed in equation 2.2.10 reduces to

$$Z_\pi \approx r_\pi \tag{2.2.16}$$

and recalling that the low frequency current gain β_o can be expressed as

$$\beta_o = r_\pi g_m \tag{2.2.17}$$

the last term reduces to

$$\frac{\overline{i_{nc}^2} (r_x + R_s + r_\pi)^2}{\beta_o^2} \tag{2.2.18}$$

At microwave frequencies the last term in equation 2.2.15 can be simplified by assuming the operation frequency is high enough such that

$$Z_\pi \approx \frac{1}{j\omega C_\pi} \tag{2.2.19}$$

but still lower than $\frac{f_T}{\sqrt{\beta_o}}$ to ensure high gain. By applying the approximation given in equation 2.2.19 to equation 2.2.15 and recalling that the forward-biased junction capacitance C_π can be related to the unity gain frequency f_T

$$C_\pi = \frac{g_m}{2\pi f_T} \tag{2.2.20}$$

when it is assumed that the feedback capacitance C_μ is negligible, the last term in equation 2.2.15 reduces to

$$\overline{i_{nc}^2}(R_s + r_x)^2 \left(\frac{f}{f_T}\right)^2. \tag{2.2.21}$$

A close approximation for the equivalent input noise given by equation 2.2.15 for all frequencies up to $\frac{f_T}{\sqrt{\beta_o}}$ is therefore given by

$$\overline{e_{ni}^2} = \overline{e_s^2} + e_x^2 + \overline{i_{nb}^2}(R_s + r_x)^2 + \overline{i_{nc}^2}\frac{(r_x + R_s + r_\pi)^2}{\beta_o^2} + \overline{i_{nc}^2}(R_s + r_x)^2 \left(\frac{f}{f_T}\right)^2. \tag{2.2.22}$$

Equation 2.2.22 can now be used to find expressions for equivalent noise voltage and current sources, $\overline{e_n^2}$ and $\overline{i_n^2}$, for the circuit depicted in figure 2.3.

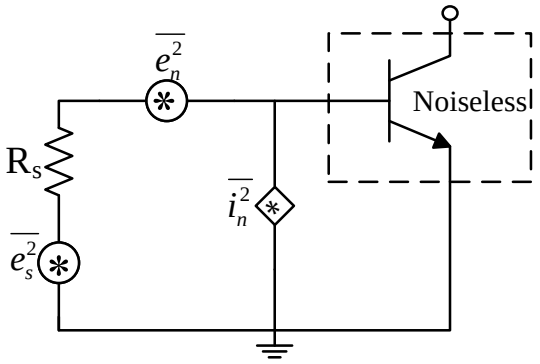

Figure 2.3: Equivalent noise sources connected to their associated noiseless BJT.

To express the noise voltage generated by the noise sources intrinsic to the BJT only, consider equation 2.2.22 with a source resistance R_s equal to zero, then

$$\overline{e_n^2} = \overline{e_x^2} + \overline{i_{nb}^2}r_x^2 + \overline{i_{nc}^2}\frac{(r_x + r_\pi)^2}{\beta_o^2} + \overline{i_{nc}^2}r_x^2 \left(\frac{f}{f_T}\right)^2. \tag{2.2.23}$$

Bearing in mind that $r_\pi = \beta_o r_e$, where r_e is the Shockley emitter resistance defined as the inverse of the transconductance g_m, equation 2.2.23 can be reduced to

$$\overline{e_n^2} = \overline{e_x^2} + \overline{i_{nc}^2}r_e^2 + \overline{i_{nc}^2}r_x^2 \left(\frac{f}{f_T}\right)^2 \tag{2.2.24}$$

since $r_x^2 \ll (\beta_o r_e)^2$.

In order to find an expression for the noise current source, $\overline{i_n^2}$ shown in figure 2.3, consider the case where the source resistance is infinite and that the equivalent input noise, $\overline{e_{ni}^2}$, is produced solely by the product $\overline{i_n^2}R_s^2$. This being the case, the input noise current can be solved by dividing each term in equation 2.2.22 by R_s and taking the limit for $R_s \to \infty$ such that

$$\overline{i_n^2} = \overline{i_{nb}^2} + \overline{i_{nc}^2}\left(\frac{f}{f_T}\right)^2. \tag{2.2.25}$$

With the values of $\overline{e_n^2}$ and $\overline{i_n^2}$ defined, the transistor circuit can be represented by its noiseless equivalent as depicted in figure 2.3. This representation, referred to as the chain representation when the transistor circuit is defined by its transmission parameters, forms the basis for deriving the noise parameters of the circuit, discussed in section 2.3.

2.2.2 Field Effect Transistors

The noise mechanisms of FETs are slightly more involved than those of BJTs. At first glance one would assume that it would be sufficient to associate shot noise with the biasing *drain* current as is done with the *base* and *collector* current for BJTs. However, as pointed out by Van der Ziel in [22], the noise generated within the conduction channel of an FET can only be considered as thermal in nature. This first noise model for FETs therefore only included a single thermal noise current source, dependent on the channel conductance of the FET. Van der Ziel later revised this noise model when a sharp increase in gate noise was observed at higher frequencies [23]. The increase in gate noise was attributed to the thermal noise generated in the conducting channel which coupled capacitively between the conducting channel and the gate. This lead to the noise model shown in figure 2.4, containing two partially correlated current noise sources, a gate and drain current source, connected to the input and the output respectively.

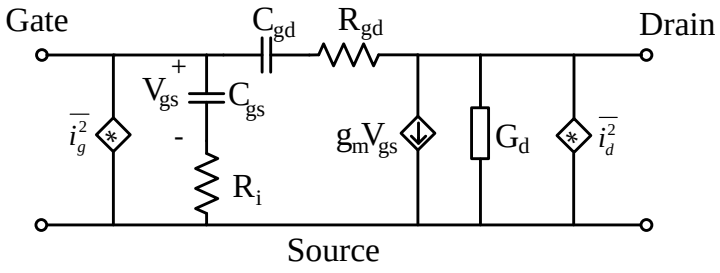

Figure 2.4: Noise model for FETs proposed by Van der Ziel.

The equivalent noise circuit developed by Van der Ziel proved to be adequate for early JFET and MOSFET devices, and has widely been used as a basis for developing improved noise models for modern devices [24], [25]. Modern FETs can be divided into three categories: Metal Oxide Semiconductor Field Effect Transistors (MOSFETs), Metal Semiconductor Field Effect Transistors (MESFETs), and High Electron Mobility Transistors (HEMTs), the latter are often used in circuits operating at microwave frequencies due to their low noise contribution. Although there are only small differences in the small signal models of the three types of FETs, two distinct approaches have been developed in describing the noise mechanisms of these FETs - Physical models and Empirical models. The physical models are mostly based on the analytical solution of the transport equations of charge carriers within the semiconductor lattice. While these models provide insight into the physical origin of the various noise mechanisms found in FETs, they tend to require a number of theoretical parameters that are not always readily available. Therefore nearly all physical noise models developed for FETs incorporate proportionality constants in the definitions of the noise generators in order to fit the models more accurately. Conversely, the empirical approach sets out to find what additional elements should be added to the device small signal model to correctly model the noise contribution. Noise generators are placed in correspondence to the available knowledge of the device's noise mechanisms and using measured data, fitting factors are extracted and applied to equations describing the generated noise. One such empirical model is the model developed by Fukui [26] wherein a number of fitting factors are extracted from measurements in order to accurately predict device noise performance. However, as described in [27], these fitting factors have no physical meaning and may lead to nonphysical two-ports. In 1989 M.W. Pospieszalski published a two parameter noise model for FETs [27] that is still widely used to model the noise of HEMTs in microwave circuits. It is this model proposed by Pospieszalski that is discussed in this section. The noise model proposed by Pospieszalski is shown in figure 2.5.

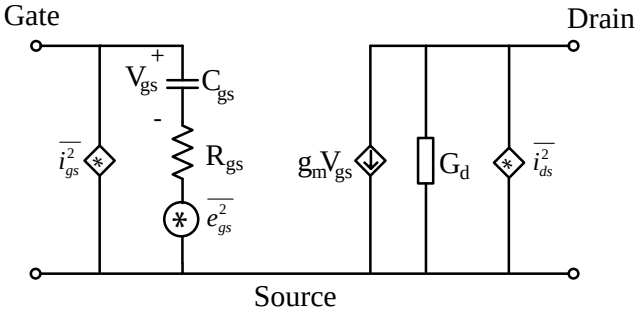

Figure 2.5: Noise model for FETs proposed by Pospiezalski.

The circuit shows a similar small signal model to the one used by Van der Ziel in figure 2.4, containing the following small signal parameters: Gate-source resistance r_{gs}, Gate-Source capacitance C_{gs}, Drain-Source conductance g_{ds} and neglects the Drain-Gate feedback resistance and capacitance. Included in Pospieszalski's noise model are three noise sources: Thermal gate noise voltage source $\overline{e_{gs}^2}$, Thermal drain noise current source $\overline{i_{ds}^2}$ and Gate leakage noise current source $\overline{i_{gs}^2}$ - although the gate leakage current source can be neglected for the majority of HEMT noise models [28] and will therefore be omitted in the noise analysis to follow.

The gate thermal noise voltage and drain thermal noise current, shown in figure 2.5, are defined by

$$\overline{e_{gs}}^2 = 4kT_g r_{gs}\Delta f \tag{2.2.26}$$

$$\overline{i_{ds}}^2 = 4kT_d g_{ds}\Delta f \tag{2.2.27}$$

where k is Boltzmann's constant, and temperatures T_g and T_d are the equivalent gate and drain temperatures, respectively. In most cases the equivalent gate temperature T_g can be made equal to the device ambient temperature without introducing much error, thus enabling full noise characterisation by extracting only the equivalent drain temperature from a single noise figure measurement. This process is discussed in section 2.4.2.
With the equivalent gate and drain temperatures as well as the small signal parameters known, the HEMT can be represented as a noiseless admittance network with two external noise current sources applied to the input and the output of the network as shown in figure 2.6.

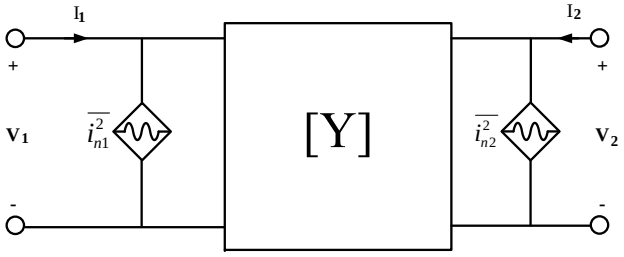

Figure 2.6: Admittance representation of a noisy HEMT.

The spectral current density of the two noise sources $\overline{i_{n1}^2}$ and $\overline{i_{n2}^2}$ in the equivalent noise model of figure 2.6 can be expressed in terms of equivalent noise conductances G_1 and G_2

$$\overline{i_{n1}}^2 = 4kT_0 G_1 \tag{2.2.28}$$

$$\overline{i_{n2}}^2 = 4kT_0 G_2 \tag{2.2.29}$$

and the correlation coefficient, describing the correlation between the two sources, by

$$\rho_c = \frac{i_{n1} i_{n2}^*}{\sqrt{\overline{i_{n1}^2}\,\overline{i_{n2}^2}}}. \tag{2.2.30}$$

By comparing the equivalent small signal noise model of figure 2.5 to the equivalent noiseless representation of figure 2.6, expressions for the equivalent noise conductances and correlation between them can be obtained in terms of the small signal parameters of the HEMT. That is,

$$G_1 = \frac{T_g}{T_0}\frac{r_{gs}(\omega C_{gs})^2}{1+\omega^2 C_{gs}^2 r_{gs}^2} \tag{2.2.31}$$

$$G_2 = \frac{T_g}{T_0}\frac{g_m^2 r_{gs}}{1+\omega^2 C_{gs}^2 r_{gs}^2} + \frac{T_d}{T_0} g_{ds} \tag{2.2.32}$$

and, by assuming the equivalent drain temperature $T_d = 0$, the drain noise will be perfectly correlated with the gate noise giving a correlation coefficient $\rho_c = -j1$.

Therefore the correlation is defined by

$$i_{n1}i_{n2}^{*} = \rho_c\sqrt{\overline{i_{n1}^2 i_{n2}^2}} = -j\frac{\omega g_m C_{gs} r_{gs}}{1+\omega^2 C_{gs}^2 r_{gs}^2}\frac{T_g}{T_0} \tag{2.2.33}$$

with the correlation coefficient being purely imaginary due to the capacitive coupling that exists between the channel and the gate [29]. Having solved the noise currents $\overline{i_{n1}^2}$ and $\overline{i_{n2}^2}$ as well as the correlation between them $i_{n1}i_{n2}^{*}$ in terms of the small signal parameters of the HEMT, the method described in [30] is used to transform the equivalent admittance model of figure 2.6 into the chain representation of a noiseless two-port shown in figure 2.7.

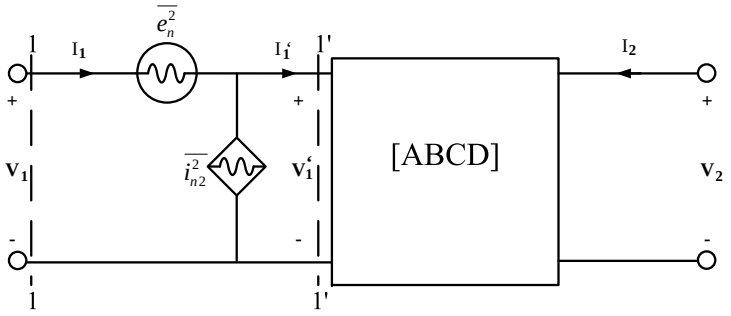

Figure 2.7: Chain representation of a noisy HEMT.

The external port currents of the equivalent admittance network are described by the following set of equations

$$I_1 = Y_{11}V_1 + Y_{12}V_2 + i_{n1} \tag{2.2.34}$$

$$I_2 = Y_{21}V_1 + Y_{22}V_2 + i_{n2} \tag{2.2.35}$$

Consider the currents and voltages at the input of the two-port network in figure 2.7. The voltage and current at plane $1-1$ can be expressed in terms of the voltage and current at plane $1'-1'$ as

$$V_1 = V_1^{'} + e_n \tag{2.2.36}$$

$$I_1 = I_1^{'} + i_n \tag{2.2.37}$$

Given that plane $1'-1'$ is at the input of the equivalent admittance network, equations 2.2.36 and 2.2.37 can be applied to equations 2.2.34 and 2.2.35, giving

$$I_1 = Y_{11}\left(V_1 - e_n\right) + Y_{12}V_2 + i_n \tag{2.2.38}$$

$$I_2 = Y_{21}V_1 + Y_{22}V_2 - Y_{21}e_n \tag{2.2.39}$$

The input referred noise voltage and current sources of the chain representation can therefore be solved in terms of the input and output noise currents of the admittance representation by comparing equations 2.2.38 and 2.2.39 with equations 2.2.34 and 2.2.35, giving

$$i_n = i_{n1} - \frac{Y_{11}}{Y_{21}}i_{n2} \tag{2.2.40}$$

$$e_n = -\frac{i_{n2}}{Y_{21}} \tag{2.2.41}$$

Representing the noisy HEMT by its equivalent noiseless chain representation, the equivalent noise sources can be used to determine the device's noise parameters, introduced in the next section.

2.3 Noise Parameters

In section 2.2 techniques are discussed whereby the noise generated within BJTs and FETs can be represented as equivalent noise sources applied to the input of the respective devices. In this section another set of parameters used to characterise the noise performance of linear two-ports are introduced. These parameters are referred to as noise parameters.

2.3.1 Equivalent two-port Noise Parameters

The first of the noise parameters is the equivalent noise resistance. It follows from the definition of thermal noise described in section 2.1.2 that the mean square fluctuations produced at the terminals of an open circuit resistor of value R at a temperature T is given by

$$\overline{e^2} = 4kTR\Delta f. \tag{2.3.1}$$

The equivalent noise resistance, R_n, of a network that produces a noise voltage $\overline{e^2}$ is therefore defined by

$$R_n = \frac{\overline{e^2}}{kT_0\Delta f} \tag{2.3.2}$$

where T_0 is the standard temperature, $290K$. It should be noted that the quantity R_n does not represent a physical resistance within the network but is merely used as a means to compare the noise generated by the internal noise sources of the network to the noise generated by the physical resistors of the network [31].
The second noise parameter is the noise factor (F) also referred to as noise figure (NF), where the noise figure is related to the noise factor by

$$NF = 10log(F) \tag{2.3.3}$$

As defined by Friis [32], this is a measure of degradation in the signal to noise ratio (S/N) that occurs when a signal passes through the two-port network

$$F = \frac{S_i/N_i}{S_o/N_o} \tag{2.3.4}$$

where i denotes the input port and o denotes the output port of the two-port network. According to IEEE standards, the expression for the noise factor of a linear two-port given in equation 2.3.4 is also defined as the ratio of the total output noise power per unit bandwidth to the portion of the output noise power produced by the source at standard temperature $T_0 = 290K$ [33], that is

$$F = \frac{Total\ output\ Noise\ per\ unit\ bandwidth}{Portion\ of\ output\ Noise\ produced\ by\ the\ source}. \tag{2.3.5}$$

For an arbitrary source impedance N_i is given by

$$N_i = kT\Delta f \tag{2.3.6}$$

as defined by Nyquist. Furthermore the gain of the linear two-port is expressed as the ratio of the output signal to the input signal, that is

$$G = \frac{S_o}{S_i}. \tag{2.3.7}$$

Substituting equations 2.3.7 and 2.3.6 into equation 2.3.4 the noise factor can be expressed as

$$F = \left(\frac{1}{G}\right)\left(\frac{N_o}{kT\Delta f}\right). \tag{2.3.8}$$

Seeing that the gain, expressed in equation 2.3.7, is independent of the output circuit connected to the two-port network, the output network has no effect on the noise figure of two-port network. However, since the available power from the signal source, S_i, is dependent on the degree of mismatch between the two-port network and the source, the output noise power, N_o, and therefore also the noise figure depend on the source impedance presented to the two-port network. Due to the fact that the noise figure varies with the degree of mismatch between the source and the two-port network, there exists an optimum source admittance $Y_{opt} = G_{opt} + jB_{opt}$ for which the noise factor of the linear two-port is a minimum, referred to as F_{min}. Knowing these four parameters: R_n, F_{min}, G_{opt}, and B_{opt} the noise figure of any linear two-port network in any input termination can be determined using

$$F = F_{min} + \frac{R_N}{G_S}|Y_S - Y_{opt}|^2 \tag{2.3.9}$$

where $Y_S = G_S + jB_S$ is the source admittance presented to the network.

2.3.2 Noise Parameters of a Bipolar Junction Transistor

2.3.2.1 Motchenbacher's Noise Model

By applying the theory introduced in section 2.2.1 a BJT amplifier can be represented by the equivalent amplifier noise model depicted in figure 2.8. The model shows the noiseless amplifier with its equivalent input referred

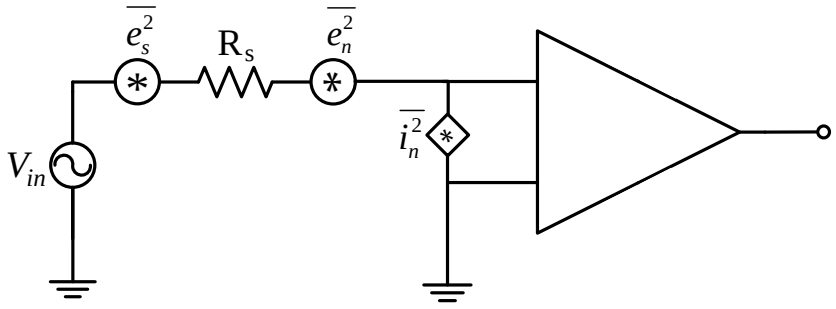

Figure 2.8: General noise equivalent model of an amplifier.

noise voltage and current sources, $\overline{e_n^2}$ and $\overline{i_n^2}$, the source resistance R_s and its thermal noise voltage $\overline{e_s^2}$ as well as the input signal source V_{in}. Motchenbacher assumes the three noise sources to be uncorrelated and, under this assumption, the equivalent input noise for the amplifier can be determined using the following equation,

$$\overline{e_{ni}^2} = \overline{e_s^2} + \overline{e_n^2} + \overline{i_n^2} R_s^2. \tag{2.3.10}$$

The noise model in figure 2.8 can therefore be represented by only the input signal, V_{in}, and a single noise voltage source, $\overline{e_{ni}^2}$. This provides an easy way to compare the noise performance of different amplifier topologies, since $\overline{e_{ni}^2}$ is independent of both the input impedance and the gain of the amplifier [17].
Therefore by applying the IEEE definition, given in equation 2.3.5, the noise factor can be solved in terms of the equivalent input noise given in equation 2.3.10

$$F = \frac{\overline{e_{ni}^2}}{\overline{e_s^2}} = \frac{\overline{e_s^2} + \overline{e_n^2} + \overline{i_n^2} R_s^2}{\overline{e_s^2}}. \tag{2.3.11}$$

Equation 2.3.11 indicates that the noise figure of an amplifier can be reduced by an increase in the thermal noise of the source resistance. This does not imply that a higher source resistance equals a lower noise figure, rather that there exits a source resistance for which the noise figure will be a minimum. This value is known as the optimum source resistance, described in section 2.3, and is given by the ratio of the amplifier noise sources,

$$R_{opt} = \sqrt{\frac{\overline{e_n^2}}{\overline{i_n^2}}}. \tag{2.3.12}$$

Since all the noise sources contained in the equivalent noise circuit of figure 2.8 are assumed to be uncorrelated, the optimum source impedance is real. Another noise model proposed by Voinigescu [34], that takes the correlation between the input noise sources into account, is introduced in the next section.

2.3.2.2 Voinigescu's Noise Model

Nielsen was the first to derive expressions for the noise parameters of BJTs in terms of general transistor parameters [35]. Using the noise equivalent circuit developed by Van der Ziel, he derived equations for the noise figure of transistors in the common-base, -collector, and -emitter configurations. Although he assumed that all the noise sources are uncorrelated, the theoretical predictions still conformed well to the measured noise figures. A year later Van der Ziel published a new set of equations for the noise parameters taking the correlation between the noise sources into account and explained why the expressions published by Nielsen still produced accurate results [36]. In the years to follow many authors published new expressions for the noise parameters in terms of general transistor parameters [21], [37], [17]. With the development of SPICE models and the correlation matrix (discussed in detail in chapter 3) Voinigescu developed a new set of equations in terms of the easily obtainable SPICE parameters of a BJT [34]. Applying the technique developed for FETs by Dambrine in [38], Voinigescu transformed the noise equivalent circuit of a BJT containing an emitter resistance (r_e) (figure 2.9) into a noiseless equivalent circuit similar to figure 2.3.

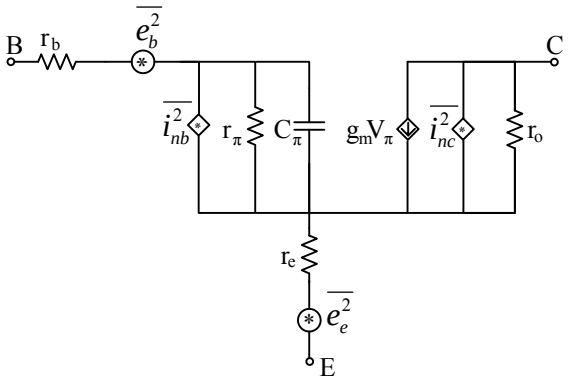

Figure 2.9: Small signal noise equivalent circuit used for derivation of noise parameters.

That is, assuming the base and collector shot noise sources ($\overline{i_{nb}^2}$ and $\overline{i_{nc}^2}$) are uncorrelated, the input referred noise sources as well as their cross-correlation are given by

$$\overline{e_n^2} = \frac{\overline{i_{nc}^2}}{|Y_{21}|^2} + 4kT_0\,(r_b + r_e)\,\Delta f \tag{2.3.13}$$

$$\overline{i_n^2} = \overline{i_{nb}^2} + \frac{|Y_{11}|^2\overline{i_{nc}^2}}{|Y_{21}|^2} \tag{2.3.14}$$

$$e_n i_n^* = e_n^* i_n = \frac{Y_{11}\overline{i_{nc}^2}}{|Y_{21}|^2} \tag{2.3.15}$$

Also the correlation admittance describing the correlation between the noise voltage and current sources is given by the expression

$$Y_c = \frac{e_n i_n^*}{\overline{e_n^2}} \tag{2.3.16}$$

However, with the assumption that the base and collector current sources are uncorrelated, it can be shown that $Y_c \approx Y_{11}$ [38], [34] and therefore

$$e_n i_n^* = Y_c\overline{e_n^2} \approx Y_{11}\overline{e_n^2} \tag{2.3.17}$$

Voinigescu uses the correlation matrix to derive expressions for the noise parameters as shown below. The noise parameters can be expressed in terms of the elements of the chain representation of the correlation matrix (refer to chapter 3 for the derivation)

$$R_n = \frac{C_{ee^*}}{2kT_0} \tag{2.3.18}$$

$$Y_{opt} = \sqrt{\frac{C_{ii^*}}{C_{ee^*}} - \left[\Im\left(\frac{C_{ei^*}}{C_{ee^*}}\right)\right]^2} + j\Im\left(\frac{C_{ei^*}}{C_{ee^*}}\right) \tag{2.3.19}$$

$$F_{min} = 1 + \frac{C_{ei^*} + C_{ee^*}Y_{opt}}{kT_0} \tag{2.3.20}$$

where the elements of the correlation matrix are defined as the auto- and cross-correlated spectral power densities of the intrinsic noise sources of the BJT. That is,

$$\frac{C_{e_n e_n^*}}{2kT_0\Delta f} = \frac{\overline{e_n^2}}{4kT_0\Delta f} = \frac{\overline{i_{nc}^2}}{4kT_0\Delta f|Y_{21}|^2} + (r_b + r_e) \tag{2.3.21}$$

$$\frac{C_{e_n i_n^*}}{2kT_0\Delta f} = \frac{e_n^* i_n}{4kT_0\Delta f} \approx \frac{Y_{11}\overline{i_{nc}^2}}{4kT_0\Delta f|Y_{21}|^2} \tag{2.3.22}$$

$$\frac{C_{i_n i_n^*}}{2kT_0\Delta f} = \frac{\overline{i_n^2}}{4kT_0\Delta f} = \frac{\overline{i_{nb}^2}}{4kT_0\Delta f} + \frac{|Y_{11}|^2\overline{i_{nc}^2}}{4kT_0\Delta f|Y_{21}|^2} \tag{2.3.23}$$

By neglecting feedback parameters r_μ and C_μ as well as the Early effect, it is found that $|Y_{21}|$ is approximately equal to the transconductance g_m. Since the collector current, expressed in terms of reverse saturation current I_s and base-emitter voltage v_{BE} can be approximated as in equation 2.3.25

$$i_C = I_S\left(e^{\frac{v_{BE}}{nV_T}} - 1\right) \tag{2.3.24}$$

$$\approx I_S\left(e^{\frac{v_{BE}}{nV_T}}\right) \tag{2.3.25}$$

where n is the collector current ideality factor, usually assumed 1, and V_T is the thermal voltage given by

$$V_T = \frac{kT_0}{q} \tag{2.3.26}$$

It therefore follows that

$$|Y_{21}| = g_m = \frac{\partial i_C}{\partial v_{BE}}|_{Q-point} \tag{2.3.27}$$

$$= \frac{I_C}{nV_T} \tag{2.3.28}$$

Substituting equations 2.3.21 to 2.3.23 into equations 2.3.18 to 2.3.20 the noise parameters of a BJT can be expressed in terms of the transistor parameters, using the relationships shown in equations 2.3.28 and 2.2.20. Hence,

$$R_n = \frac{n^2V_T}{2I_C} + r_E + r_B \tag{2.3.29}$$

$$Y_{opt} = \frac{f}{f_T R_n}\left(\sqrt{\frac{I_C}{2V_T}(r_E + r_B)\left(1 + \frac{f_T^2}{\beta_o f^2}\right) + \frac{n^2 f_T^2}{4\beta_o f^2}} - j\frac{n}{2}\right) \tag{2.3.30}$$

$$F_{min} = 1 + \frac{n}{\beta_o} + \frac{f}{f_T}\sqrt{\frac{2I_C}{V_T}(r_E + r_B)\left(1 + \frac{f_T^2}{\beta_o f^2}\right) + \frac{n^2 f_T^2}{\beta_o f^2}} \tag{2.3.31}$$

These expressions make it possible to characterise the noise performance of a BJT using only the small signal parameters of the device. Furthermore, the values of the equivalent noise voltage and current sources in figure 2.3, as well as the correlation between them, can be solved from these equations using the theory on the correlation matrix, described in chapter 3.

2.3.3 Noise Parameters of Field Effect Transistors

In section 2.2.2 an equivalent noise model for HEMTs is derived in the form of a noiseless two-port network - defined by the transmission parameters of the small signal model of an HEMT - with a correlated noise voltage source and noise current source connected to the input of the two-port. This equivalent noise representation, shown in figure 2.7, is used in this section to derive the noise parameters of an HEMT in terms of the device's small signal parameters. The spectral densities of the equivalent noise voltage and current sources are given by

$$\overline{e_n^2} = 4kT_0R_n \tag{2.3.32}$$

$$\overline{i_n^2} = 4kT_0g_n \tag{2.3.33}$$

where R_n and g_n are referred to as the equivalent noise resistance and noise conductance, respectively. Furthermore the correlation between the two sources are defined by the correlation admittance

$$Z_c = R_c + jX_c \tag{2.3.34}$$

Similar to the method applied by Voinigescu in section 2.3.2.2, the correlation admittance is defined by assuming no correlation between the equivalent gate and drain noise sources e_{gs} and i_{ds}. That is, in terms of the small signal parameters,

$$Z_c \approx Z_{11} = r_{sg} + \frac{1}{j\omega C_{sg}} \tag{2.3.35}$$

The equivalent noise resistance and conductance can be solved in terms of the small signal parameters of the HEMT by substituting the equivalent noise conductance values, derived in equations 2.2.31 and 2.2.32, into the expressions for the noise voltage and current sources shown in equations 2.2.40 and 2.2.41, giving

$$R_n = \frac{G_2}{|Y_{21}|^2} \tag{2.3.36}$$

$$g_n = G_1 - G_2\frac{|Y_{11}|^2}{|Y_{21}|^2} \tag{2.3.37}$$

or in terms of the small signal parameters

$$R_n = \frac{T_g}{T_0}r_{gs} + \frac{T_d}{T_0}\frac{g_{ds}}{g_m^2}\left(1+\omega^2C_{gs}^2r_{gs}^2\right) \tag{2.3.38}$$

$$g_n = \left(\frac{f}{f_T}\right)^2\frac{g_{ds}T_d}{T_0} \tag{2.3.39}$$

given that

$$f_T = \frac{g_m}{2\pi C_{gs}} \tag{2.3.40}$$

By performing an analysis analogous to that of section 3.2 Pucel *et al.* derived expression for the noise parameters in terms of the noise resistance, conductance and correlation impedance [24], with the real and imaginary parts of the optimum source impedance being equal to

$$R_{opt} = \sqrt{R_c^2 + \frac{R_n}{g_n}} \tag{2.3.41}$$

$$X_{opt} = -X_c \tag{2.3.42}$$

and the minimum noise figure expressed as

$$F_{min} = 1 + 2g_n \left(R_c + R_{opt}\right) \tag{2.3.43}$$

Substituting equations 2.3.35, 2.3.38 and 2.3.39 into equations 2.3.41 to 2.3.43, the noise parameters are solved in terms of the HEMT small signal parameters and equivalent gate and drain temperatures

$$R_{opt} = \sqrt{\left(\frac{f_T}{f}\right)^2 \frac{r_{gs}}{gds}\frac{T_g}{T_d} + r_{gs}^2} \tag{2.3.44}$$

$$X_{opt} = \frac{1}{\omega C_{gs}} \tag{2.3.45}$$

$$T_{min} = 2\frac{f}{f_T}\sqrt{g_{ds}r_{gs}T_gT_d + \left(\frac{f}{f_T}\right)^2 r_{gs}^2 g_{ds}^2 T_d^2} + 2\left(\frac{f}{f_T}\right)^2 r_{gs}g_{ds}T_d \tag{2.3.46}$$

where the minimum noise temperature (T_{min}) is related to the minimum noise factor by

$$T_{min} = \left(F_{min} - 1\right) T_0 \tag{2.3.47}$$

Furthermore, under the condition that

$$\frac{f}{f_T} \ll \sqrt{\frac{T_g}{T_d}\frac{1}{r_{gs}g_{ds}}} \tag{2.3.48}$$

then

$$R_{opt} \gg r_{gs} \tag{2.3.49}$$

and equations 2.3.44 and 2.3.46 reduce to

$$R_{opt} = \frac{f_T}{f}\sqrt{\frac{r_{gs}}{gds}\frac{T_g}{T_d}} \tag{2.3.50}$$

$$T_{min} = 2\frac{f}{f_T}\sqrt{g_{ds}r_{gs}T_gT_d} \tag{2.3.51}$$

2.4 Experimental Verification of Noise Models

To illustrate the validity of the noise models described in the previous sections, both of the BJT noise models are applied to an elementary, L-band, LNA design implementing a single BFG425W NPN transistor manufactured by Phillips Semiconductors. The FET noise model is verified by applying the noise model of Pospieszalski introduced in section 2.4.2 to a HEMT manufactured by AVAGO.

2.4.1 Bipolar Junction Transistor Amplifier Design

The BFG425W data sheet (refer to appendix A.1) includes two sets of noise parameters for varying collector current. However, since none of the noise data gives an indication of the noise performance of the transistor within the L-band, the two BJT noise models are used to determine the noise performance of the BJT within the band of interest.

One of the first steps in designing an LNA is to determine the magnitude of the biasing current that will ensure low noise contribution from the transistor. This is accomplished by implementing the technique described by Motchenbacher in section 2.2.1. Using equation 2.3.10, the equivalent input noise of the transistor can be expressed as a function of collector current at a specific frequency. Since this design is purely for investigative purposes, it is simplified by assuming a source resistance of 50Ω, instead of designing for an optimum source impedance, and the equivalent input noise is calculated at a frequency of 1.42 GHz (a critical frequency in radio astronomy - the spectral line for Hydrogen gas). This expression is then used to find the collector current that will result in a minimum equivalent input noise. The graph in figure 2.10 shows the transistor's equivalent input noise at $f = 1.42$ GHz as a function of collector current.

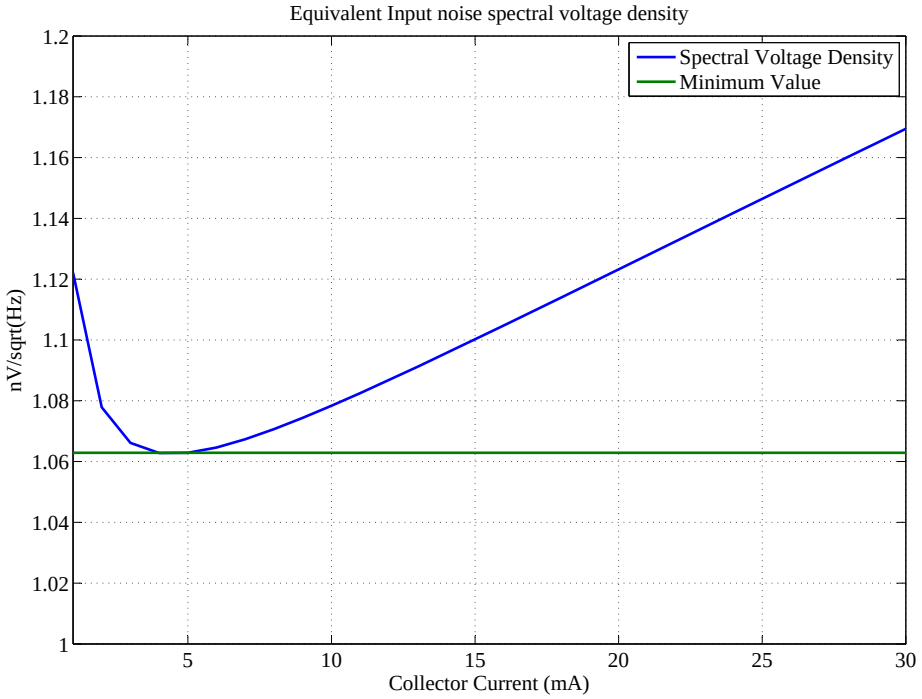

Figure 2.10: Equivalent input noise as a function of collector current.

It is clear from figure 2.10 that there is an ideal value for the collector current for which the equivalent input noise contributed by the transistor is a minimum. The biasing circuit of the LNA is therefore designed such that the collector current equals this optimum value.

2.4.1.1 Motchenbacher's noise model

With the optimum collector current for low noise contribution known, the transistor can be represented as a noiseless transistor with two equivalent noise sources applied to the input as depicted in figure 2.3. The values of the equivalent noise voltage and current sources (e_n and i_n) are solved, for the desired collector current, using equations 2.2.24 and 2.2.25 respectively. To investigate the accuracy of this model the LNA circuit is simulated in RF/Microwave simulation software, Microwave Office (MWO), developed by AWR. Consider the circuit schematic of the LNA shown in figure 2.11.

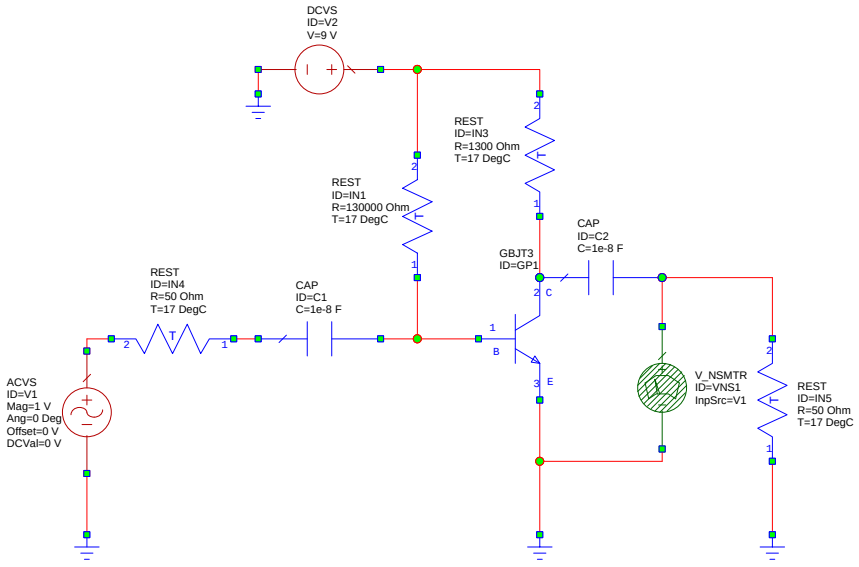

Figure 2.11: SPICE simulation of LNA circuit biased for minimum noise contribution.

The SPICE parameters of the BFG425W transistor is entered into the transistor model provided by MWO and the noise voltage at the output of the LNA is simulated using the linear simulator in MWO. By disabling the internal noise model of the transistor element, the LNA circuit can be simulated using the noiseless equivalent circuit of Motchenbacher. The LNA circuit containing a noiseless transistor with the two equivalent noise sources applied to the input is shown in figure 2.12. Figure 2.13 shows a graph comparing the simulated output noise voltage of the two circuits depicted in figures 2.11 and 2.12. It is clear that the simulation results from the noise model proposed by Motchenbacher deviates slightly from the internal noise model of MWO, which is to be expected since the equivalent input noise sources are assumed to be uncorrelated.

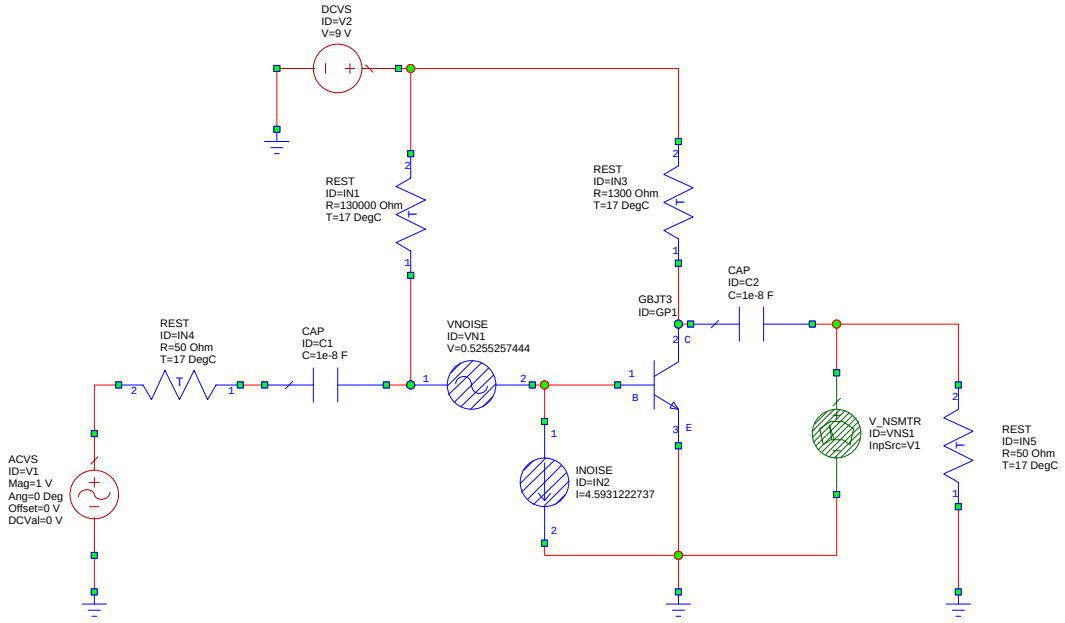

Figure 2.12: LNA circuit implementing Motchenbacher's noise model.

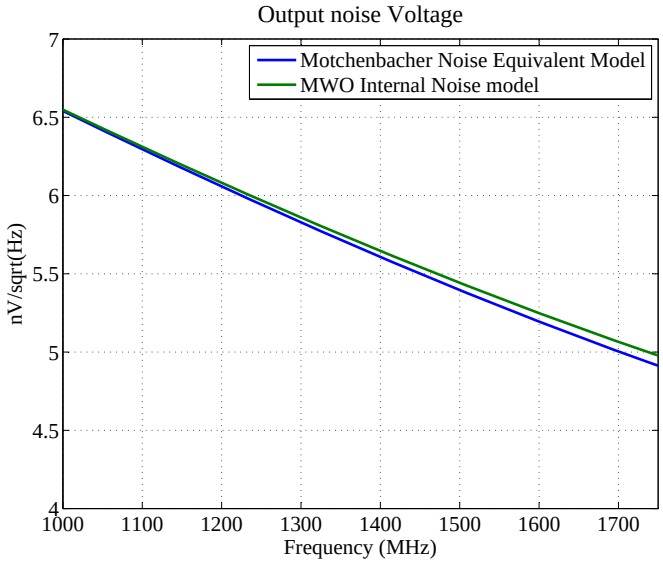

Figure 2.13: Simulated output noise of Motchenbacher's noise model.

2.4.1.2 Voinigescu's noise model

Microwave circuits are often characterised in terms of their Scattering (S)- and noise parameters. These parameters can be imported into MWO in the form of a TOUCHSTONE data file, thereby enabling designers to use measured data within the desired bandwidth to analyse their designs. The S-parameter data for the BFG425W transistor is provided by the manufacturer at various frequencies and for a number of biasing points.

Since the noise data for the transistor is limited, the equations developed by Voinigescu, equations 2.3.29 to 2.3.31, are applied to the transistor model to calculate the noise parameters of the device within the desired bandwidth. The LNA design shown in figure 2.11 consisting of a transistor element containing the device specific SPICE parameters with the internal noise sources activated is now represented by a circuit containing the S-parameters and calculated noise parameters of the transistor as shown in figure 2.14. (Refer to appendix A.2 for the TOUCHSTONE file). The validity of Vionigescu's model is investigated by comparing the simulated

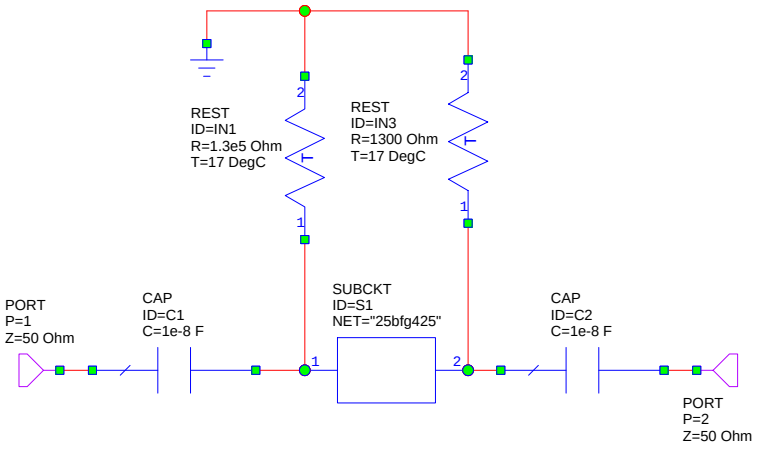

Figure 2.14: LNA circuit diagram containing transistor S-parameters and calculated noise parameters.

noise figure of the LNA shown in figure 2.14 to that of the LNA circuit implementing the internal noise model of MWO as well as the noise model developed by Motchenbacher shown in figures 2.11 and 2.12 respectively. This comparison is shown in the graph in figure 2.15.

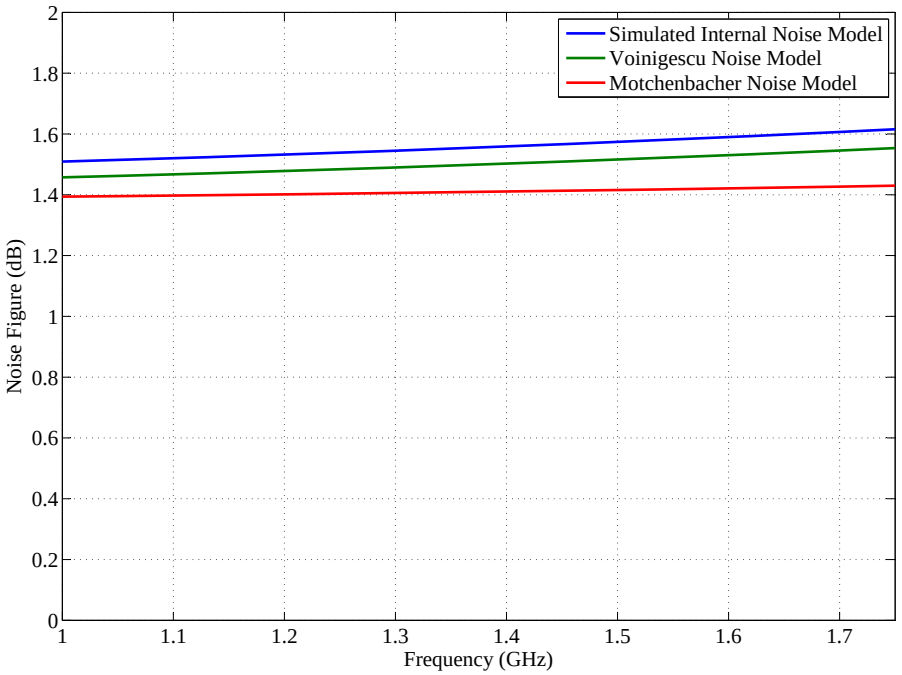

Figure 2.15: Simulated noise figure of the BJT noise models.

The graph in figure 2.15 shows that both the models of Voinigescu and Motchenbacher prove to be adequate for predicting the noise performance of a BJT. By considering the deviation of noise figure calculated from Motchenbacher's model, the importance of including the correlation between the input noise sources is emphasized.

2.4.2 Field Effect Transistors - Pospieszalski's Noise Model

This section uses the noise model of Pospieszalski described in section 2.2.2 to determine the minimum noise figure of a GaAs HEMT manufactured by AVAGO - VMMK1218. (Refer to appendix B for the device noise and small signal parameters). The aim of this investigation is to determine the equivalent gate and drain noise temperatures (T_g and T_d) from the measured noise parameters provided, and then to use these values to predict the noise performance of the HEMT based on the expressions derived by Pospieszalski. Consider the noise parameters, for $V_{DS} = 3$V and $I_{DS} = 20$mA, measured at a frequency of 10GHz. Since the optimum source resistance (R_{opt}) is significantly larger than the value of the gate source resistance (r_{gs}), the reduced equations for the source resistance and minimum noise temperature (equations 2.3.50 and 2.3.51) are used to determine the values of drain and gate noise constants, defined by

$$K_d = T_d g_{ds} \tag{2.4.1}$$

$$K_g = T_g r_{gs} \tag{2.4.2}$$

respectively. Thus, by solving K_d and K_g from

$$R_{opt} = \frac{f}{f_T}\sqrt{\frac{K_g}{K_d}} \tag{2.4.3}$$

$$T_{min} = 2\frac{f}{f_T}\sqrt{K_d K_g} \tag{2.4.4}$$

where f_T is given by equation 2.3.40, the equivalent drain and gate noise temperatures are calculated using equations 2.4.1 and 2.4.2, respectively. Since the noise generated by the HEMT is considered to be frequency independent, these values of the equivalent noise temperatures, together with the small signal parameters of the HEMT, are used in equation 2.3.46 to calculate the equivalent noise temperature within a desired bandwidth. Figure 2.16 shows a graph comparing the measured minimum noise figure provided by the manufacturer, over a bandwidth from 2-18 GHz, with the minimum noise figure calculated using the above mentioned method.

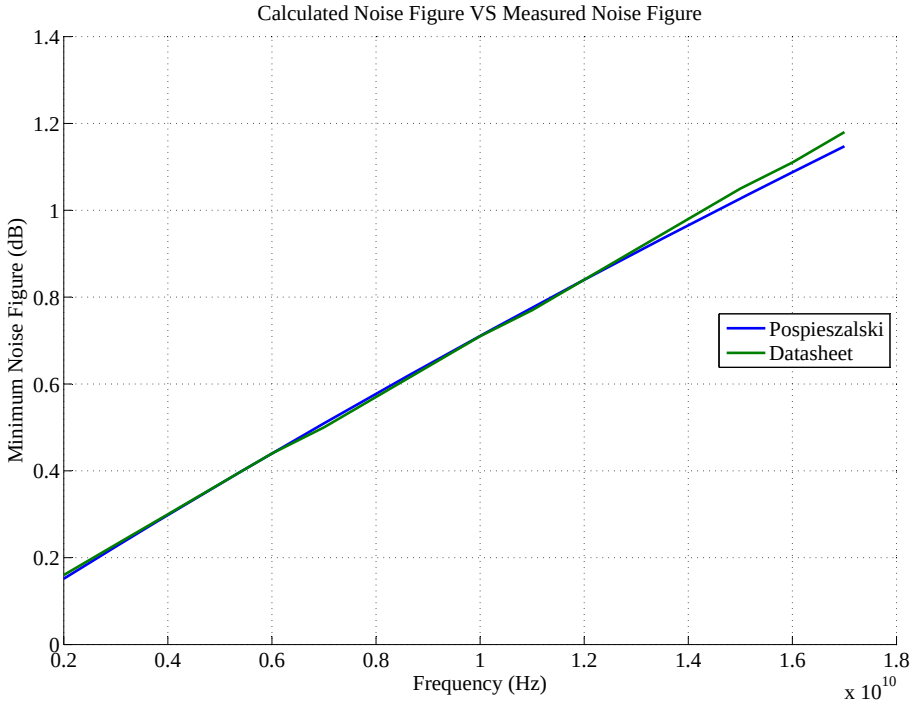

Figure 2.16: Experimental verification of HEMT noise model.

The graph in figure 2.16 clearly shows that the noise model of Pospieszalski conforms extremely well to measured data. However, it should be mentioned that the calculated equivalent gate noise temperature is in the order of a few thousand Kelvin and not close to ambient temperature as stated in section 2.2.2. This difference in equivalent gate noise temperature can be attributed to the fact that the accurate determination of the gate source resistance proves to be troublesome. It is therefore suggested that the noise constants of equations 2.4.1 and 2.4.2 be used in FET noise analysis, instead of solving the equivalent noise temperatures separately [27].

2.5 Conclusion

This chapter introduced the predominant sources of noise found in electronic circuits and applied this theory to the two major classes of active devices - BJTs and FETs. The equivalent noise models for these devices were discussed together with the methods of representing each one as a noiseless two-port network with a noise voltage and current source applied to the input. These models provided the basis for deriving expressions for the four noise parameters of each device. The graphs comparing the calculated noise parameters to that of data provided in the data sheet, show that these models give a valid prediction of what the noise performance of each device should be. It is also clear from the verification of these models, that the correlation between equivalent noise sources, as well as the transformation between various representations, form an integral part of noise analysis. Both of these topics are discussed in chapter 3.

Chapter 3

Noise Correlation Matrix

Chapter 2 introduced various noise generators to the familiar small signal models of Bipolar Junction Transistors (BJTs) and Field Effect Transistors (FETs) and illustrated techniques through which these small signal models can be represented as noiseless two-port networks with two noise generators connected to the two-port input. Noise generated at a specific device terminal is often influenced by noise originating from a different source. The influence noise from different physical origins have on one another is referred to as the correlation between the noise sources. This chapter introduces the noise correlation matrix: a powerful tool that bridges the gap between the measurable noise parameters and the analytical expressions for noise generators used in network analysis.

The noise correlation matrix greatly simplifies noise network analysis. This is illustrated in section 3.1 where three representations of the correlation matrix, each corresponding to a different electrical two-port representation, is introduced and the ease with which one representation can be transformed to another is demonstrated. In section 3.2 a direct relation between the elements of the noise correlation matrix and the noise parameters of a two-port network is derived, making it possible to use measured noise performance during network analysis. Conversely, should the noise parameters of an active device not be available, the noise correlation matrix can be solved in terms of the noise generators, introduced in chapter 2, in order to predict the noise performance of the device as shown in section 3.3. Lastly it will be shown that the correlation matrix can be used to analyse the noise performance of multi-port networks making it possible to derive the mixed-mode noise parameters of a multi-port network as demonstrated in chapter 6.

3.1 Definition of the Correlation Matrix

All linear noisy two-port networks can be replaced by the same linear two-port, taken to be noiseless, with two equivalent noise sources connected to the noiseless network. If the two noise sources, denoted by s_1 and s_2, are considered to be band-limited signals around a stationary frequency with random amplitude and phase, the auto-and cross-spectral power densities of the two sources are defined by the Fourier transform of their auto- and cross-correlation functions, as given in equation 2.1.2. Arranging these auto- and cross-spectral power densities in a matrix form, makes up the correlation matrix

$$\mathbf{C} = \begin{bmatrix} < s_1 s_1^* > & < s_1 s_2^* > \\ < s_2 s_1^* > & < s_2 s_2^* > \end{bmatrix} \tag{3.1.1}$$

From equation 3.1.1 it is apparent that the diagonal of the correlation matrix contains the self-power spectral densities (and therefore only real values), whereas the off-diagonal elements are the cross-power spectral densities which are complex quantities.

With a noisy linear two-port network represented by its noiseless equivalent network and two external noise sources, the noiseless two-port network can be described by various two-port matrices, the most common of which are Impedance (Z), Admittance (Y), or Transmission ($ABCD$) parameters. These two-port networks are referred to as the Impedance, Admittance and Chain representations respectively and the external noise sources for these representations are either in the form of two noise voltage sources (e_{n1} and e_{n2}), two noise current sources (i_{n1} and i_{n2}), or a noise voltage and current source (e_n and i_n), respectively. The three representations with the correlation matrices of their equivalent external noise sources as well as their respective electrical matrices are summarised in table 3.1 [39].

Table 3.1: Three representations of the correlation matrix.

	Impedance Representation	Admittance Representation	Chain Representation
Equivalent Circuit	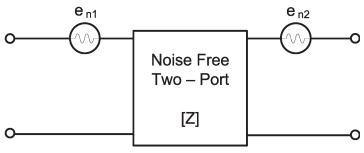	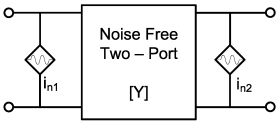	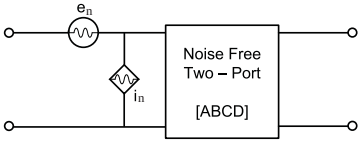
Correlation Matrix	$C_Z = \begin{bmatrix} C_{e_{n_1} e_{n_1}^*} & C_{e_{n_1} e_{n_2}^*} \\ C_{e_{n_2} e_{n_1}^*} & C_{e_{n_2} e_{n_2}^*} \end{bmatrix}$	$C_Y = \begin{bmatrix} C_{i_{n_1} i_{n_1}^*} & C_{i_{n_1} i_{n_2}^*} \\ C_{i_{n_2} i_{n_1}^*} & C_{i_{n_2} i_{n_2}^*} \end{bmatrix}$	$C_A = \begin{bmatrix} C_{e_n e_n^*} & C_{e_n i_n^*} \\ C_{i_n e_n^*} & C_{i_n i_n^*} \end{bmatrix}$
Electrical Matrix	$Z = \begin{bmatrix} z_{11} & z_{12} \\ z_{21} & z_{22} \end{bmatrix}$	$Y = \begin{bmatrix} y_{11} & y_{12} \\ y_{21} & y_{22} \end{bmatrix}$	$A = \begin{bmatrix} a_{11} & a_{12} \\ a_{21} & a_{22} \end{bmatrix}$

Since the two-port networks, shown in table 3.1, are defined by noiseless electrical matrices, transforming the electrical matrices from one representation to another can easily be done by applying the correct set of equations summarized in [15]. Hillbrand and Russer showed that one of the most useful properties of the correlation matrix is the ability to transform between equivalent noise representations, by using extremely simple transformation matrices. Table 3.2 shows a summary of the transformation matrices, $\mathbf{T}$, used to transform the noise sources between representations. To transform correlation matrix $\mathbf{C}_1$ to a different representation $\mathbf{C}_2$, the appropriate transformation matrix, $\mathbf{T}$ is used as follows,

$$\mathbf{C}_2 = \mathbf{T}\mathbf{C}_1\mathbf{T}^\dagger \tag{3.1.2}$$

where the dagger (†) denotes the Hermitian matrix or conjugate-transpose of transformation matrix $\mathbf{T}$. The mean square value of the noise sources of the final representation can then be solved from the transformed correlation matrix using the relation given in equation 2.1.3. Conversely, given that the noise generators within a passive network are all thermal in nature, the impedance and admittance representations of the correlation matrix can readily be solved from the impedance or admittance electrical matrices. That is, for a passive network,

$$\mathbf{C}_Z = kT\left[\mathbf{Z} + \mathbf{Z}^*\right] \tag{3.1.3}$$

$$\mathbf{C}_Y = kT\left[\mathbf{Y} + \mathbf{Y}^*\right] \tag{3.1.4}$$

Table 3.2: Transformation matrices for the three correlation matrix representations.

Resulting Reresentation	Original Representation		
	Admittance	Impedance	Chain
Admittance	$\begin{bmatrix} 1 & 0 \\ 0 & 1 \end{bmatrix}$	$\begin{bmatrix} y_{11} & y_{12} \\ y_{21} & y_{22} \end{bmatrix}$	$\begin{bmatrix} -y_{11} & 1 \\ -y_{21} & 0 \end{bmatrix}$
Impedance	$\begin{bmatrix} z_{11} & z_{12} \\ z_{21} & z_{22} \end{bmatrix}$	$\begin{bmatrix} 1 & 0 \\ 0 & 1 \end{bmatrix}$	$\begin{bmatrix} 1 & -z_{11} \\ 0 & -z_{21} \end{bmatrix}$
Chain	$\begin{bmatrix} 0 & a_{12} \\ 1 & a_{22} \end{bmatrix}$	$\begin{bmatrix} 1 & -a_{11} \\ 0 & -a_{21} \end{bmatrix}$	$\begin{bmatrix} 1 & 0 \\ 0 & 1 \end{bmatrix}$

Two-port networks can often be simplified by describing them as an interconnection of a number of two-ports in either series, parallel or cascade. The correlation matrix can be used to express the resulting noise generated by the composite two-port network. That is, using the appropriate representation, the resulting correlation matrix is related to the original matrices by

$$\mathbf{C}_Z = \mathbf{C}_{Z1} + \mathbf{C}_{Z2} \quad (Series) \tag{3.1.5}$$

$$\mathbf{C}_Y = \mathbf{C}_{Y1} + \mathbf{C}_{Y2} \quad (Parallel) \tag{3.1.6}$$

$$\mathbf{C}_A = \mathbf{A}_1\mathbf{C}_{A2}\mathbf{A}_1^\dagger + \mathbf{C}_{A1} \quad (Cascade) \tag{3.1.7}$$

where subscripts 1 and 2 represent the individual two-ports connected together. Note that for series and parallel interconnections of two-ports, the resulting noise correlation matrices are simply computed as the addition of the individual two-port correlation matrices expressed in impedance and admittance representation, respectively. It is only for cascade interconnections that the correlation matrix of the one two-port needs to be transformed using the transmission (*ABCD*) matrix of the other two-port.

3.2 Correlation matrix in terms of Equivalent two-port Noise Parameters

The noise performance of two-port devices are mostly provided in terms of the four noise parameters introduced in section 2.3. Although these noise parameters (R_n, F_{min}, and Y_{opt}) provide circuit designers with all the necessary information for low noise circuit design, the correlation matrix still gives a more useful description of the noise mechanisms within the two-port network. This section introduces an elegant relation between the noise parameters of a two-port device and the correlation matrix of the chain representation [40].
Figure 3.1 shows the chain representation of a noiseless linear two-port network with noise voltage source, e, and noise current source, i. The spectral power densities of the noise voltage and current sources can be expressed in terms of the noise resistance (R_n) and conductance (G_n), giving

$$< ee^* >= 2kTR_n \tag{3.2.1}$$

$$< ii^* >= 2kTG_n \tag{3.2.2}$$

where noise sources, i and e, are assumed to be partially correlated.

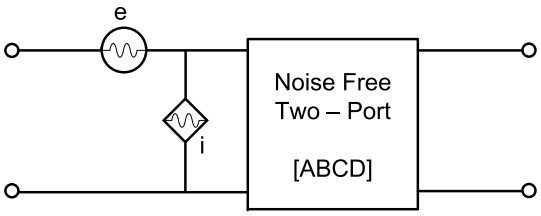

Figure 3.1: Chain representation of a noisy two-port network.

Noise current i can therefore be separated into correlated (i_c) and uncorrelated (i_u) noise sources such that

$$i = i_c + i_u \tag{3.2.3}$$

$$i = Y_c e + i_u \tag{3.2.4}$$

where $Y_c = G_c + jB_c$ is the correlation admittance that characterizes the correlation between e and i. The cross correlated terms of e and i is therefore described by

$$< ei_u^* > = 0 \tag{3.2.5}$$

$$< ei_c^* > =< ei^* >= Y_c^* < ee^* > . \tag{3.2.6}$$

It follows from equation 3.1.1 that

$$\mathbf{C} = < \begin{bmatrix} ee^* & ei^* \\ ie^* & ii^* \end{bmatrix} > \tag{3.2.7}$$

and therefore the correlation matrix is given by

$$\mathbf{C} = 2kT \begin{bmatrix} R_n & R_n Y_c^* \\ R_n Y_c & G_u + R_n |Y_c|^2 \end{bmatrix} \tag{3.2.8}$$

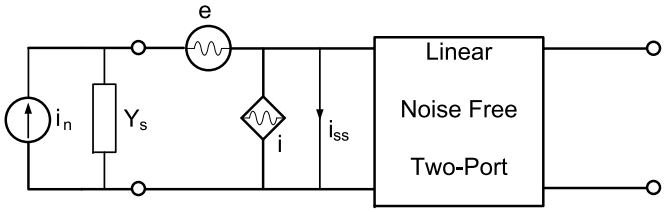

Figure 3.2: Linear noise free two-port shorted at the input.

If this two-port network is driven by a source with admittance Y_s, the noise factor can be computed using equation 2.3.4. In shorting the input of the linear noiseless two-port network, as shown in figure 3.2, the noise figure as considered at the input simplifies to

$$F = \frac{N_{ss}}{N_i} \tag{3.2.9}$$

where N_{ss} and N_i denote the short circuit and input noise powers, respectively. The output noise power is therefore represented by the spectral power density of the short circuited current $< i_{ss} i_{ss}^* >$ with the short circuit noise current equal to

$$i_{ss} = i_n + Y_s e + i \tag{3.2.10}$$

where $< i_n i_n^* >$ is the spectral power density of the noise current due to the source conductance G_s

$$< i_n i_n^* > = 2kTG_s \tag{3.2.11}$$

and describes the input noise power. It is worth noting at this point that the noise from the source, i_n is uncorrelated from the noise generated by the two-port network, e and i. The noise factor can thus be written as

$$F = \frac{< i_{ss} i_{ss}^* >}{< i_n i_n^* >} = \frac{< i_n i_n^* > + < (Y_s e + i)(Y_s e + i)^* >}{< i_n i_n^* >} \tag{3.2.12}$$

where

$$< (Y_s e + i)(Y_s e + i)^* > = < \left(\begin{bmatrix} Y_s & 1 \end{bmatrix} \begin{bmatrix} e \\ i \end{bmatrix} \right) \left(\begin{bmatrix} e & i \end{bmatrix} \begin{bmatrix} Y_s \\ 1 \end{bmatrix} \right)^* > \tag{3.2.13}$$

$$= \begin{bmatrix} Y_s & 1 \end{bmatrix} (\mathbf{C}) \begin{bmatrix} Y_s^* \\ 1 \end{bmatrix} \tag{3.2.14}$$

and correlation matrix $\mathbf{C}$ is given by 3.2.8. Therefore the noise factor can be expressed in terms of the noise correlation matrix and the source admittance

$$F = 1 + \frac{1}{2kTG_s} \begin{bmatrix} Y_s & 1 \end{bmatrix} \mathbf{C} \begin{bmatrix} Y_s^* \\ 1 \end{bmatrix} \tag{3.2.15}$$

where source admittance $Y_s = G_s + jB_s$.

Expanding equation 3.2.15 yields an expression for the noise factor in terms of the noise resistance (R_n), source admittance (Y_s), correlation admittance (Y_c), and the uncorrelated noise conductance (G_u):

$$F = 1 + \frac{\left(G_s^2 + 2G_cG_s + G_c^2 + B_s^2 + 2B_sB_c + B_c^2\right)R_n + G_u}{G_s} \tag{3.2.16}$$

Since the noise factor is a minimum when the two-port is presented with the optimum source admittance, $Y_{opt} = G_{opt} + jB_{opt}$, equation 3.2.16 can be differentiated with respect to G_s and B_s and the optimum source admittance can be calculated by setting the derivatives equal to zero.

$$\frac{\partial F}{\partial B_s} = \frac{(B_s + B_c)R_n}{2G_s} \tag{3.2.17}$$

Therefore the optimum source susceptance for $\frac{\partial F}{\partial B_s} = 0$ is

$$B_{opt} = -B_c \tag{3.2.18}$$

Also

$$\frac{\partial F}{\partial G_s} = \frac{\left(G_s^2 - G_c^2 - B_s^2 - 2B_cB_s - B_c^2\right)R_n - G_u}{G_s^2} \tag{3.2.19}$$

Solving $\frac{\partial F}{\partial G_s} = 0$ and substituting $B_{opt} = -B_c$ gives the optimum source conductance

$$G_{opt} = \sqrt{G_c^2 + \frac{G_u}{R_n}} \tag{3.2.20}$$

The minimum noise figure, F_{min}, is therefore given by

$$F_{min} = 1 + 2R_n\left(G_c + \sqrt{G_c^2 + \frac{G_u}{R_n}}\right) \tag{3.2.21}$$

Using the expressions for G_{opt}, B_{opt}, and F_{min}, the correlation admittance (Y_c) and the uncorrelated real conductance G_u can be solved in terms of the two-port noise parameters.

$$G_u = \frac{(4F_{min} - 4)G_{opt}R_n - F_{min}^2 + 2F_{min} - 1}{4R_n} \tag{3.2.22}$$

$$G_c = -\frac{2G_{opt}R_n - F_{min} + 1}{2R_n} \tag{3.2.23}$$

$$B_c = -B_{opt} \tag{3.2.24}$$

$$Y_c = \frac{F_{min} - 2G_{opt}R_n - 1}{2R_n} - jB_{opt} \tag{3.2.25}$$

Substituting these expressions into equation 3.2.8 gives the expression for the chain representation of the noise correlation matrix in terms of the two-port noise parameters

$$\mathbf{C} = 2kT\begin{bmatrix} R_n & \frac{F_{min}-1}{2} - R_nY_{opt}^* \\ \frac{F_{min}-1}{2} - R_nY_{opt} & R_n|Y_{opt}|^2 \end{bmatrix} \tag{3.2.26}$$

Using equations 3.2.26 and 3.1.1 the auto- and cross-spectral power densities of the noise voltage and current sources for the equivalent noiseless chain representation, can be derived from the two-port noise parameters.

3.3 Correlation matrix in terms of Noise Generators

Section 3.2 derived an expression for the noise correlation matrix in terms of the noise parameters of a linear two-port network. However, the noise parameters of the two-port network might not always be available and therefore the correlation matrix may need to be derived from the physical parameters of the two-port network. This process is illustrated using the small signal model of a BJT [40].

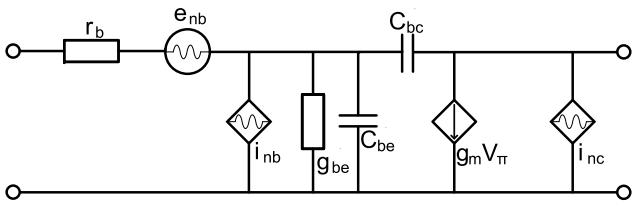

Figure 3.3: Noisy small signal model of a BJT.

Figure 3.3 shows the two-port representation of the small signal model for a BJT including: base-emitter and base-collector capacitances (C_{be} and C_{bc}), base spreading resistance (r_b), and the base-emitter conductance (g_{be}). Also included in the model are the noise current and voltage sources, i_{nb}, i_{nc}, and e_{nb}. As described in section 2.1 the noise current sources are modelled as shot noise sources, dependent on the base and collector DC biasing currents, whereas the noise voltage is modelled as a thermal noise source dependent on the base spreading resistance, with mean square values

$$\overline{i_{nb}}^2 = 2qI_b\Delta f \tag{3.3.1}$$

$$\overline{i_{nc}}^2 = 2qI_c\Delta f \tag{3.3.2}$$

$$\overline{e_{nb}}^2 = 4kTr_b\Delta f \tag{3.3.3}$$

Recalling that the transconductance (g_m) of a BJT is given by

$$g_m = \frac{I_c}{V_T} \tag{3.3.4}$$

where V_T is the thermal voltage equal to

$$V_T = \frac{kT}{q} \tag{3.3.5}$$

the spectral densities of shot noise sources can be expressed as

$$< i_{nb}i_{nb}^* > = \frac{kTg_m}{\beta} \tag{3.3.6}$$

$$< i_{nc}i_{nc}^* > = kTg_m \tag{3.3.7}$$

The circuit shown in figure 3.3 can be separated into two two-port networks as shown in figure 3.4.
Since the first two-port is a passive network, it follows from equation 3.1.4 that the correlation matrix is given by

$$\mathbf{C}_{Y1} = 2kT\Re\{\mathbf{Y1}\}. \tag{3.3.8}$$

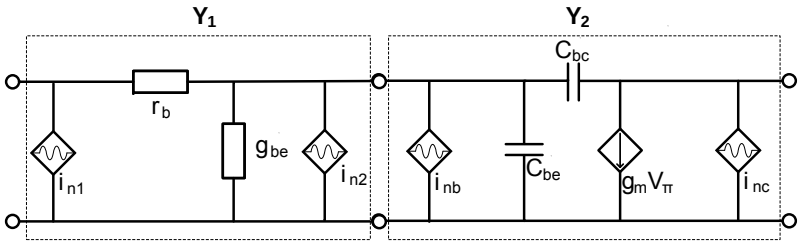

Figure 3.4: Hybrid-pi model separated into two cascaded noise free two-port networks in admittance representation.

The correlation matrix of the second two-port is deduced from equation 3.1.1 as

$$\mathbf{C}_{Y2} = \begin{bmatrix} < i_{nb} i_{nb}^* > & < i_{nb} i_{nc}^* > \\ < i_{nc} i_{nb}^* > & < i_{nc} i_{nc}^* > \end{bmatrix} \tag{3.3.9}$$

where the cross-correlation terms $< i_{nb} i_{nc}^* >$ and $< i_{nc} i_{nb}^* >$ are equal to zero, since noise sources i_{nb} and i_{nc} are uncorrelated. In order to find the correlation matrix of the resulting network obtained by cascading the two-ports, both need to be transformed to the chain representation using the transformations illustrated in table 3.2. That is

$$\mathbf{C}_{Ci} = \mathbf{T}_i \mathbf{C}_{Yi} \mathbf{T}_i^\dagger \tag{3.3.10}$$

$$\mathbf{T}_i = \begin{bmatrix} 0 & B_i \\ 1 & D_i \end{bmatrix} \quad \text{i} = 1,2 \tag{3.3.11}$$

The resulting transmission matrix ($\mathbf{A}_f$) and chain correlation matrix ($\mathbf{C}_{Cf}$) can then be calculated to describe the noiseless linear two-port as shown in figure 3.1

$$\mathbf{A}_f = \mathbf{A}_1 \mathbf{A}_2 \tag{3.3.12}$$

$$\mathbf{C}_{Cf} = \mathbf{A}_1 \mathbf{C}_{C2} \mathbf{A}_1^\dagger + \mathbf{C}_{C1}. \tag{3.3.13}$$

Finally, using the relationship described by equation 3.2.26, the correlation matrix $\mathbf{C}_{Cf}$ can be used to calculate the noise parameters of the two-port network

$$R_n = \frac{C_{ee^*}}{2kT} \tag{3.3.14}$$

$$Y_{opt} = \sqrt{\frac{C_{ii^*}}{C_{ee^*}} - \left[\Im\left(\frac{C_{ei^*}}{C_{ee^*}}\right)\right]^2} + j\Im\left(\frac{C_{ei^*}}{C_{ee^*}}\right) \tag{3.3.15}$$

$$F_{min} = 1 + \frac{C_{ei^*} + C_{ee^*} Y_{opt}}{kT} \tag{3.3.16}$$

It is clear from this section that the noise correlation matrix significantly simplifies the noise analysis of noisy two-port networks. This is even more true for multi-port networks.

3.4 Multi-Port Networks

All multi-port networks can be represented as a number of embedded active devices encased in a lossy and noisy passive network. As a special case of this, consider an n-port multi-port network with m embedded two-port active devices as shown in figure 3.5 [41].

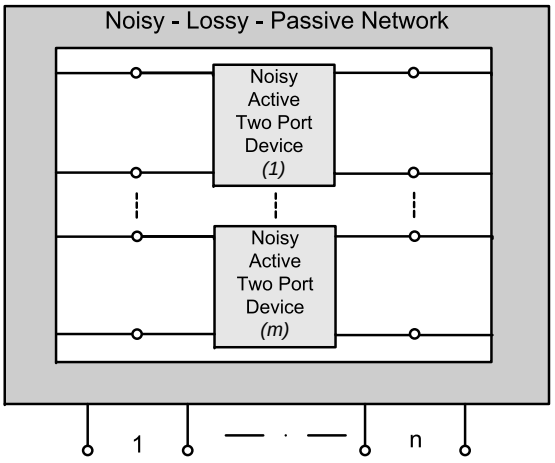

Figure 3.5: n-Port network with m embedded active devices.

Assuming that each active device is characterized as a two-port network with corresponding admittance (Y) and noise parameters (R_n,Y_{opt}, and F_{min}), the noisy network can be replaced with its noiseless Norton equivalent counterpart shown in figure 3.6.

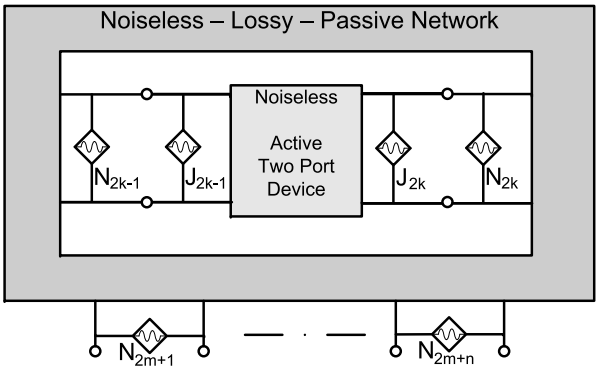

Figure 3.6: Noise free multi-port network with internal equivalent noise sources.

As figure 3.6 shows, the equivalent circuit contains two independent sets of noise sources, N and J. Here noise sources represented by N are all the equivalent noise generators of the passive network and are therefore thermal in nature as well as correlated. The correlation matrix for the N sources is given by

$$\mathbf{C}_N = kT\{\mathbf{Y} + \mathbf{Y}^*\} \tag{3.4.1}$$

where $\mathbf{Y}$ represents the $(2m+n)\times(2m+n)$ admittance matrix of the passive network. The J sources are the equivalent noise generators of the embedded two-port networks, as determined from their noise parameters,

and therefore usually not thermal in nature. Only sources from the same two-port device are assumed to be correlated, ie. J_{2k-1} and J_{2k} are correlated.
Using the given noise parameters of the embedded two-port devices, the chain representation of the correlation matrix can be determined from equation 3.2.26. It is therefore necessary to derive an expression for the admittance representation of the correlation matrix in terms of the two-port noise parameters.

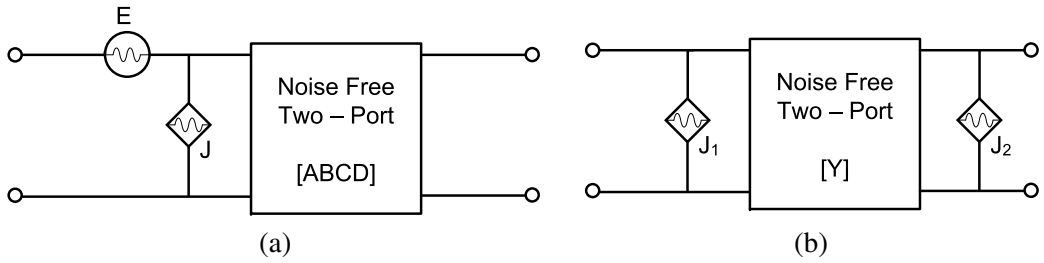

Figure 3.7: Chain (a) and Admittance (b) two-port representations.

Figure 3.7 depicts the required transformation. Since sources J and E are correlated

$$J = J_u + Y_c E \tag{3.4.2}$$

where the subscript u represents the uncorrelated noise. Therefore, from inspection it is found that

$$J_1 = J - y_{11} E \tag{3.4.3}$$

$$J_2 = -y_{21} E \tag{3.4.4}$$

where $y11$ and $y21$ are admittance parameters of the embedded noiseless two-port. As defined in section 3.2 the spectral power densities of noise sources E and J are

$$< EE^* > = 2kTR_n \tag{3.4.5}$$

$$< JJ^* > = < (J_u + Y_c E)(J_u + Y_c E)^* > = 2kT\left(G_u + |Y_c|^2 R_n\right) \tag{3.4.6}$$

Using the set of equations listed above, the correlation matrix of the admittance representation is calculated as

$$\mathbf{C}_J = \begin{bmatrix} < J_1 J_1^* > & < J_1 J_2^* > \\ < J_2 J_2^* > & < J_2 J_2^* > \end{bmatrix} \tag{3.4.7}$$

$$\mathbf{C}_J = 2kT \begin{bmatrix} G_u + |y_{11} - Y_c|^2 R_n & y_{21}^* (y_{11} - Y_c) R_n \\ y_{21} (y_{11} - Y_c)^* R_n & |y_{21}| R_n \end{bmatrix} \tag{3.4.8}$$

Note that the values of G_u and Y_c are calculated from the two-port noise parameters as in equations 3.2.22 and 3.2.25, respectively.

The $(2m+n)\times(2m+n)$ admittance matrix of the passive network encasing the m active devices can be subdivided as follow

$$\mathbf{Y} = \begin{bmatrix} \mathbf{Y}_{ii} & \mathbf{Y}_{ie} \\ \mathbf{Y}_{ei} & \mathbf{Y}_{ee} \end{bmatrix} \tag{3.4.9}$$

where the subscript i refers to the $2m$ internal device ports and subscript e refers to the n external ports. The network equations for the equivalent multi-port network shown in figure 3.6 is therefore given by

$$\mathbf{I}_i = \mathbf{Y}_{ii}\mathbf{V}_i + \mathbf{Y}_{ie}\mathbf{V}_e + \mathbf{N}_i \tag{3.4.10}$$

$$\mathbf{I}_e = \mathbf{Y}_{ei}\mathbf{V}_i + \mathbf{Y}_{ee}\mathbf{V}_e + \mathbf{N}_e \tag{3.4.11}$$

$$\mathbf{I}_i = -\mathbf{y}\mathbf{V}_i - \mathbf{J} \tag{3.4.12}$$

where the admittance matrix $\mathbf{y}$ in equation 3.4.12 is the diagonal sum of all the individual two-port device admittance matrices

$$\mathbf{y} = \begin{bmatrix} [\mathbf{y}_1] & \cdots & 0 \\ \vdots & \ddots & \vdots \\ 0 & \cdots & [\mathbf{y}_m] \end{bmatrix} \tag{3.4.13}$$

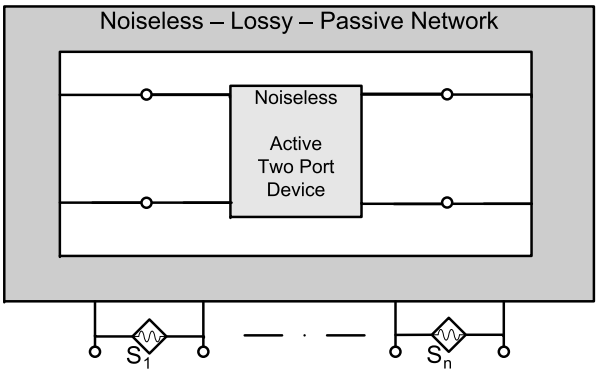

Figure 3.8: Noise free multi-port network with only n external equivalent noise sources.

To represent the multi-port network as a noiseless network with equivalent noise sources at the external ports, the external ports are shorted ($\mathbf{V}_e = 0$). The equivalent noiseless network is shown in figure 3.8. Note that the external port currents $\mathbf{I}_e$ are now represented by $\mathbf{S}$, such that

$$-\mathbf{y}\mathbf{V}_i - \mathbf{J} = \mathbf{Y}_{ii}\mathbf{V}_i + \mathbf{N}_i \tag{3.4.14}$$

$$\mathbf{S} = \mathbf{Y}_{ei}\mathbf{V}_i + \mathbf{N}_e \tag{3.4.15}$$

Equations 3.4.14 and 3.4.15 can be used to solve $\mathbf{S}$, giving

$$\mathbf{S} = \mathbf{H}_N\mathbf{N} + \mathbf{H}_J\mathbf{J} \tag{3.4.16}$$

where $\mathbf{N}$ is a noise vector containing all the noise sources at the internal device ports and external network ports

$$\mathbf{N} = \begin{bmatrix} \mathbf{N}_i \\ \mathbf{N}_e \end{bmatrix} \tag{3.4.17}$$

and

$$\mathbf{H}_J = -\mathbf{Y}_{ei}\left(\mathbf{Y}_{ii}+\mathbf{y}\right)^{-1} \tag{3.4.18}$$

$$\mathbf{H}_N = [\mathbf{H}_J|\mathbf{I}_n] \tag{3.4.19}$$

where $\mathbf{I}_n$ represents an identity matrix of order n.
Since noise sources N and J are taken to be uncorrelated, the two terms $\mathbf{H}_N\mathbf{N}$ and $\mathbf{H}_J\mathbf{J}$ can be superimposed in power, giving the spectral power density

$$<\mathbf{SS}^*>=\mathbf{H}_N<\mathbf{NN}^*>\mathbf{H}_N^\dagger+\mathbf{H}_J<\mathbf{JJ}^*>\mathbf{H}_J^\dagger \tag{3.4.20}$$

It then follows from equations 3.1.1, 3.4.1 and 3.4.8 that the correlation matrix of the multi-port network is given by

$$\mathbf{C}_{SS} = \mathbf{H}_N\mathbf{C}_N\mathbf{H}_N^\dagger+\mathbf{H}_J\mathbf{C}_{J_T}\mathbf{H}_J^\dagger \tag{3.4.21}$$

where $\mathbf{C}_{J_T}$ is the diagonal sum of the correlation matrices of the m embedded two-port devices,

$$\mathbf{C}_{J_T} = \begin{bmatrix} [\mathbf{C}_{J1}] & \cdots & 0 \\ \vdots & \ddots & \vdots \\ 0 & \cdots & [\mathbf{C}_{Jm}] \end{bmatrix} \tag{3.4.22}$$

Finally the overall n port admittance matrix is determined by

$$\mathbf{Y}_n = \mathbf{Y}_{ee}+\mathbf{H}_J\mathbf{Y}_{ie} \tag{3.4.23}$$

Determining the noise factor of the multi-port network involves investigating the degradation of the signal to noise ratio caused by the network as a signal passes from an input port p to an output port q. This can be represented as

$$F_{qp} = 1+\frac{\text{Noise power at } q \text{ due to the network}}{\text{Noise power at } q \text{ due to source at } p} \tag{3.4.24}$$

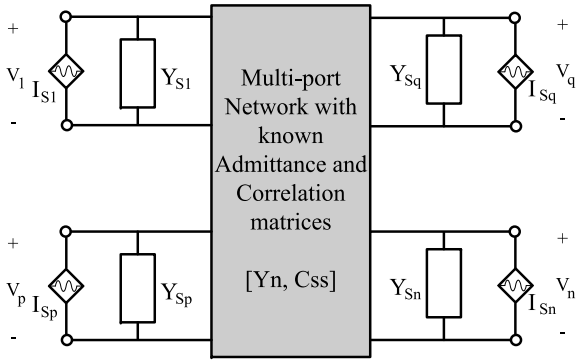

Figure 3.9: Noise free multi-port network with each port driven by a source.

To calculate the noise figure, consider the admittance matrix of the multi-port network with all n ports loaded by source admittance Y_{s_n}, as shown in figure 3.9. The new loaded admittance matrix is then given by

$$\mathbf{Y}_{n_L} = \mathbf{Y}_n+\mathbf{Y}_{s_n}\mathbf{I}_n \tag{3.4.25}$$

and the loaded impedance matrix of the n port network is simply the inverse

$$\mathbf{Z}_{n_L} = (\mathbf{Y}_{n_L})^{-1} = \begin{bmatrix} \mathbf{Z}_{e1} \\ \mathbf{Z}_{e2} \\ \vdots \\ \mathbf{Z}_{en} \end{bmatrix} \tag{3.4.26}$$

where $\mathbf{Z}_{en}$ denotes a row vector described by

$$\mathbf{Z}_{e_n} = \begin{bmatrix} Z_{n1} & Z_{n2} & \cdots \end{bmatrix} \tag{3.4.27}$$

Consider the noise power delivered to port q due to the network. The voltage at port q, $\mathbf{V}_q$ is represented by the vector equation

$$[\mathbf{V}_q] = -[\mathbf{Z}_{eq}][\mathbf{S}] \tag{3.4.28}$$

with $\mathbf{S}$ being the vector containing the n external equivalent noise sources as described in equation 3.4.16. The noise power due to the network delivered to port q is then given by

$$\mathbf{P}_{qn} = < \mathbf{V}_q \mathbf{V}_q^* > \Re\{Y_{sq}\} \tag{3.4.29}$$

and, since

$$< \mathbf{V}_q \mathbf{V}_q^* > = \mathbf{Z}_{eq} < \mathbf{S}\mathbf{S}^* > \mathbf{Z}_{eq}^\dagger \tag{3.4.30}$$

the noise power $\mathbf{P}_{qn}$ can be expressed in terms of the noise correlation matrix

$$\mathbf{P}_{qn} = [\mathbf{Z}_{eq}]\, 2\mathbf{C}_{SS}\, [\mathbf{Z}_{eq}]^\dagger \Re\{Y_{sq}\} \tag{3.4.31}$$

The noise power at port q due to the source at port p is equal to

$$\mathbf{P}_{qp} = < \mathbf{V}_{qp} \mathbf{V}_{qp}^* > \Re\{Y_{sq}\} \tag{3.4.32}$$

where the mean square of the noise voltage V_{qp} produced at port q, due to the noise source input i_{sp} at port p, is given by

$$< V_{qp} V_{qp}^* > = |Z_{qp}|^2 < i_{sp} i_{sp}^* > \tag{3.4.33}$$

Noting that the spectral power density of the noise source at port p is equal to

$$< i_{sp} i_{sp}^* > = 2kT\Re\{Y_{sp}\} \tag{3.4.34}$$

the noise power due to the noise source at port p can be expressed by

$$P_{qp} = |Z_{qp}|^2 4kT\Re\{Y_{sp}\}\Re\{Y_{sq}\} \tag{3.4.35}$$

The noise figure calculated from port p to port q is therefore solved, in terms of the multi-port noise correlation matrix, by

$$F_{qp} = 1 + \frac{[\mathbf{Z}_{eq}]\, \mathbf{C}_{SS}\, [\mathbf{Z}_{eq}]^\dagger}{|Z_{qp}|^2 4kT\Re\{Y_{sp}\}} \tag{3.4.36}$$

When a network consists of multiple input and output ports differential- and common-mode (mixed-mode) signals can propagate between coupled ports (The theory of mixed-mode signal propagation is discussed in Chapter 4). Using the noise correlation matrix, three- or four-port networks can be transformed into two equivalent noiseless two-port networks, one for each mode of propagation. Section 6.2.6 derives the differential noise parameters of a three-port network by means of the mixed-mode correlation matrix.

3.5 Conclusion

This chapter illustrates the importance of the noise correlation matrix when investigating the noise performance of both two-port and multi-port networks. The three two-port representations introduced in section 3.1 make this theory applicable to any noisy linear two-port network and the transformations summarised in table 3.2 significantly simplifies two-port noise analysis by allowing networks to be considered as the interconnection of simpler two-port networks. Lastly the direct relationship between the noise parameters of a two-port device and the elements of the correlation matrix of the chain representation proves to be extremely useful when analysing the noise performance of mixed-mode propagation in multi-port networks (refer to chapter 6).

Chapter 4

Transmission Line Theory

Single-ended circuits operating at microwave frequencies are commonly characterised by their Scattering (S)-parameters. When working with differential circuits, the important characteristics are however in terms of combinations of standard S-parameters. A number of advantages can be achieved by defining an alternative set of S-parameters, the so called Mixed-Mode S-paramters. Bockelman and Eisenstadt were the first to introduce mixed-mode S-parameters for differential circuits, based on the two propagation modes that co-exist on pairs of coupled transmission lines [42]. This chapter applies general transmission line theory to coupled transmission lines in order to derive expressions for the differential- and common-mode waves propagating on the lines. These expressions are then used to find a transformation matrix that can be used to transform the general S-parameters of a four-port network into the equivalent mixed-mode S-parameters.

4.1 Generalized Scattering Parameters

Measuring the voltages and currents of microwave networks and their related impedance and admittance matrices can prove to be a difficult task, since it involves the measurement of the magnitude and phase of a wave propagating in a certain direction. Scattering parameters, on the other hand, relate the incident voltage waves at the network ports to the waves reflected from the ports and can easily be calculated using network analysis techniques or measured using a vector network analyzer. To derive expressions for the S-parameters, consider the N-port network, shown in figure 4.1, with arbitrary characteristic impedances [15]. The port voltages and currents can be defined in terms of their incident and reflected components. That is,

$$V_n = V_n^+ + V_n^- \tag{4.1.1}$$

$$I_n = I_n^+ - I_n^- \tag{4.1.2}$$

where the superscripts $+$ and $-$ indicate the incident and reflected waves, respectively. Given that the incident and reflected voltage and current are related to one another by,

$$V_n^+ = Z_{0_n}^* I_n^+ \tag{4.1.3}$$

$$V_n^- = Z_{0_n} I_n^- \tag{4.1.4}$$

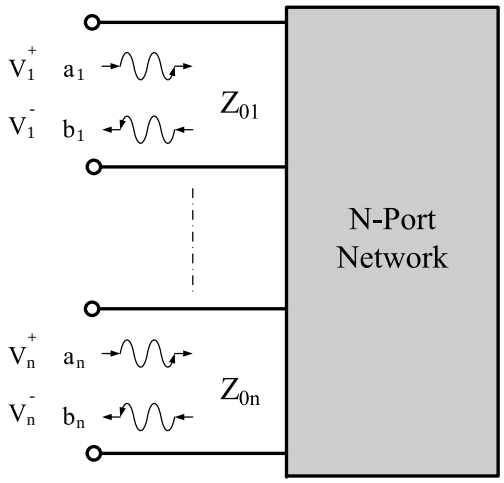

Figure 4.1: Generalized multi-port network showing incident and reflected waves.

where Z_{0_n} is the characteristic port impedance, the current at port n, as defined by equation 4.1.2, can be expressed in terms of the incident and reflected voltages

$$I_n = \frac{V_n^+}{Z_{0_n}^*} - \frac{V_n^-}{Z_{o_n}} \tag{4.1.5}$$

Therefore the reflected voltage is given by

$$V_n^- = \frac{Z_{0_n}}{Z_{0_n}^*} V_n^+ - I_n Z_{o_n} \tag{4.1.6}$$

Substituting equation 4.1.6 into equation 4.1.1, yields an expression for the incident voltage wave:

$$V_n^+ = \frac{Z_{0_n}^*}{2\Re\left(Z_{0_n}\right)} \left(V_n + I_n Z_{o_n}\right) \tag{4.1.7}$$

It is convenient to define a new set of normalized incident and reflected wave amplitudes as the square root of the incident and reflected power at port n, respectively

$$a_n = \frac{\sqrt{Z_{0_n} + Z_{0_n}^*}}{\sqrt{2}} I_n^+ \tag{4.1.8}$$

$$= \sqrt{\Re(Z_{0_n})} I_n^+ \tag{4.1.9}$$

$$= \frac{\sqrt{\Re(Z_{0_n})}}{Z_{0_n}^*} V_n^+ \tag{4.1.10}$$

$$b_n = \frac{\sqrt{Z_{0_n} + Z_{0_n}^*}}{\sqrt{2}} I_n^- \tag{4.1.11}$$

$$= \sqrt{\Re(Z_{0_n})} I_n^- \tag{4.1.12}$$

$$= \frac{\sqrt{\Re(Z_{0_n})}}{Z_{0_n}} V_n^- \tag{4.1.13}$$

Substituting equation 4.1.7 into equation 4.1.10, the incident wave at port n can be expressed in terms of the port voltage, current and characteristic impedance

$$a_n = \frac{V_n + I_n Z_{o_n}}{2\sqrt{\Re(Z_{o_n})}} \tag{4.1.14}$$

Similarly the reflected power wave can be shown to equal

$$b_n = \frac{V_n - I_n Z_{o_n}^*}{2\sqrt{\Re(Z_{o_n})}} \tag{4.1.15}$$

The generalized scattering matrix can then be used to relate the reflected waves to the incident waves

$$[b] = [S]\,[a] \tag{4.1.16}$$

where $[S]$ is the n x n scattering matrix and $[b]$ and $[a]$ are the n x 1 reflected and incident wave vectors respectively [15].

4.2 Mixed-Mode Scattering Parameters

With the generalized S-parameters defined the mixed-mode scattering parameters can now be derived. The theory of coupled transmission lines are used in many applications, including the synthesis of filters, directional couplers and matching networks. Using the method developed by Bockelman and Eisenstadt in [42], the mixed-mode S-parameters are derived considering coupled transmission lines connected to the input and output of an arbitrary DUT, as shown in figure 4.2. Therefore the theory of operation of coupled transmission lines are discussed in sections 4.2.1 and 4.2.2.

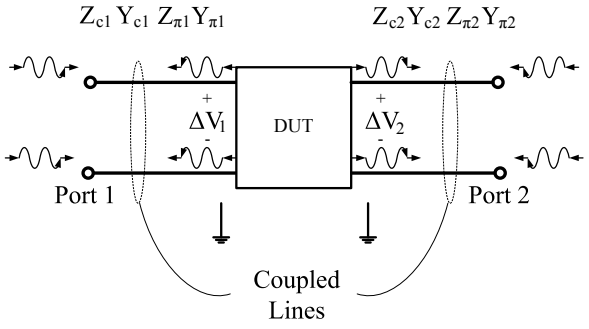

Figure 4.2: Differential two-port network with coupled lines connected to the input and output of the DUT.

4.2.1 Coupled Transmission lines: Even and Odd mode Propagation

The voltage and currents on two coupled transmission lines can be described by two fundamental modes of propagation. Figure 4.3 shows the transverse field distribution for the in-phase (c-mode) and anti-phase (π-mode) propagation on a pair of asymmetric coupled transmission lines in an inhomogeneous dielectric medium.

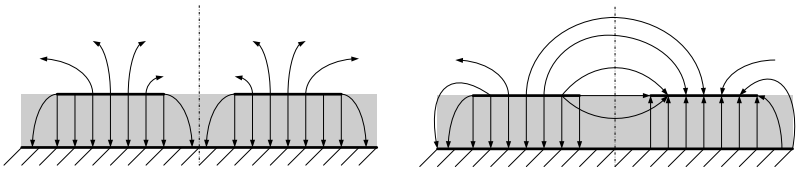

Figure 4.3: Electric field lines showing (a) Even and (b) Odd mode propagation.

The voltage on each line can be expressed in terms of the four voltage waves propagating on the lines - the incident and reflected c- and π-mode voltage waves. Given that, in an inhomogeneous dielectric medium each of the fundamental modes propagate at a different phase velocity, the line voltages are

$$v_1 = A_1 e^{-\gamma_c z} + A_2 e^{\gamma_c z} + A_3 e^{-\gamma_\pi z} + A_4 e^{\gamma_\pi z} \tag{4.2.1}$$

$$v_2 = A_1 R_c e^{-\gamma_c z} + A_2 R_c e^{\gamma_c z} + A_3 R_\pi e^{-\gamma_\pi z} + A_4 R_\pi e^{\gamma_\pi z} \tag{4.2.2}$$

where, A_1 and A_3, and, A_2 and A_4, represent the phasor coefficients of the c- and π-mode propagation in the positive and in the negative z directions, γ_c and γ_π are the c- and π-mode propagation constants, and R_c and R_π denote constants defined in terms of the self and mutual-per unit length-impedances of the lines [43]. The corresponding currents on the lines due to the four waves, can be expressed as

$$i_1 = \frac{A_1}{Z_{c_1}} e^{-\gamma_c z} - \frac{A_2}{Z_{c_1}} e^{\gamma_c z} + \frac{A_3}{Z_{\pi_1}} e^{-\gamma_\pi z} - \frac{A_4}{Z_{\pi_1}} e^{\gamma_\pi z} \tag{4.2.3}$$

$$i_2 = \frac{A_1}{Z_{c_2}} R_c e^{-\gamma_c z} - \frac{A_2}{Z_{c_2}} R_c e^{\gamma_c z} + \frac{A_3}{Z_{\pi_2}} R_\pi e^{-\gamma_\pi z} - \frac{A_4}{Z_{\pi_2}} R_\pi e^{\gamma_\pi z} \tag{4.2.4}$$

where Z_{c_1}, Z_{c_2}, Z_{π_1}, and Z_{π_2} denote the ground referenced characteristic impedance of each line for the c- and π-modes, respectively. The equations for the line voltages and currents can be simplified by assuming symmetric coupled transmission lines. It then follows that constants

$$R_c = +1 \tag{4.2.5}$$

$$R_\pi = -1 \tag{4.2.6}$$

and the c- and π-modes correspond to the even and odd modes, first introduced by Cohn in [44]. Thus, for symmetric coupled transmission lines in an inhomogeneous dielectric medium, the ground referenced characteristic impedances

$$Z_{c_1} = Z_{c_2} = Z_{0_e} \tag{4.2.7}$$

$$Z_{\pi_1} = Z_{\pi_2} = Z_{0_o} \tag{4.2.8}$$

and propagation constants

$$\gamma_c = \gamma_e \tag{4.2.9}$$

$$\gamma_\pi = \gamma_o \tag{4.2.10}$$

where subscripts e and o refer to even and odd mode propagation, respectively. It is worth noting that for a homogeneous dielectric medium the even and odd mode propagation constants can be considered equal. That is,

$$\gamma_c = \gamma_e = \gamma \tag{4.2.11}$$

However, for the derivation of the mixed-mode S-parameters a pair of symmetric, coupled transmission lines in an inhomogeneous dielectric medium are considered and the voltages and currents on two lines, shown in figure 4.4, are therefore given by

$$v_1 = A_1 e^{-\gamma_e z} + A_2 e^{\gamma_e z} + A_3 e^{-\gamma_o z} + A_4 e^{\gamma_o z} \tag{4.2.12}$$

$$v_2 = A_1 e^{-\gamma_e z} + A_2 e^{\gamma_e z} - A_3 e^{-\gamma_o z} - A_4 e^{\gamma_o z} \tag{4.2.13}$$

$$i_1 = \frac{A_1}{Z_{0_e}} e^{-\gamma_e z} - \frac{A_2}{Z_{0_e}} e^{\gamma_e z} + \frac{A_3}{Z_{0_o}} e^{-\gamma_o z} - \frac{A_4}{Z_{0_o}} e^{\gamma_o z} \tag{4.2.14}$$

$$i_2 = \frac{A_1}{Z_{0_e}} e^{-\gamma_e z} - \frac{A_2}{Z_{0_e}} e^{\gamma_e z} - \frac{A_3}{Z_{0_o}} e^{-\gamma_o z} + \frac{A_4}{Z_{0_o}} e^{\gamma_o z} \tag{4.2.15}$$

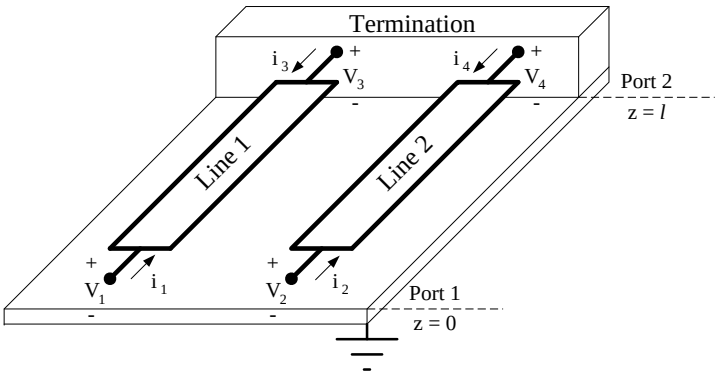

Figure 4.4: Symmetric, terminated, coupled transmission lines over a ground plane.

4.2.2 Coupled Transmission lines: Differential- and Common-mode Signals

In order to derive the mixed-mode scattering parameters the differential- and common-mode voltages and currents between the two coupled transmission lines have to be described in terms of the even and odd mode propagating waves [42]. The differential-mode voltage is defined as the difference in voltage at any point z between lines 1 and 2,

$$v_{dm}(z) = v_1(z) - v_2(z) \tag{4.2.16}$$

Therefore, the differential-mode voltage is no longer referenced to ground, implying that the differential-mode current flowing into one line exits the other line:

$$i_{dm}(z) = \frac{1}{2}\left(i_1(z) - i_2(z)\right) \tag{4.2.17}$$

The common-mode voltage is given by the average voltage at a point z along the line

$$v_{cm}(z) = \frac{1}{2}\left(v_1(z) + v_2(z)\right) \tag{4.2.18}$$

Thus the common-mode current is defined as the total current flowing into the port, and returns via the ground plane:

$$i_{cm}(z) = i_1(z) + i_2(z) \tag{4.2.19}$$

Let $v_o^f(z)$ and $v_o^r(z)$ represent the forward and reverse propagating odd mode waves respectively and $v_e^f(z)$ and $v_e^r(z)$ the forward and reverse propagating even mode waves:

$$v_e^f(z) = A_1 e^{-\gamma_e z} \tag{4.2.20}$$

$$v_e^r(z) = A_2 e^{\gamma_e z} \tag{4.2.21}$$

$$v_o^f(z) = A_3 e^{-\gamma_o z} \tag{4.2.22}$$

$$v_o^r(z) = A_4 e^{\gamma_o z} \tag{4.2.23}$$

Similarly, from equations 4.2.14 and 4.2.15

$$i_e^f(z) = \frac{A_1}{Z_{0_e}} e^{-\gamma_e z} \tag{4.2.24}$$

$$i_e^r(z) = \frac{A_2}{Z_{0_e}} e^{\gamma_e z} \tag{4.2.25}$$

$$i_o^f(z) = \frac{A_3}{Z_{0_o}} e^{-\gamma_o z} \tag{4.2.26}$$

$$i_o^r(z) = \frac{A_4}{Z_{0_o}} e^{\gamma_e z} \tag{4.2.27}$$

From equations 4.2.12 to 4.2.15, the differential-mode voltage and current defined in equations 4.2.16 and 4.2.17 can be expressed as:

$$v_{dm}(z) = 2\left[v_o^f(z) + v_o^r(z)\right] \tag{4.2.28}$$

$$i_{dm}(z) = \frac{1}{Z_{0_o}}\left[v_o^f(z) - v_o^r(z)\right] \tag{4.2.29}$$

Also, the common-mode voltage and current expressed by equations 4.2.18 and 4.2.19 are given by

$$v_{cm}(z) = \left[v_e^f(z) + v_e^r(z)\right] \tag{4.2.30}$$

$$i_{cm}(z) = \frac{2}{Z_{0_e}}\left[v_e^f(z) - v_e^r(z)\right] \tag{4.2.31}$$

It can be noted from the above sets of equations that differential-mode signals are only defined by odd mode propagation whereas common-mode signals are only defined by even-mode propagation.
Considering only the forward propagating part of the differential- and common-mode voltages and currents, the differential- and common-mode characteristic impedances can be determined in terms of the ground referenced even and odd mode characteristic impedances:

$$Z_{dm} = \frac{v_{dm}^f}{i_{dm}^f} = 2Z_{0_o} \tag{4.2.32}$$

$$Z_{cm} = \frac{v_{cm}^f}{i_{cm}^f} = \frac{Z_{0_e}}{2} \tag{4.2.33}$$

It should also be noted that, in general, the even and odd mode characteristic impedances are not equal.
With the differential- and common-mode voltages, currents, and characteristic impedances defined, the mixed-mode power waves at the n^{th} port can be defined. In a similar fashion to equations 4.1.14 and 4.1.15 the amplitude of the differential wave propagating in the positive z direction can be expressed as

$$a_{dm_n}|_{z=0} = \frac{1}{2\sqrt{\Re(Z_{dm})}}\left[v_{dm}(z) + i_{dm}(z)Z_{dm}\right]|_{z=0} \tag{4.2.34}$$

and the differential wave propagating in the negative z direction as

$$b_{dm_n}|_{z=0} = \frac{1}{2\sqrt{\Re(Z_{dm})}}\left[v_{dm}(z) - i_{dm}(z)Z_{dm}^*\right]|_{z=0} \tag{4.2.35}$$

Similarly, the common-mode waves at port n are

$$a_{cm_n}|_{z=0} = \frac{1}{2\sqrt{\Re(Z_{cm})}}\left[v_{cm}(z) + i_{cm}(z)Z_{cm}\right]_{z=0} \tag{4.2.36}$$

$$b_{cm_n}|_{z=0} = \frac{1}{2\sqrt{\Re(Z_{cm})}}\left[v_{cm}(z) - i_{cm}(z)Z_{cm}^*\right]|_{z=0} \tag{4.2.37}$$

As done in section 4.1, the mixed mode reflected waves at ports 1 and 2 of the differential network shown in figure 4.2, can be related to the incident waves by means of the mixed-mode scattering matrix,

$$\begin{bmatrix} b_{dm_1} \\ b_{dm_2} \\ b_{cm_1} \\ b_{cm_2} \end{bmatrix} = \begin{bmatrix} S_{dd} & S_{dc} \\ S_{cd} & S_{cc} \end{bmatrix} \begin{bmatrix} a_{dm_1} \\ a_{dm_2} \\ a_{cm_1} \\ a_{cm_2} \end{bmatrix} \tag{4.2.38}$$

where S_{dd} denotes the differential-mode S-parameters, S_{cc} denotes the common-mode S-parameters, and S_{cd} and S_{dc} the cross-mode S-parameters describing the conversion of differential-mode signals into common-mode signals and vice versa.

Thus, the differential two port, consisting of four terminals, can be described in terms of the mixed-mode scattering parameters [45]:

$$[\mathbf{b}_{mm}] = [\mathbf{S}_{mm}]\,[\mathbf{a}_{mm}] \tag{4.2.39}$$

where $\mathbf{b}_{mm}$ and $\mathbf{a}_{mm}$ are the 4 x 1 reflected and incident mixed-mode wave vectors as used in equation 4.2.38, and $\mathbf{S}_{mm}$ is the 4 x 4 mixed-mode S-parameter matrix.

4.3 Mixed-mode Scattering Parameters derived from General Scattering Parameters

In many circuits, differential circuits are not driven by coupled lines. To analyse this, the distance between the two coupled lines is increased to infinity, resulting in

$$Z_{0_e} = Z_{0_o} = Z_0 \tag{4.3.1}$$

where Z_0 is the characteristic impedance of one line. From equations 4.1.14 and 4.1.15 the normalized incident and reflected waves at each terminal are given by

$$a_i = \frac{1}{2\sqrt{\Re(Z_0)}}\left[v_i + i_i Z_0\right] \tag{4.3.2}$$

$$b_i = \frac{1}{2\sqrt{\Re(Z_0)}}\left[v_i - i_i Z_0^*\right] \tag{4.3.3}$$

where $i = 1,2,3,4.$ and similar to section 4.2.1, the line voltage and current equations for Port 1 at $z = 0$ are

$$v_1(z) = v_e^f(z) + v_e^r(z) + v_o^f(z) + v_o^r(z) \tag{4.3.4}$$

$$v_2(z) = v_e^f(z) + v_e^r(z) - v_o^f(z) - v_o^r(z) \tag{4.3.5}$$

$$i_1(z) = \frac{1}{Z_0}\left[v_e^f(z) - v_e^r(z) + v_o^f(z) - v_o^r(z)\right] \tag{4.3.6}$$

$$i_2(z) = \frac{1}{Z_0}\left[v_e^f(z) - v_e^r(z) - v_o^f(z) + v_o^r(z)\right] \tag{4.3.7}$$

The incident and reflected waves of terminals 1 and 2, at Port 1, can therefore be expressed as

$$\begin{aligned} a_1|_{z=0} &= \frac{1}{2\sqrt{\Re(Z_0)}}\left[v_1 + i_1 Z_0\right] \\ &= \frac{1}{2\sqrt{\Re(Z_0)}}\left[2\left(v_e^f(z) + v_o^f(z)\right)\right] \end{aligned} \tag{4.3.8}$$

$$\begin{aligned} b_1|_{z=0} &= \frac{1}{2\sqrt{\Re(Z_0)}}\left[v_1 - i_1 Z_0^*\right] \\ &= \frac{1}{2\sqrt{\Re(Z_0)}}\left[2\left(v_e^r(z) + v_o^r(z)\right)\right] \end{aligned} \tag{4.3.9}$$

$$\begin{aligned} a_2|_{z=0} &= \frac{1}{2\sqrt{\Re(Z_0)}}\left[v_2 + i_2 Z_0\right] \\ &= \frac{1}{2\sqrt{\Re(Z_0)}}\left[2\left(v_e^f(z) - v_o^f(z)\right)\right] \end{aligned} \tag{4.3.10}$$

$$\begin{aligned} b_2|_{z=0} &= \frac{1}{2\sqrt{\Re(Z_0)}}\left[v_2 - i_2 Z_0^*\right] \\ &= \frac{1}{2\sqrt{\Re(Z_0)}}\left[2\left(v_e^r(z) - v_o^r(z)\right)\right] \end{aligned} \tag{4.3.11}$$

Furthermore, the differential and common-mode voltages and currents at Port 1 are:

$$v_{dm}(z) = 2\left[v_o^f(z) + v_o^r(z)\right] \tag{4.3.12}$$

$$i_{dm}(z) = \frac{1}{Z_0}\left[v_o^f(z) - v_o^r(z)\right] \tag{4.3.13}$$

$$v_{cm}(z) = \left[v_e^f(z) + v_e^r(z)\right] \tag{4.3.14}$$

$$i_{cm}(z) = \frac{2}{Z_0}\left[v_e^f(z) - v_e^r(z)\right] \tag{4.3.15}$$

Substituting these values into the equations for the differential- and common-mode power waves, yields the expressions for the differential- and common-mode incident and reflected power waves at Port 1, in terms of the propagating waves at terminals 1 and 2. Hence, the incident and reflected differential waves at Port 1, given by equation 4.2.34 and 4.2.35, equals

$$a_{dm_1}|_{z=0} = \frac{1}{2\sqrt{Z_{dm}}}\left[v_o^f(z)\left(2 + \frac{Z_{dm}}{Z_0}\right) + v_o^r(z)\left(2 - \frac{Z_{dm}}{Z_0}\right)\right]|_{z=0} \tag{4.3.16}$$

$$b_{dm_1}|_{z=0} = \frac{1}{2\sqrt{Z_{dm}}}\left[v_o^r(z)\left(2 + \frac{Z_{dm}^*}{Z_0}\right) + v_o^f(z)\left(2 - \frac{Z_{dm}^*}{Z_0}\right)\right]|_{z=0} \tag{4.3.17}$$

It then follows from equation 4.3.17 that the characteristic port impedance has to be real, such that the forward propagating voltage equals zero when considering reflected waves. Therefore, given that,

$$Z_0 = R_0 \tag{4.3.18}$$

$$Z_{dm} = 2R_0 \tag{4.3.19}$$

$$Z_{cm} = \frac{R_0}{2} \tag{4.3.20}$$

equations 4.3.16 and 4.3.17 reduce to

$$\begin{aligned} a_{dm_1} &= \frac{1}{2\sqrt{2R_0}}\left(4v_o^f\right) \\ &= \frac{1}{\sqrt{2}}\left(a_1 - a_2\right) \end{aligned} \tag{4.3.21}$$

$$\begin{aligned} b_{dm_1} &= \frac{1}{2\sqrt{2R_0}}\left(4v_o^r\right) \\ &= \frac{1}{\sqrt{2}}\left(b_1 - b_2\right) \end{aligned} \tag{4.3.22}$$

Also, since $Z_{cm} = \frac{R_0}{2}$, the incident and reflected common-mode power wave at Port 1, given by equations 4.2.36 and 4.2.37 reduce to

$$\begin{aligned} a_{cm_1}|_{z=0} &= \frac{1}{\sqrt{2R_0}}\left[2\left(v_e^f(z)\right)\right]|_{z=0} \\ &= \frac{1}{\sqrt{2}}\left[a_1 + a_2\right] \end{aligned} \tag{4.3.23}$$

$$\begin{aligned} b_{cm_1}|_{z=0} &= \frac{1}{\sqrt{2R_0}}\left[2\left(v_e^r(z)\right)\right]|_{z=0} \\ &= \frac{1}{\sqrt{2}}\left[b_1 + b_2\right] \end{aligned} \tag{4.3.24}$$

The above equations clearly indicate that the differential- and common-mode incident waves are defined by the forward propagating odd and even mode waves, while the reflected waves are defined by the reverse directed odd and even mode propagation, respectively. Repeating the above procedure at $z = l$ the mixed-mode power waves at Port 2, comprising of terminals 3 and 4, are shown to be

$$a_{dm_2} = \frac{1}{\sqrt{2}}\left[a_3 - a_4\right] \tag{4.3.25}$$

$$b_{dm_2} = \frac{1}{\sqrt{2}}\left[b_3 - b_4\right] \tag{4.3.26}$$

$$a_{cm_2} = \frac{1}{\sqrt{2}}\left[a_3 + a_4\right] \tag{4.3.27}$$

$$b_{cm_2} = \frac{1}{\sqrt{2}}\left[b_3 + b_4\right] \tag{4.3.28}$$

It then follows from equations 4.3.22, 4.3.26, 4.3.24, and 4.3.28 that the reflected mixed-mode waves at each port can be related to the reflected waves at each terminal:

$$\left[\mathbf{b}_{mm}\right] = \left[\mathbf{M}\right]\left[\mathbf{b}\right] \tag{4.3.29}$$

where,

$$[\mathbf{M}] = \frac{1}{\sqrt{2}} \begin{bmatrix} 1 & -1 & 0 & 0 \\ 0 & 0 & 1 & -1 \\ 1 & 1 & 0 & 0 \\ 0 & 0 & 1 & 1 \end{bmatrix} \tag{4.3.30}$$

is the transformation matrix and $[\mathbf{b}] = \begin{bmatrix} b_1, & b_2, & b_3, & b_4 \end{bmatrix}^T$ is the reflected waves at the four terminals as defined in equation 4.1.16.

Similarly it can be shown that

$$[\mathbf{a}_{mm}] = [\mathbf{M}]\,[\mathbf{a}] \tag{4.3.31}$$

where $[\mathbf{a}] = \begin{bmatrix} a_1, & a_2, & a_3, & a_4 \end{bmatrix}^T$ is the vector containing the incident waves at each of the four terminals. Thus, from equations 4.1.16, 4.3.29, and 4.3.31 we can relate the standard four terminal scattering matrix $[S]$ and the mixed-mode scattering matrix $[S_{mm}]$ by

$$[\mathbf{S}_{mm}] = [\mathbf{M}]\,[\mathbf{S}]\,[\mathbf{M}]^{-1} \tag{4.3.32}$$

$$[\mathbf{S}] = [\mathbf{M}]^{-1}\,[\mathbf{S}_{mm}]\,[\mathbf{M}] \tag{4.3.33}$$

4.4 Conclusion

This chapter introduced a method of obtaining the mixed-mode S-parameters of a differential network from a standard S-parameters measurement. This makes it possible to determine the differential and common-mode gain as well as the common-mode rejection ratio of a differential network using the general S-parameters of the network. Furthermore, the techniques for deriving the mixed-mode parameters can be applied to mixed-mode noise analysis, as done in section 6.2.6, wherein a transformation matrix analogous to that of equation 4.3.30 is derived in order to calculate the differential noise parameters of a differential network.

Chapter 5

Noise Figure Measurement

Experimental characterisation of low-noise devices is of high importance in the design cycle. This chapter introduces methods developed for determining the noise figure as well as the noise parameters of linear two-port devices. These methods are then applied to various measurement techniques proposed for de-embedding the differential noise figure of three- and four-port differential devices.

5.1 Linear Two-port Devices

Measuring the noise of a two-port device requires the fundamental property of noise linearity. As the graph in figure 5.1 indicates, the output noise power of a Device Under Test (DUT) should be related to the input noise power, or temperature, by the factor

$$kG_a\Delta f \tag{5.1.1}$$

where k is Boltzmann's constant, and G_a is the gain of the DUT. The graph also indicates that, in principle, the equivalent outpu noise power (N_a) of the DUT can be determined by connecting the input of the DUT to a load kept at absolute zero ($0K$). However, as measurements at absolute zero are impossible, the output noise power is measured at different source temperatures to obtain the noise slope, from which the equivalent noise power can easily be calculated.

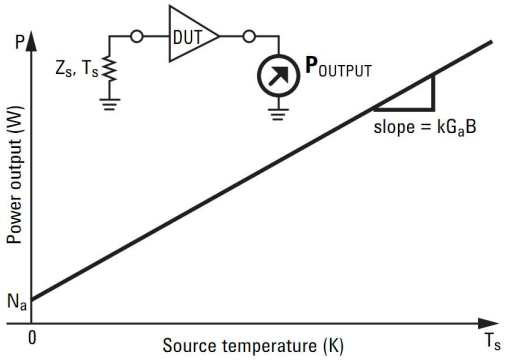

Figure 5.1: Graphical representation of the linear relationship between input noise temperature and output noise power, from [2].

Given that the output noise power of the DUT is linearly related to the input noise power, the noise factor expressed in terms of the output noise power, as in equation 2.3.8, can be written in terms of the equivalent noise power of the DUT as

$$N_a = G_a (N_e + N_i) \tag{5.1.2}$$

The noise factor can be computed from the equivalent noise temperature, by substituting equation 5.1.2 into equation 2.3.8,

$$F = 1 + \frac{N_e}{N_i} \tag{5.1.3}$$

Furthermore, recalling that noise power is related to temperature as in equation 2.3.6 the noise factor can be expressed in terms of the DUT equivalent noise temperature T_e and the standard temperature T_0

$$F = 1 + \frac{T_e}{T_0} \tag{5.1.4}$$

The equivalent input noise temperature, and therefore the noise figure of the DUT can be determined by measuring the output noise power at two different source temperatures. This measurement technique is referred to as the *Y-factor* method and forms the basis for the operation of most Noise Figure Meters and Noise Figure Analysers (NFAs).

5.1.1 Y-factor Measurement

A schematic representation of the Y-factor measurement setup is shown in figure 5.2.

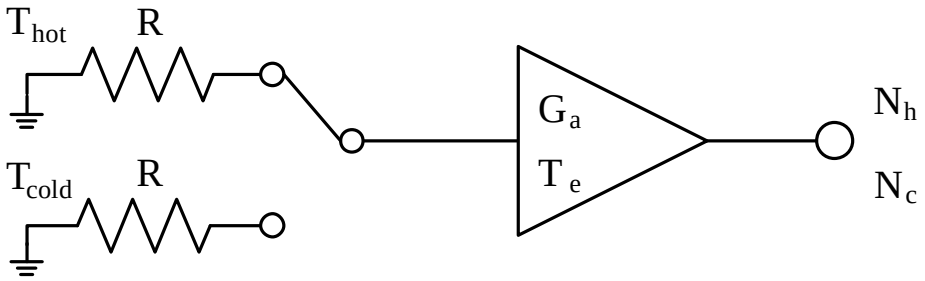

Figure 5.2: Schematic representation of the Y-factor measurement setup.

The method involves measuring the output noise power of the device for two loads connected to the device input, that are kept at two significantly different temperatures, denoted by T_h and T_c, where h and c correspond to the terms 'hot' and 'cold'. The respective output noise power produced for each of the different source temperatures are given by

$$N_h = G_a k T_h \Delta f + G_a k T_e \Delta f \tag{5.1.5}$$

$$N_c = G_a k T_c \Delta f + G_a k T_e \Delta f \tag{5.1.6}$$

Using the output noise powers, the *Y-factor* is defined as

$$Y = \frac{N_h}{N_c} = \frac{T_h + T_e}{T_c + T_e} > 1 \tag{5.1.7}$$

from which the equivalent noise temperature of the DUT can be solved as

$$T_e = \frac{T_h - YT_c}{Y - 1} \tag{5.1.8}$$

Considering equations 5.1.7 and 5.1.8, it is clear that the temperature difference of the two noise sources should be large enough to avoid unnecessary loss of accuracy [15]. Therefore, when performing the Y-factor measurements manually, one load is usually kept at room temperature ($T_h = T_0 = 290K$), while the other is immersed in either liquid Nitrogen ($T_c = 77K$) or Helium ($T_c = 4K$). Since manual Y-factor measurement requires an accurate temperature controlled environment to ensure repeatable results, noise figure measurement is mostly performed using modern Noise Figure Meters or NFAs that use electronic noise sources. One of the noise sources generally used in noise figure measurements is a low-capacitance diode that generates noise levels equivalent to several thousand Kelvin when reverse biased into avalanche breakdown, referred to as the noise source's 'ON' state [2]. In its 'OFF' state the noise source produces a noise temperature equal to the ambient temperature. The output noise level of a noise source is represented by its ENR which is expressed, in dB, as

$$ENR_{dB} = 10log\left(\frac{T_h - T_c}{T_0}\right) \tag{5.1.9}$$

Noise sources are each supplied with their unique dataset containing the calibrated ENR values over a frequency range. Note that the calibration of a noise source is performed in a controlled environment to ensure $T_c = T_0 = 290K$ and it is therefore necessary to compensate for any deviation of T_c from T_0 during measurements. This procedure can be avoided by performing measurements using a noise source similar to Agilent's *SNS*-Series that incorporates a temperature sensor and transmits the value of T_c to the NFA before each measurement sweep, thereby increasing the accuracy of the measured data. Further techniques of improving measurement accuracy are discussed in the following section.

5.1.2 Measurement Accuracy Improvement

Performing noise measurement with a NFA involves a two step procedure: a calibration of the measurement system and the actual noise figure measurement of the DUT. During both the calibration and the measurement procedure, the NFA performs noise analysis based on the Y-factor method introduced in section 5.1.1. The NFA computes the gain (G_{NFA}) and noise figure (F_{NFA}) of the measurement system during the calibration procedure, and stores the 'hot' and 'cold' output noise powers N_c^{ON} and N_c^{OFF}. Repeating the procedure with the DUT in place, the NFA measures the system output noise powers N_s^{ON} and N_s^{OFF} and computes the gain of the DUT as the ratio

$$G_{DUT} = \frac{N_s^{ON} - N_s^{OFF}}{N_c^{ON} - N_c^{OFF}} \tag{5.1.10}$$

and the system noise figure F_{sys} using the Y-factor method.

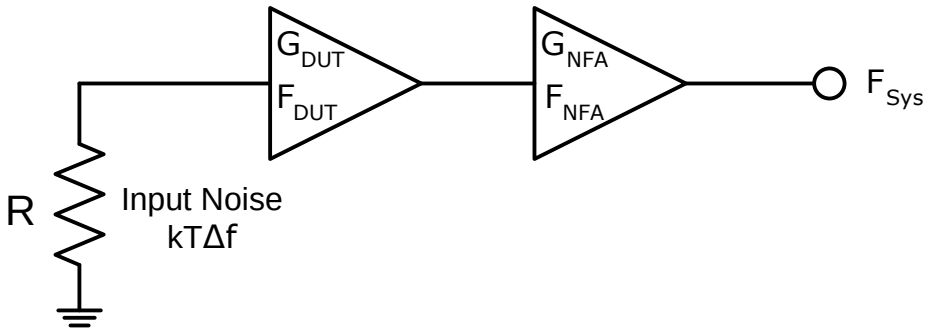

Figure 5.3: Schematic representation of the noise figure measurement system.

Figure 5.3 illustrates the cascaded measurement system. Applying the theory developed by Friis [32], the cascaded system noise factor can be expressed in terms of the DUT and NFA noise factors as

$$F_{sys} = F_{DUT} + \frac{F_{NFA} - 1}{G_{DUT}} \tag{5.1.11}$$

The NFA uses the relationship of equation 5.1.11 to de-embed the noise figure of the DUT. Note that the gain of the DUT is the measured transducer gain and not the available gain as in the definition of Friis. The measured DUT gain is therefore dependent on the mismatch between the noise source and the DUT as well as the input impedance of the NFA. Figure 5.4 contains a graph indicating the variation in input SWR of the Agilent N8975A NFA over frequency.

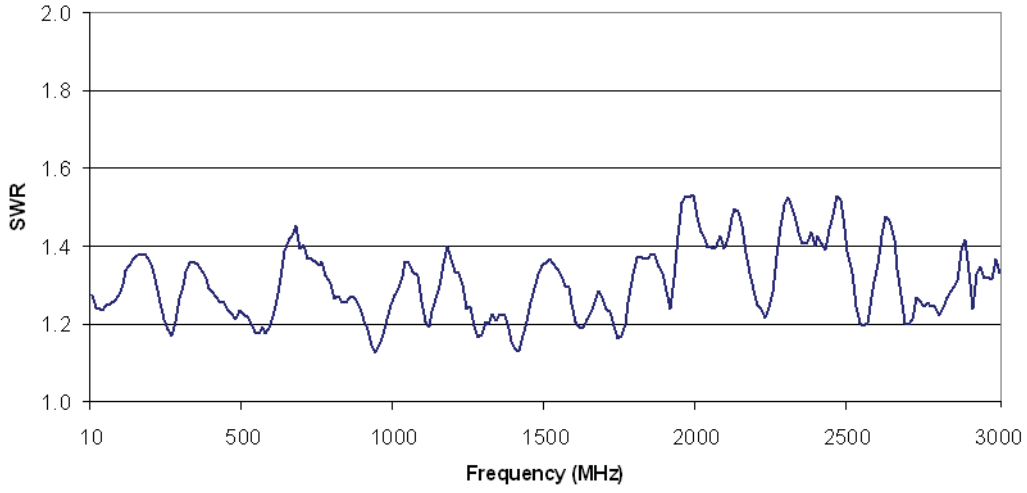

Figure 5.4: Input Standing Wave Ratio of the Agilent N8975A NFA with frequency.

This variation in measurements over frequency can be minimized by inserting circulators (or attenuators) before and after the DUT. Placing circulators/attenuators between the DUT and the NFA minimises the effect of reflections and ensures that the output impedance of the DUT does not influence the noise figure of the NFA and conversely, that the input impedance of the NFA does not influence the gain of the DUT. On the other hand, circulators/attenuators placed between the noise source and the DUT ensures that the LNA is well matched, thereby minimising variations in noise figure, and prevents the output power of the noise source to be influenced

by the input of the DUT. It is important to note that only the circulator/attenuator placed between the DUT and the NFA is included in the calibration procedure. The circulator/attenuator placed between the noise source and the DUT is only inserted with the DUT. This will of course reduce the DUT gain and also increase the measured noise figure by the associated loss of the circulator/attenuator. Furthermore when measuring low noise devices the noise contributed by the NFA can influence the accuracy of the measured DUT noise figure and it is therefore recommended to include a pre-amplifier before the NFA in order to decrease the noise contributed by the measurement instrument. The following section investigates the influence different accuracy improvement techniques have on noise figure measurements.

5.1.3 Investigating Accuracy Improvement

There are a number of different techniques that can be implemented in order to improve noise figure measurement accuracy when using a NFA with an electronic noise source. This section compares the deviation in measurements observed when implementing each of the various techniques by considering the measured noise figure of the paired single ended LNA design discussed in Chapter 6. The three measurement configurations proposed for improving accuracy are illustrated in figure 5.5.

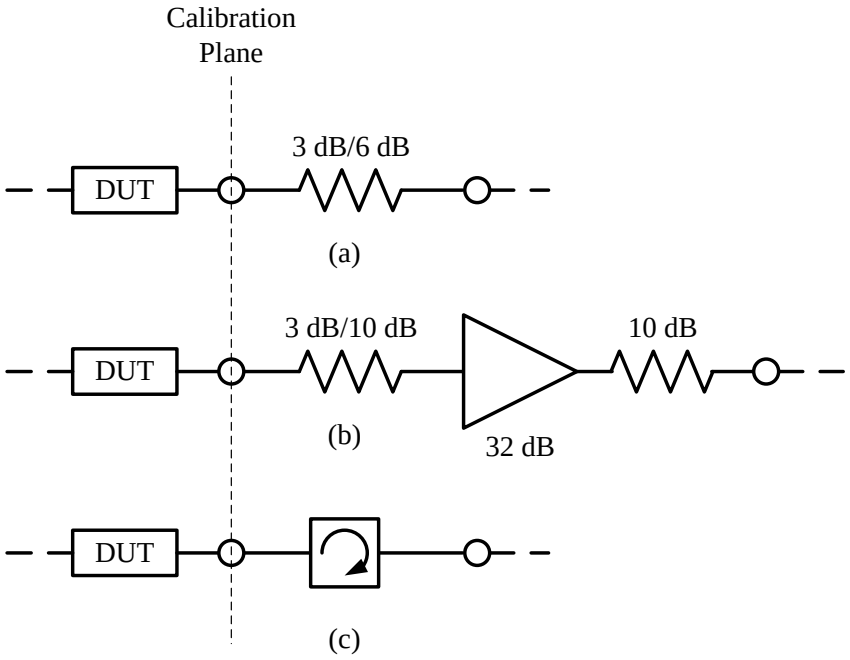

Figure 5.5: Measurement calibration configurations implementing, (a) Attenuators, (b) Attenuators connected to a pre-amplifier with a 10dB attenuator at the output, (c) Circulator.

These include an attenuator pad (figure 5.5(a)), a pre-amplifier with attenuator pads connected to the input and output of the pre-amplifier to ensure a stable response (figure 5.5(b)), and a circulator placed between the DUT and the NFA (figure 5.5(c)), respectively. First consider the noise figure measured after calibration - that is without the DUT - for the measurement configuration in figure 5.5(a). Note that, ideally, the measured noise figure should be 0 dB exactly across the band.

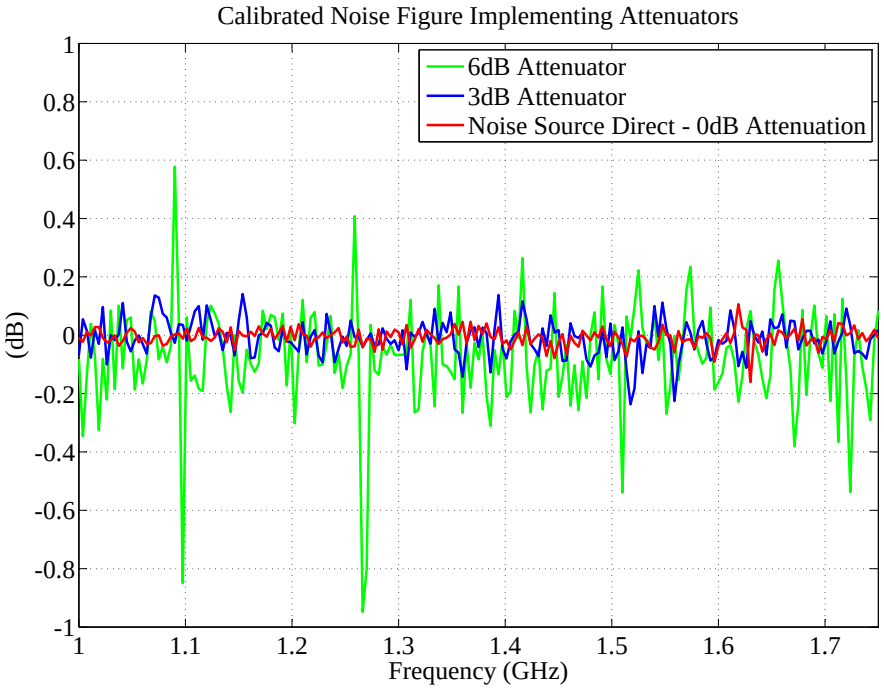

Figure 5.6: Calibrated noise figures of 3dB and 6dB attenuator compared to noise source only.

It is clear from figure 5.6 that the uncertainty in measurement increases as the gain of the measurement chain decreases. As explained by equation 5.1.11, the system noise can be reduced by a increasing the gain. This is illustrated by the noise figure measured, after calibration, for the circuit in figure 5.5(b) with a 3dB and a 10dB attenuator connected to the input of the 32 dB pre-amplifier, respectively.

The graph in figure 5.7 shows the measured noise figure, without the DUT, after calibration and indicates that the added gain introduced by the pre-amplifier significantly reduces the measurement uncertainty when considering the magnitude of the jitter observed in the measurement made with the 3dB attenuator at the input of the pre-amplifier. Comparing the average level of the calibrated noise figure for the two configurations shows the amount of error introduced due to the non-linearity of the NFA at high input power levels. This error can be corrected by setting the internal attenuator of the NFA to a larger value, as done for the same calibrated noise figure, with the internal attenuator set to 15dB, shown in figure 5.8. Note that in both figures 5.7 and 5.8 the calibration performed with the 10dB attenuator at the input of the pre-amplifier still indicate a significant amount of uncertainty.

Next consider the noise figure of the DUT measured for each of the calibrated circuits outlined above - with the noise source connected directly to the input of the DUT - shown in figure 5.9.

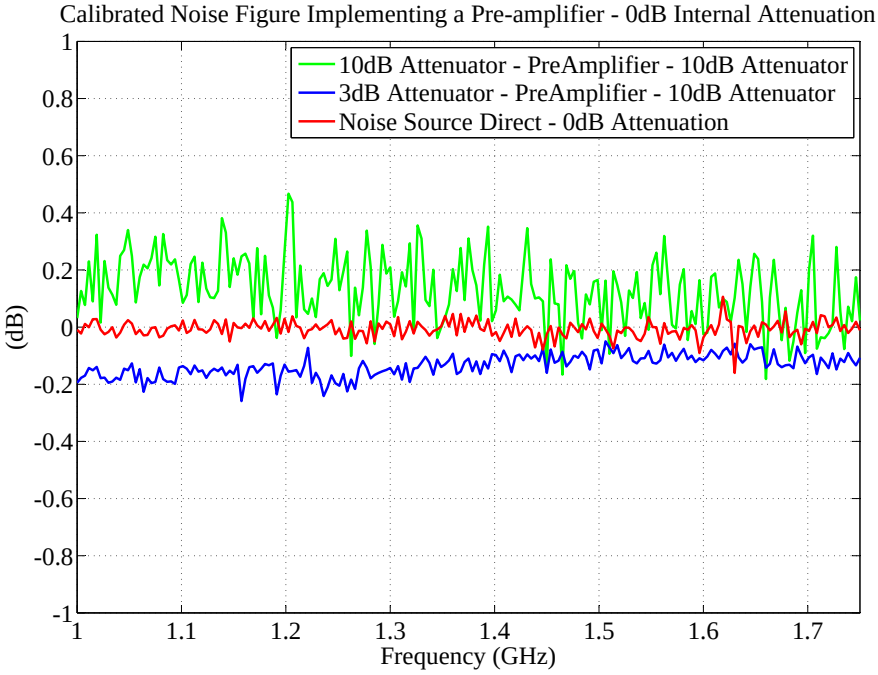

Figure 5.7: Calibrated noise figures of 3dB and 10dB attenuators cascaded with a pre-amplifier - no internal attenuation.

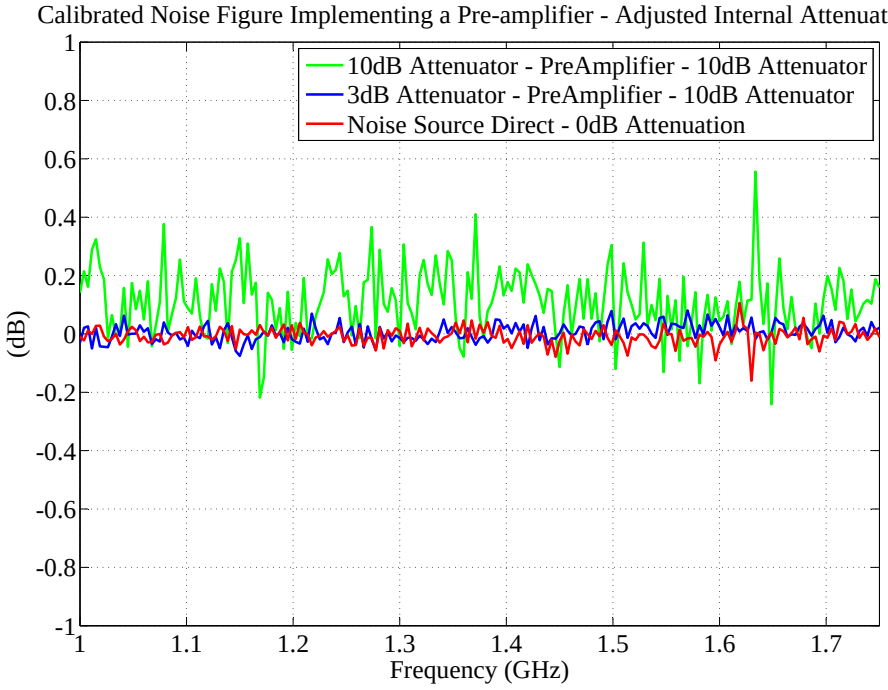

Figure 5.8: Calibrated noise figures of 3dB and 10dB attenuators cascaded with a pre-amplifier - internal attenuation adjusted.

The severity of the loading effect of the DUT on the power produced by the noise source is clear from the 0 dB noise figure measured in figure 5.9. This can only occur if the noise source generates less noise power when loaded by the DUT than during calibration. To reduce the loading effect/mismatch, the measurement is repeated with a 3dB attenuator placed between the DUT and the noise source. The insertion loss of the 3dB

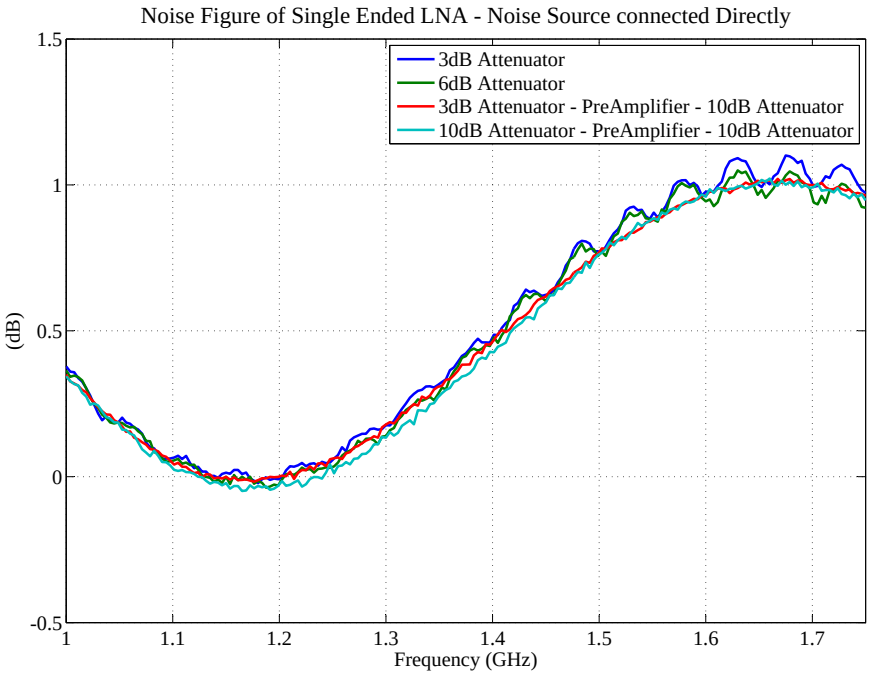

Figure 5.9: LNA noise figure measured with noise source connected directly to DUT.

attenuator is measured and subtracted from the measured noise figure in order to de-embed the noise figure for each the calibration configurations. The de-embedded noise figures are compared in figure 5.10.

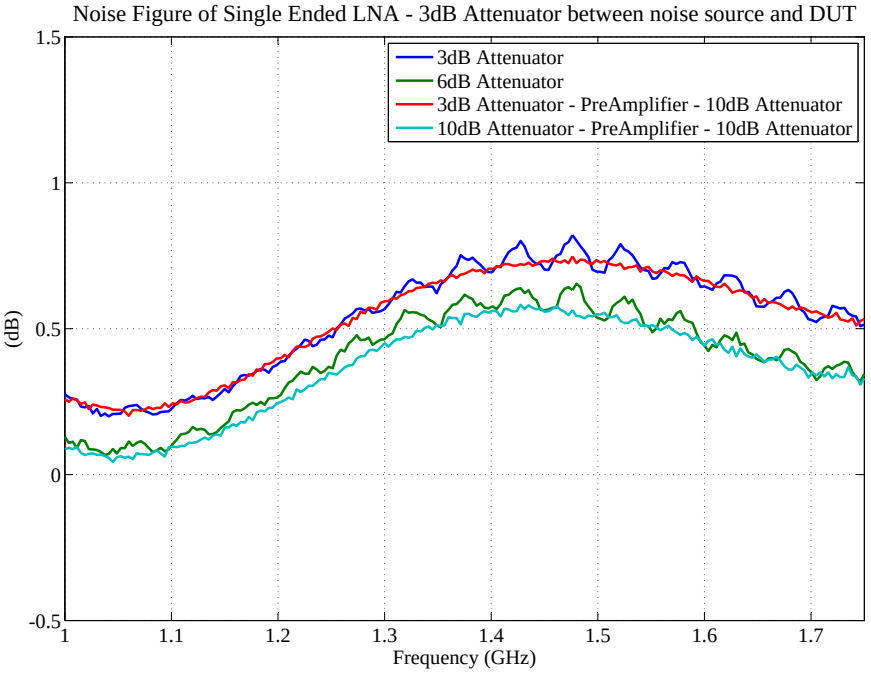

Figure 5.10: LNA noise figure measured with a 3dB attenuator connected between the noise source and the DUT.

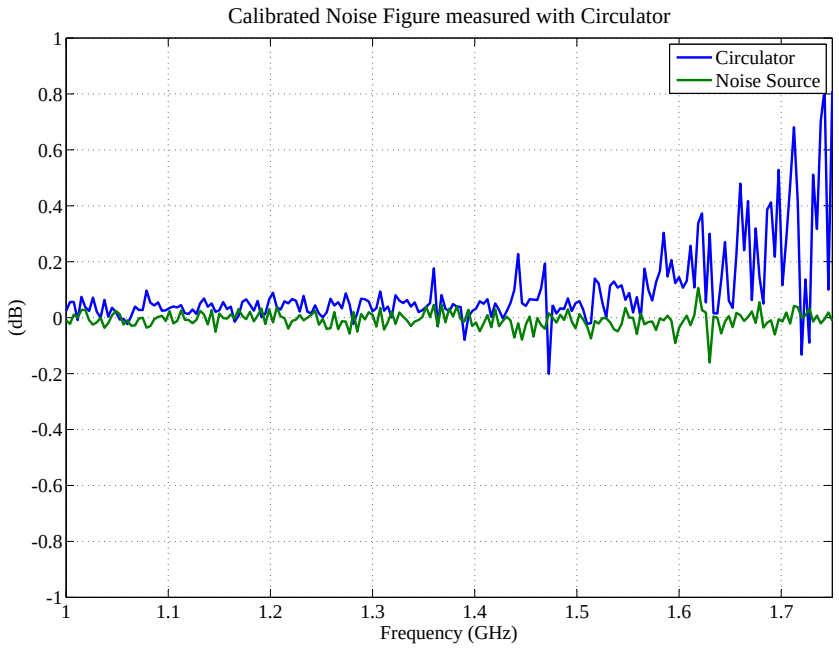

Figure 5.11: Calibrated noise figure with circulator compared to noise source only.

The graph in figure 5.10 shows the effect the large jitter observed in the calibrated noise figure of the calibrations performed with the 6dB and 10dB attenuators when considering the deviation from the noise figure measured with the 3dB attenuators. Still the noise figure measured with the 3dB attenuators at the output does not conform to the simulated noise figure illustrated in figure 6.48. From the discussion outlined in this section it can be deduced that, in order to perform accurate measurements using a high ENR (15dB) noise source the DUT has to be well matched to both the noise source and the NFA, using a component with a low insertion loss. This can be seen when considering the noise figure of the circuit in figure 5.5(c), measured after calibration - without the DUT, shown in the graph in figure 5.11. The measured insertion loss and reflection coefficients of the circulators are shown in figure 5.12, indicating that the operating band of the circulator used for the calibration depicted in figure 5.11 is approximately 1.2-1.4 GHz.

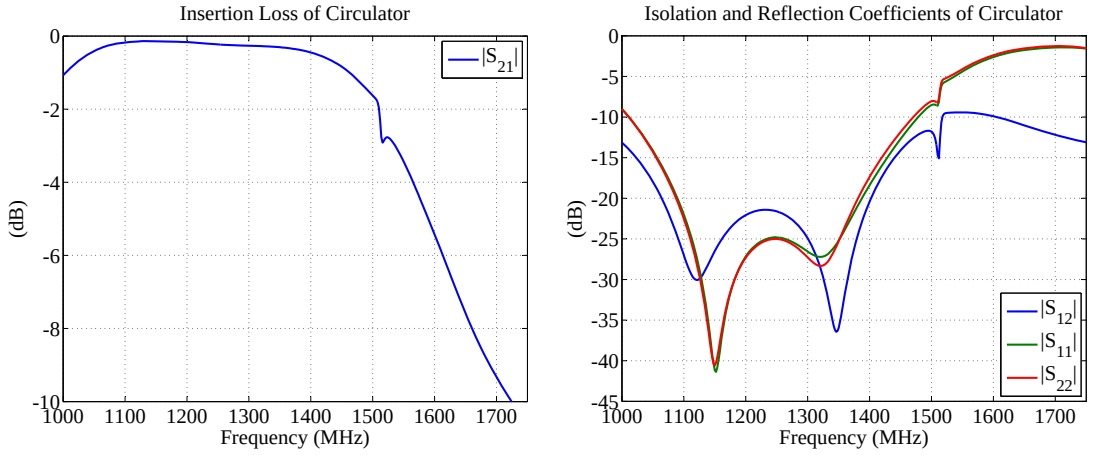

(a) (b)

Figure 5.12: Measured (a) insertion loss and (b) reflection coefficients of the circulator used during calibration.

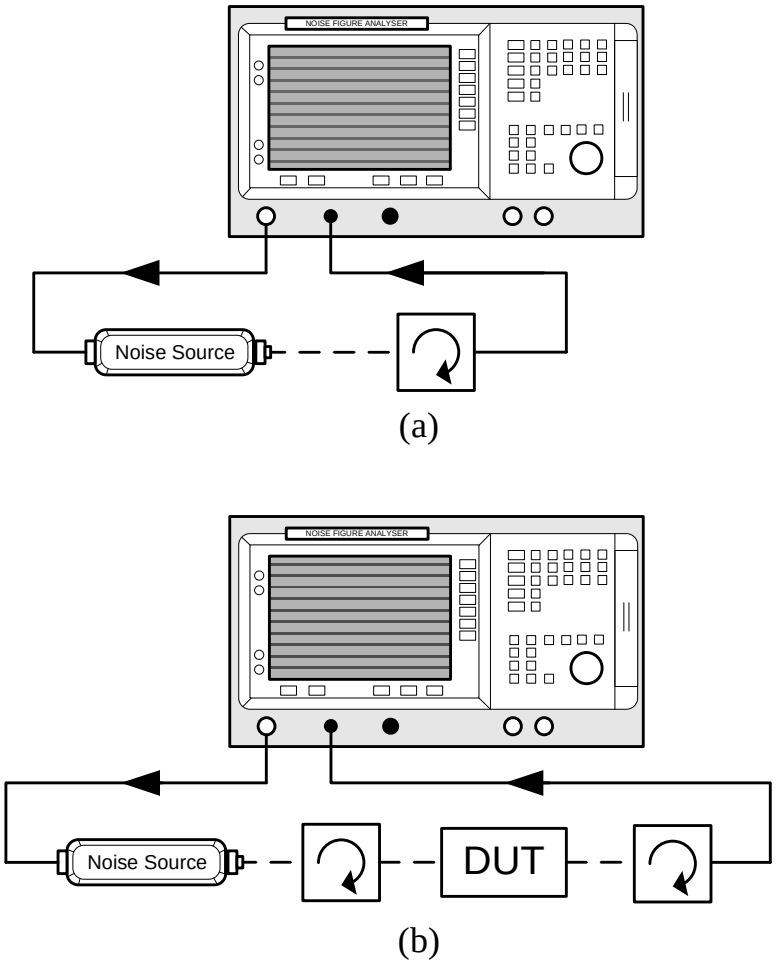

Figure 5.13: Schematic representation of the noise figure (a) calibration setup and (b) measurement setup.

Comparing the calibrated noise figure of the circulator to the calibration performed with only the noise source verifies that a low insertion loss provides the most accurate calibration. Including another circulator between the noise source and the DUT therefore ensures a good power match without introducing an unnecessary amount of loss. The noise figure of the LNA measured, within the operating band of the circulators, using the calibration and measurement setup indicated in figure 5.13, is compared to the simulated noise figure in the graph shown in figure 5.14.

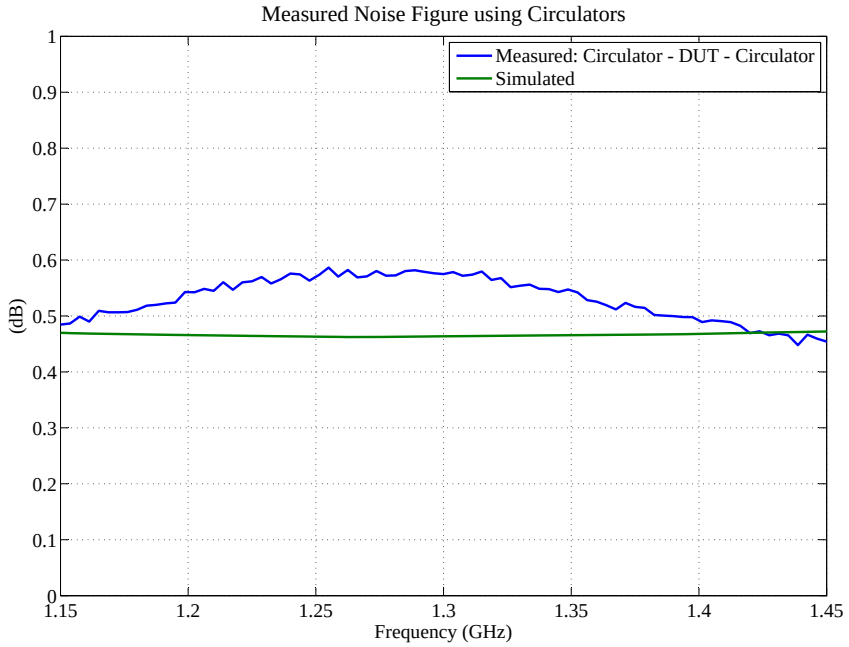

Figure 5.14: Noise figure measured using circulators compared to simulated noise figure.

5.1.4 Alternative Measurement Techniques

Section 2.3 introduced the two-port noise parameters that can be used to determine the noise performance of a device terminated in an arbitrary source impedance Y_s. That is, if the four noise parameters F_{min}, R_n, and Y_{opt} of a device are known, the noise factor of the device for any port termination can be solved using

$$F = F_{min} + \frac{R_n}{\Re(Y_s)}\left[Y_s - Y_{opt}\right]^2 \tag{5.1.12}$$

Conversely the four noise parameters can be solved by measuring the noise factor of a device at four different source impedances. Measuring the noise figure can be done using the Y-factor method introduced in section 5.1.1. However, the change in impedance that occurs when the noise source switches between the 'hot' and 'cold' states can cause deviations in measurements. Davidson *et al.* proposed a new measurement technique that aims to eliminate the deviation caused by the change in source impedance by performing a number of noise power measurements with the noise source kept in the 'cold' state, and only performing a single noise power measurement with the noise source in its 'hot' state in order to find a scaling factor for the extracted minimum noise figure [46]. This measurement technique is referred to as the 'Cold source' method.

5.1.4.1 'Cold-source' Measurement

The measurement system for the cold source method , shown in figure 5.15, comprises of a noise source and impedance tuner that can alternately be connected to the input of the DUT, as well as a preamplifier connected to a noise power meter which are in turn connected to the output of the DUT. Furthermore the system includes a Vector Network Analyser (VNA) used to measure the Scattering (S)-parameters at each frequency interval as well as the impedances presented to the DUT by the impedance tuner, the noise source and the output network.

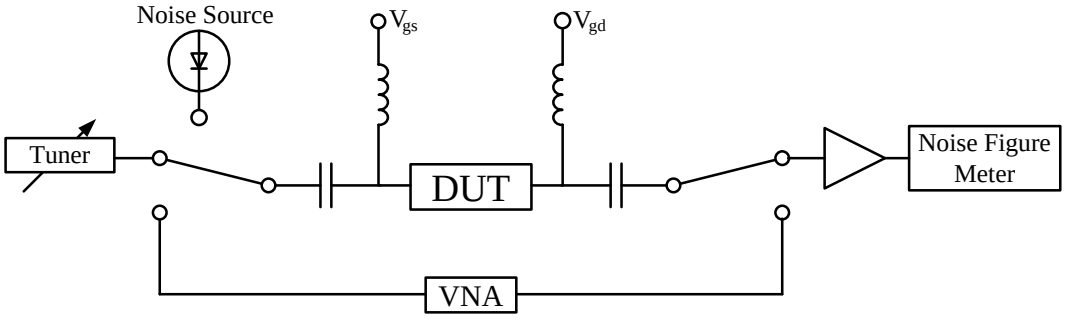

Figure 5.15: Cold source measurement system.

Similar to the Y-factor method, the system is calibrated with the noise source in its 'hot' state by substituting the DUT with a through connection and thereby calculating the noise contributed by the measurement system. After calibration, the noise parameters of the DUT is extracted by performing a single measurement with the noise source in its 'hot' state and at least four measurements with the DUT connected to the impedance tuner, where the tuner is set to a different impedance for each measurement. The study performed in [46] indicates that accuracy of the extracted noise parameters are not dependent on the number of impedances presented to the DUT but rather on their distribution. Concluding that if the impedances are well distributed, as the impedance constellation in figure 5.16 shows, accurate measurements can be performed.

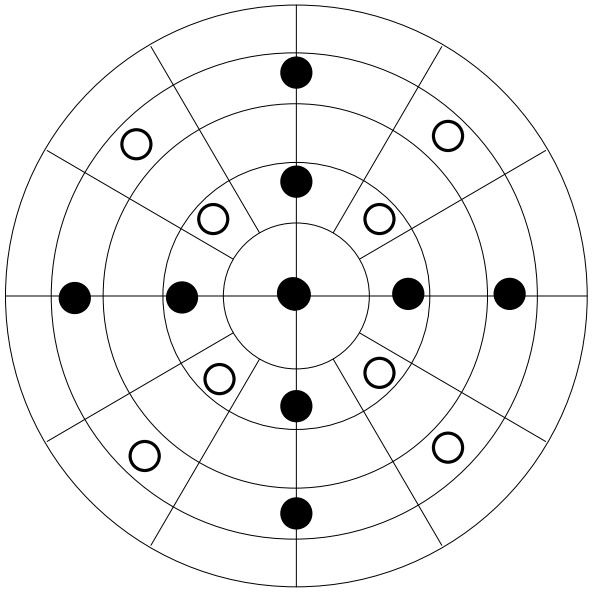

Figure 5.16: Source constellations used in cold source noise measurement.

5.1.4.2 Improved Y-factor Measurement

Tiemeijer *et al.* later showed that the Y-factor measurement method, introduced in section 5.1.1, still proves to be adequate for extracting accurate noise parameters provided some additions are made [3]. This adaptation of the 'classic' Y-factor method, referred to by Tiemeijer *et al.* as the 'Improved Y-factor Method', defines the

ratio of the output noise powers with the noise source in its 'hot' and 'cold' states by

$$Y = \frac{N_H}{N_C} = \frac{(F_{Y_H} - 1)kT_0 G_{T,Y_H}\Delta f + kT_H G_{T,Y_H}\Delta f}{(F_{Y_C} - 1)kT_0 G_{T,Y_C}\Delta f + kT_C G_{T,Y_C}\Delta f} \tag{5.1.13}$$

where G_{T,Y_H} and G_{T,Y_C} are the transducer gains of the DUT for the hot and cold noise source admittances, Y_H and Y_C. This improved Y-factor method incorporates the change in noise source impedance by defining an effective Y-factor

$$Y' = \frac{G_{T,Y_C}}{G_{T,Y_H}} Y \tag{5.1.14}$$

$$= \frac{F_{Y_H} + \frac{T_H - T_0}{T_0}}{F_{Y_C} + \frac{T_C - T_0}{T_0}} \tag{5.1.15}$$

and from this, the effective ENR

$$ENR' = \frac{T_H - T_0}{T_0} + Y' \frac{T_C - T_0}{T_0} \tag{5.1.16}$$

Thereby giving the relation

$$Y' F_{Y_C} - F_{Y_H} = ENR' \tag{5.1.17}$$

By substituting equation 5.1.12 into equation 5.1.17 the Y-factor weighted average of the noise figures measured at Y_C and Y_H can be expressed as

$$F_{Y_C,Y_H,Y'} = \frac{ENR'}{Y' - 1} \tag{5.1.18}$$

$$= F_{min} + R_n \left(\frac{Y'}{Y' - 1} \frac{|Y_C - Y_{opt}|^2}{\Re(Y_C)} - \frac{1}{Y' - 1} \frac{|Y_H - Y_{opt}|^2}{\Re(Y_H)} \right) \tag{5.1.19}$$

Then, similar to the Cold source method discussed in section 5.1.4.1 the noise parameters of the DUT can be solved by determining the noise factor, $F_{Y_C,Y_H,Y'}$, and the effective Y-factor, Y', at at least four different source admittances.

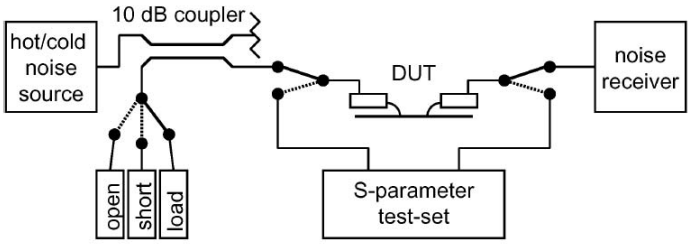

Figure 5.17: Measurement system for improved Y-factor noise measurement, from [3].

As mentioned in [46] the source impedances presented to the DUT should be well distributed in order to decrease measurement uncertainty. To achieve this, the measurement system proposed by Tiemeijer *et al.*, illustrated in figure 5.17, uses a wideband 10dB coupler terminated in either an open, shorted or matched load instead of an impedance tuner. The source impedances represented to the DUT is therefore in the form of one matched and two reflective sources spaced 180° apart. By making the assumption that the noise performance of the DUT is linear over a small bandwidth $(f_0 - \Delta) < f < (f_0 + \Delta)$, nine different source admittances can

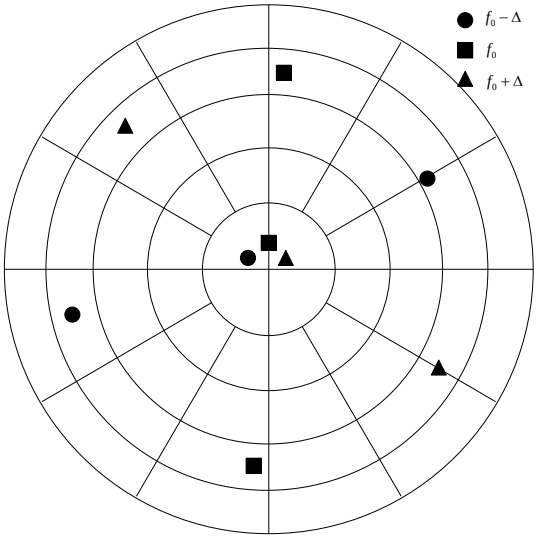

Figure 5.18: Constellation of source reflections in a narrow bandwidth as seen by the DUT

be achieved with this measurement setup. The source constellation realised at three different frequencies in a narrow bandwidth is illustrated in figure 5.18.
Similar to the Cold source measurement system, the system also includes a VNA connected in parallel to the DUT in order to measure the device S-parameters as well as characterise the measurement system. Since the improved Y-factor method considers a noise power ratio instead of absolute noise power as done in the Cold-source method, most drifts and uncertainties in the system gains cancel and therefore only minor correction need to be made using the measured S-parameters.

5.2 Differential Devices

The IRE definition for noise figure that forms the basis of the noise measurement techniques described in section 5.1, apply only to single ended devices. Therefore commercial noise figure meters and noise sources are all single ended, which poses a concern when attempting to characterise the noise of differential devices. This section introduces some of the more recent techniques published on the de-embedding of differential noise figure from single ended measurements. The first of which is the method published by Abidi and Leete in [4].

5.2.1 De-embedding the Differential Noise Figure using Baluns

The de-embedding technique published by Abidi and Leete in 1999 proposes the use of baluns to convert a single ended stimulus of the noise source into a differential stimulus and to combine the differential response into a single ended one that can be analysed by a single ended noise figure meter. That is, by assuming ideal passive baluns, a voltage signal applied to the input (port 1) of the balun is split evenly but out of phase between the output ports (ports 2 and 3) and when two equal anti phase voltages are applied to ports 2 and 3, the voltages are combined at port 1. However, any signal applied to ports 2 and 3 that is in phase is dissipated in an internal load.

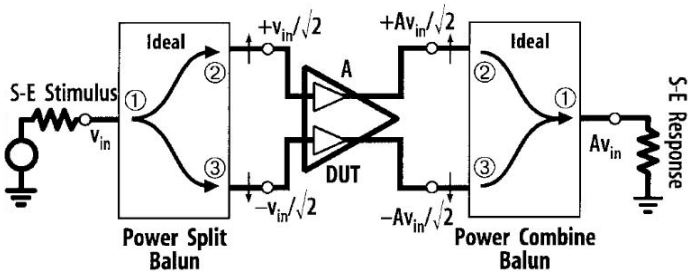

Figure 5.19: Differential amplifier connected to ideal input and output baluns, from [4].

Figure 5.19 shows a differential amplifier connected to two ideal baluns. The differential amplifier considered in this analysis is assumed to have equal gains, G_A, and associated input referred noise powers, N_a, along its two respective signal paths. Given the relation in equation 5.1.3 the associated input referred noise power can be expressed in terms of the device noise factor F_A

$$N_a = (F_A - 1)\,kT_0\Delta f \tag{5.2.1}$$

In a similar fashion, the output noise power at ports 2 and 3 of the power splitting balun can be solved in terms of the noise factor F_1 and gain G_1 of the balun. That is, given that the gain along the two paths are identical

$$N_{o1} = F_1 kT_0 G_1 \Delta f \tag{5.2.2}$$

Consider the noise contributed by the power combining balun. The output noise power measured at port 1 is equal to the sum of the noise generated at the input ports and the noise contributed by the balun N_B. Given that the input noise power equals $kT_0\Delta f$, the output noise power can be expressed as

$$N_{o2} = N_B + 2kT_0 G_2 \Delta f \tag{5.2.3}$$

from which the noise generated by the balun can be solved in terms of the balun noise factor F_2 given the relation in equation 5.2.2. That is,

$$N_B = (F_2 - 2)\,kT_0 G_2 \Delta f \tag{5.2.4}$$

The total single ended output noise power received is therefore equal to

$$N_{o_{SE}} = 2\,(N_{o1} G_A G_2 + N_a G_A G_2) + N_B \tag{5.2.5}$$

$$= 2F_1 kT_0 G_1 G_A G_2 \Delta f + 2\,(F_A - 1)\,kT_0 G_A G_2 \Delta f + (F_2 - 1)\,kT_0 G_2 \Delta f \tag{5.2.6}$$

In order to express the equivalent measured single ended noise figure of the system shown in figure 5.19 an expression for the portion of the output noise generated by the source needs to be derived. Since the only source of noise in the entire system is the single ended stimulus at the input, the noise voltages due to the source at ports 2 and 3 of the combining balun are completely correlated. Therefore the output noise voltage due to these correlated noise voltages can be solved from

$$\overline{e_o}^2 = \overline{e_2}^2 + \overline{e_3}^2 + 2\overline{e_2 e_3^*}C \tag{5.2.7}$$

where the term C defines the correlation between the noise voltages at ports 2 and 3, e_2 and e_3. Given that $e_2 = e_3$ and $C = 1$, since both noise voltages at port 2 and 3 originate from the same source, the output noise power due to the source alone is solved as

$$N_{o_i} = 4kT_0 G_1 G_a G_2 \Delta f \tag{5.2.8}$$

It also follows from equation 5.2.8 that the system gain equals

$$G_{sys} = 4G_1G_AG_2 \tag{5.2.9}$$

or in decibels,

$$G_{sys}(dB) = G_1(dB) + G_A(dB) + G_2(dB) + 6dB \tag{5.2.10}$$

The noise figure of the cascaded system can then be expressed as

$$F_{sys} = \frac{N_{o_{SE}}}{N_{o_i}} \tag{5.2.11}$$

$$= \frac{1}{2}F_1 + \frac{1}{2}\left(\frac{F_A - 1}{G_1}\right) + \frac{1}{4}\left(\frac{F_2 - 2}{G_1G_A}\right) \tag{5.2.12}$$

Using equations 5.2.12 and 5.2.9 the noise factor and gain of the differential amplifier can be de-embedded by performing three single ended Y-factor noise figure measurements to determine noise factors F_1, F_2, and F_{sys} as well as gains G_1, G_2, and G_{sys}. To measure the noise factors and gains of the power splitting and combining baluns, the measurement setup illustrated in figure 5.20 is used.

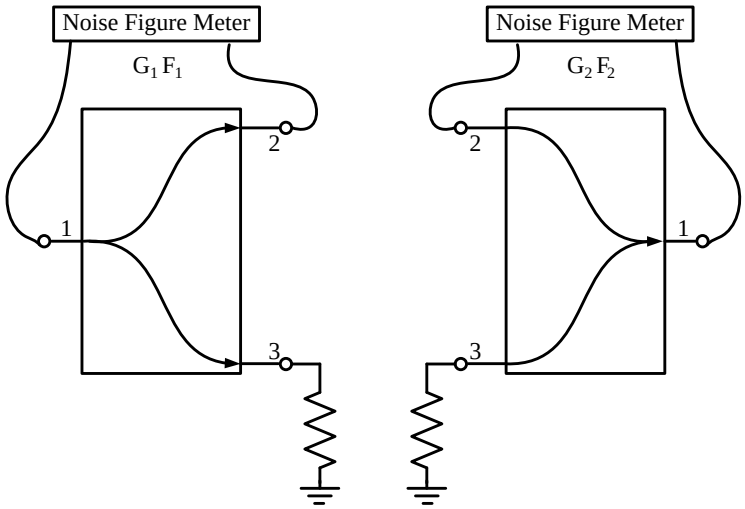

Figure 5.20: Single ended measurement of the (a) power-splitting and (b) power-combining baluns.

By assuming ideal operation, the balun noise figure and gain can be measured by terminating the open port in a matched load. Furthermore, it can be shown that for any matched passive two-port network the noise factor equals the reciprocal of the insertion loss of the network. Thus, for an ideal balun, the single ended insertion loss $G = 1/2$ and therefore the noise factor $F = 1/G = 2$. It then follows from equation 5.2.12 that, for $F_1 = F_2 = 2$ and $G_1 = G_2 = 1/2$,

$$F_{sys} = F_A \tag{5.2.13}$$

and similarly

$$G_{sys} = G_A \tag{5.2.14}$$

thereby validating the use of equation 5.2.12 for the de-embedding of the noise figure of a differential amplifier using baluns.

5.2.2 Deriving the Mixed-Mode Noise Correlation Matrix from Noise Figure Measurements

The noise analysis published by Abidi and Leete, described in section 5.2.1, assumes no correlation between the equivalent output noise sources of the differential amplifier and also only defines the differential noise performance of the DUT within the measurement system. A similar measurement system, incorporating baluns, can be used to obtain the noise correlation matrix of a four-port differential device. Then by using the theory on the noise correlation matrix described in Chapter 3, the derived noise correlation matrix can be used to obtain the noise parameters of the DUT from which the noise performance can be solved for any input termination. This measurement procedure was first published by Tiemeijer *et al.* in [5]. The proposed technique considers the impedance representation of a linear noisy four port network, as illustrated in figure 5.21.

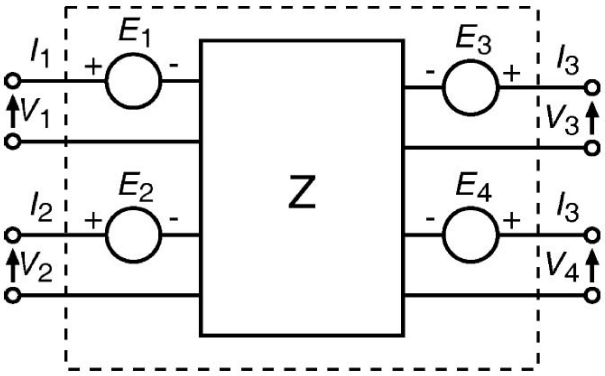

Figure 5.21: Impedance representation of a noisy four-port network, from [5].

Using the improved Y-factor method, the 2x2 sub-matrix $\mathbf{C}_{Z13}$ can be solved by performing a single ended measurement using ports 1 and 3, with ports 2 and 4 left open ended. The sub-matrix $\mathbf{C}_{Z13}$ is given by

$$\mathbf{C}_{Z13} = \begin{bmatrix} C_{Z.11} & C_{Z.13} \\ C_{Z.31} & C_{Z.33} \end{bmatrix} \tag{5.2.15}$$

Solving the noise parameters using the improved Y-factor method, discussed in section 5.1.4.2, the chain representation of the noise correlation matrix can be obtained and transformed to the equivalent impedance representation using the theory on the noise correlation matrix discussed in Chapter 3.

The other elements of the 16 element impedance correlation matrix can be obtained by repeating this measurement, however this can become a tedious task and leads to multiple values for the diagonal terms of the correlation matrix. The technique proposed by Tiemeijer *et al.* uses the theory on the mixed-mode noise correlation matrix, derived in section 6.2.1, to simplify this measurement procedure by first of all assuming that the network is sufficiently symmetrical such that the single ended noise correlation matrix $\mathbf{C}_{Z13}$ equals $\mathbf{C}_{Z24}$ - the noise correlation matrix obtained by performing a single ended noise measurement using ports 2 and 4 with ports 1 and 3 left open ended. Also due to symmetry the cross-mode elements of the mixed-mode correlation can be neglected. Resulting in the mixed-mode noise correlation matrix in equation 5.2.16

$$\mathbf{C}_{Z_{MM}} = \begin{bmatrix} C_{Z_{MM}.11} & C_{Z_{MM}.12} & 0 & 0 \\ C_{Z_{MM}.21} & C_{Z_{MM}.22} & 0 & 0 \\ 0 & 0 & C_{Z_{MM}.33} & C_{Z_{MM}.34} \\ 0 & 0 & C_{Z_{MM}.43} & C_{Z_{MM}.44} \end{bmatrix} \tag{5.2.16}$$

where subscripts MM.1 and MM.2 denote differential signals at the input and output, and MM.3 and MM.4 denote common-mode signals at the input and output, respectively. The mixed mode noise correlation matrix can therefore be derived by performing one differential and one common-mode noise measurement. Due to the fact that differential amplifiers exhibit high common mode rejection, the common-mode noise figure can prove difficult to measure. Therefore Tiemeijer *et al.* proposed the de-embedding of the remaining terms of the 4x4 impedance correlation matrix by performing one single ended noise measurement to obtain $\mathbf{C}_{Z13}$ and one differential noise measurement to obtain the differential sub-matrix

$$\mathbf{C}_{Z_{dd}} = \begin{bmatrix} C_{Z_{MM}.11} & C_{Z_{MM}.12} \\ C_{Z_{MM}.21} & C_{Z_{MM}.22} \end{bmatrix} \tag{5.2.17}$$

Similar to the differential noise figure measurement system of Abidi and Leete outlined in section 5.2.1, Tiemeijer *et al.* also suggests the use of baluns to measure the differential noise performance of the differential DUT where, instead of only measuring the differential noise factor of the device, the differential noise parameters of the device are determined by using the improved Y-factor method instead of the classical Y-factor method employed by Abidi and Leete.

The mixed mode differential sub-matrix $\mathbf{C}_{Z_{dd}}$ can then readily be solved from the extracted differential noise parameters. Recalling the mixed-mode impedance correlation matrix is determined using a relation analagous to that given in equation 6.2.19 the elements of the differential sub-matrix defined in equation 5.2.17 can be expressed in terms of the elements of the 4x4 impedance correlation matrix. That is,

$$C_{Z_{MM}.11} = C_{Z.11} - C_{Z.12} - C_{Z.21} + C_{Z.22} \tag{5.2.18}$$

$$C_{Z_{MM}.12} = C_{Z.13} - C_{Z.14} - C_{Z.23} + C_{Z.24} \tag{5.2.19}$$

$$C_{Z_{MM}.21} = C_{Z.31} - C_{Z.32} - C_{Z.41} + C_{Z.42} \tag{5.2.20}$$

$$C_{Z_{MM}.22} = C_{Z.33} - C_{Z.34} - C_{Z.43} + C_{Z.44} \tag{5.2.21}$$

Then using the assumption that $C_{Z13} = C_{Z24}$ due to symmetry, the remaining cross-correlation coefficients can be solved in terms of the elements of $\mathbf{C}_{Z13}$ and $\mathbf{C}_{Z_{dd}}$ giving

$$C_{Z.12} = C_{Z.21} = \frac{1}{2}\left(C_{Z.11} + C_{Z.22} - C_{Z_{MM.11}}\right) \tag{5.2.22}$$

$$C_{Z.14} = C_{Z.23} = \frac{1}{2}\left(C_{Z.13} + C_{Z.24} - C_{Z_{MM.12}}\right) \tag{5.2.23}$$

$$C_{Z.32} = C_{Z.41} = \frac{1}{2}\left(C_{Z.31} + C_{Z.42} - C_{Z_{MM.21}}\right) \tag{5.2.24}$$

$$C_{Z.34} = C_{Z.43} = \frac{1}{2}\left(C_{Z.33} + C_{Z.44} - C_{Z_{MM.22}}\right) \tag{5.2.25}$$

In this way the full 4x4 impedance noise correlation matrix, from which the noise performance of the linear four-port network can be predicted in any port termination, is solved.

5.2.3 De-embedding the Differential Noise Figure without the use of Baluns

Although the use of baluns or hybrids simplifies the measurement procedure, proper de-embedding of the baluns/hybrids can prove to be a difficult task. Furthermore the baluns and hybrids used in the measurements might limit the frequency range of the measurement and wideband measurements may therefore require more than one set of baluns or hybrids during measurement. Belostotski proposed a technique through which the differential noise figure of a four-port network can be de-embedded by performing single ended measurements between two ports with the unused ports terminated in matched loads [47]. Similar to the technique proposed by Abidi and Leete, Belostotski's measurement procedure only de-embeds the differential noise figure of the device. In this respect, the method proposed by Tiemeijer *et al.* proves more advantageous as it provides the full differential noise parameters of the device, making it possible to characterise the differential noise performance of the device in any arbitrary port termination. However, due to the fact that the differential LNA design considered in the scope of this text comprises of an output 180°-hybrid coupler, the measurement techniques discussed in sections 5.2.1 and 5.2.2 can not be applied to this design since both procedures incorporate an output balun that requires de-embedding to obtain the differential noise performance. Therefore, Belostotski's technique, published in [47], is applied in this section to derive an expression for the differential noise figure of a differential LNA in terms of the noise figures of two single-ended measurements.

A schematic representation of the differential LNA design discussed in chapter 6 is shown in figure 5.22.

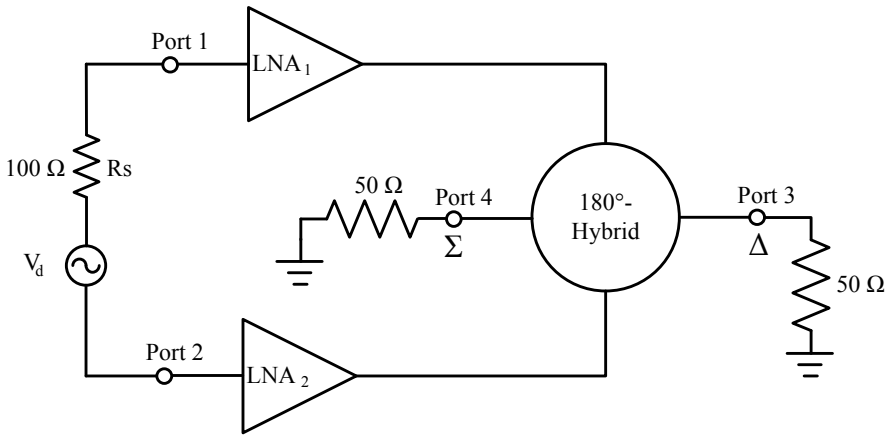

Figure 5.22: Schematic representation of the differential LNA driven by a differential excitation.

The differential LNA consists of a differential 100Ω input port comprising of single-ended ports 1 and 2, connected to two single ended Low Noise Amplifiers (LNAs), feeding a hybrid coupler with difference and sum 50Ω output ports 3 and 4.
By representing the differential input of the LNA as two 50Ω input ports referenced to ground, as indicated in figure 5.23, the transducer gain G_{31} as well as the equivalent single-ended noise factor F_{31} can be measured, with ports 2 and 4 terminated in 50Ω loads. The measured single-ended noise factor can then be expressed as

$$F_{31} = 1 + \frac{N_{31}}{kT_0 G_{31} \Delta f} \tag{5.2.26}$$

where N_{31} is the output noise measured at port 3 due to the LNA alone (N_3) as well as the terminations on ports 2 and 4. That is, with transducer gains G_{yx} representing the gain from port x to port y, the output noise at port 3 can be expressed as

$$N_{31} = N_3 + G_{32} kT_0 \Delta f + G_{34} kT_0 \Delta f \tag{5.2.27}$$

Furthermore, the output noise power due to the LNA alone can be expressed in terms of two uncorrelated equivalent input referred noise powers at ports 1 and 2, as shown in figure 5.23

$$N_3 = G_{31} N_{e1} + G_{32} N_{e2} \tag{5.2.28}$$

or if expressed in equivalent noise temperatures

$$T_3 = G_{31} T_{e1} + G_{32} T_{e2} \tag{5.2.29}$$

Using equations 5.2.27 to 5.2.29, the noise factor expressed in equation 5.2.26 can be expressed in terms of the equivalent input referred noise temperatures of each LNA

$$F_{31} = 1 + \frac{T_{e1}}{T_0} + \frac{G_{32}}{G_{31}} \left(1 + \frac{T_{e2}}{T_0} \right) + \frac{G_{34}}{G_{31}} \tag{5.2.30}$$

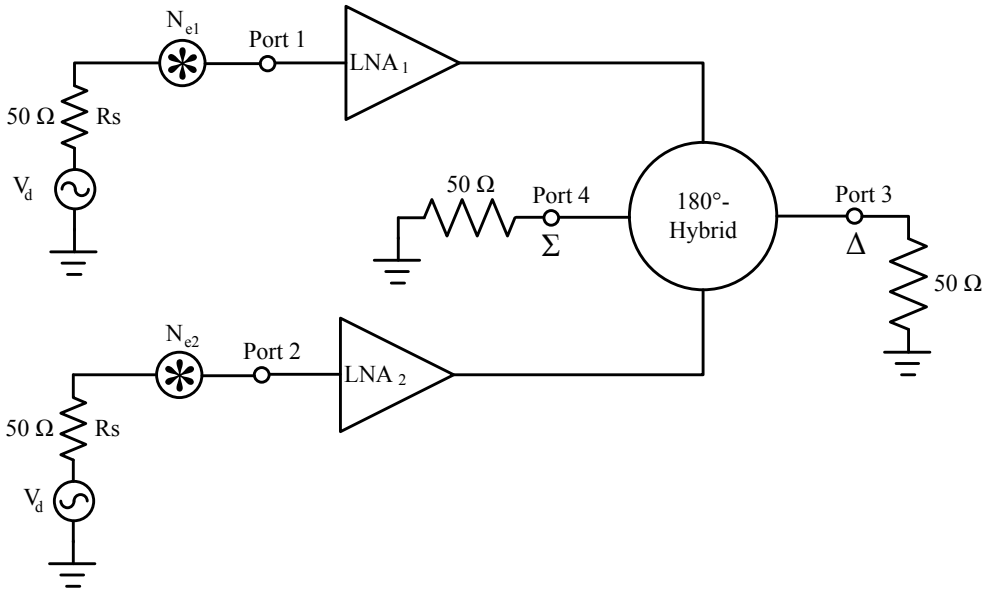

Figure 5.23: Noise contribution of the LNA represented by two uncorrelated input referred noise sources.

In a similar fashion, the noise factors F_{32}, F_{41}, and F_{42} can be measured by terminating the idle ports in 50Ω terminations. These noise factors can readily be expressed in terms of the equivalent input referred noise temperatures by repeating the procedure outlined above, giving

$$F_{32} = 1 + \frac{T_{e2}}{T_0} + \frac{G_{31}}{G_{32}}\left(1 + \frac{T_{e1}}{T_0}\right) + \frac{G_{34}}{G_{32}} \tag{5.2.31}$$

$$F_{41} = 1 + \frac{T_{e1}}{T_0} + \frac{G_{42}}{G_{41}}\left(1 + \frac{T_{e2}}{T_0}\right) + \frac{G_{43}}{G_{41}} \tag{5.2.32}$$

$$F_{42} = 1 + \frac{T_{e2}}{T_0} + \frac{G_{41}}{G_{42}}\left(1 + \frac{T_{e1}}{T_0}\right) + \frac{G_{43}}{G_{42}} \tag{5.2.33}$$

The extraction of the differential noise factor can be simplified further by only considering the output noise power at the differential port of the hybrid coupler, port 3, and taking the isolation between the sum and difference ports to be sufficiently large such that the gain G_{34} can be neglected without introducing too much of an error. With these simplifying assumptions taken into account, the noise factors of equations 5.2.30 and 5.2.31 reduce to

$$F_{31} = 1 + \frac{T_{e1}}{T_0} + \frac{G_{32}}{G_{31}}\left(1 + \frac{T_{e2}}{T_0}\right) \tag{5.2.34}$$

$$F_{32} = 1 + \frac{T_{e2}}{T_0} + \frac{G_{31}}{G_{32}}\left(1 + \frac{T_{e1}}{T_0}\right) \tag{5.2.35}$$

Similar to the standard two-port noise factor definition, the differential noise factor is defined as the ratio of the total differential noise power at the output, to the portion of the output noise power produced by the source. Since the noise power produced by a differential source is still $kT_0\Delta f$, the differential noise power produced by the LNA needs to be solved. This can be done by considering the equivalent thermal noise model representing the input referred noise at ports 1 and 2 by an equivalent increase in ambient temperature. The differential noise power can be solved by connecting the signal sources together instead of to ground as shown in figure 5.24.

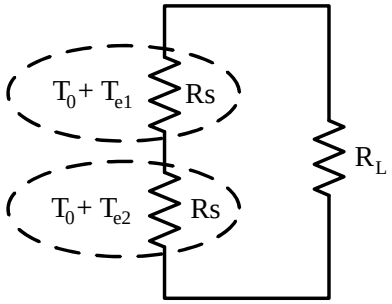

Figure 5.24: Equivalent thermal network representing the differential noise contribution of the LNA.

The maximum noise power delivered to the load R_L equals

$$P_{nT} = \left(\frac{\overline{V_{nT}}}{2}\right)^2 \left(\frac{1}{R_L}\right) \tag{5.2.36}$$

where the total thermal noise voltage produced by the two uncorrelated sources is given by

$$\overline{V_{nT}}^2 = \overline{V_{n1}}^2 + \overline{V_{n2}}^2 \tag{5.2.37}$$

$$= 4k\left(T_0 + T_{e1}\right)R\Delta f + 4k\left(T_0 + T_{e2}\right)R\Delta f \tag{5.2.38}$$

The differential noise power delivered to the matched load can therefore be expressed as

$$P_{nT} = \frac{k\left(2T_0 + T_{e1} + T_{e2}\right)\Delta f}{2} \tag{5.2.39}$$

which equals the total differential noise power produced by the source and the LNA. The differential noise factor can then be defined as

$$F_d = \frac{k\left(2T_0 + T_{e1} + T_{e2}\right)\Delta f}{2kT_0\Delta f} \tag{5.2.40}$$

$$= 1 + \frac{T_{e1} + T_{e2}}{2T_0} \tag{5.2.41}$$

Observe that the expression for the differential noise factor reduces to the standard single-ended definition when the equivalent input referred noise temperatures at the two input ports are assumed equal. That is, for

$$T_{e1} = T_{e2} = T_e \tag{5.2.42}$$

equation 5.2.41 reduces to equation 5.1.4.

5.3 Extracting the Differential noise factor

In section 5.2 an expression for the differential noise factor, equation 5.2.41, of a differential LNA is derived in terms of the two equivalent input referred noise temperatures T_{e1} and T_{e2}. By performing two single-ended measurements the measured noise factors and gains can be expressed in terms of T_{e1} and T_{e2}, as in equations 5.2.34 and 5.2.35. However, since equations 5.2.34 and 5.2.35 are linearly dependent, unique solutions for T_{e1} and T_{e2} can not be obtained.

Therefore the noise power at port 3 due to the LNA alone is solved in terms of the measured noise factors (F_{31} and F_{32}) and respective gains (G_{31} and G_{32}). That is, by substituting equation 5.2.27 into equation 5.2.26, the output noise power due to the LNA alone, is solved to be equal to

$$N_3 = kT_0\left[(F_{31}-1)\,G_{31} - G_{32}\right] \tag{5.3.1}$$

and, in a similar fashion it can be shown that

$$N_3 = kT_0\left[(F_{32}-1)\,G_{32} - G_{31}\right] \tag{5.3.2}$$

To reduce measurement uncertainties, N_3 is defined as the average of equations 5.3.1 and 5.3.2 such that

$$N_3 = \frac{kT_0}{2}\left[(F_{32}-2)\,G_{31} + (F_{32}-2)\,G_{32}\right] \tag{5.3.3}$$

By comparing equation 5.3.3 to equation 5.2.28 the equivalent input referred noise temperatures can be expressed in terms of F_{31} and F_{32}

$$T_{e1} = (F_{31}-2)\,\frac{T_0}{2} \tag{5.3.4}$$

$$T_{e2} = (F_{32}-2)\,\frac{T_0}{2} \tag{5.3.5}$$

The differential noise factor can therefore be solved from the two single ended noise factor measurements, giving the relationship

$$F_d = \frac{F_{31}+F_{32}}{4} \tag{5.3.6}$$

Note that equation 5.3.6 applies only for the ideal scenario when no deviation in gains G_{31} and G_{32} can be assumed. Considering the fact that measured single ended noise figures F_{31} and F_{32} are dependent on the measured gain it would be useful to define the deviation of the measured differential noise figure due to deviations in gain measurements. This is done by defining two constants k_0 and Δ in terms of the gain ratios, where

$$k_0 = \frac{1}{2}\left[\frac{G_{32}}{G_{31}} + \frac{G_{31}}{G_{32}}\right] \tag{5.3.7}$$

$$\frac{G_{32}}{G_{31}} = k_0 + \Delta \tag{5.3.8}$$

$$\frac{G_{31}}{G_{32}} = k_0 - \Delta \tag{5.3.9}$$

Using equations 5.3.7 to 5.3.9 a new expression for the differential noise figure is derived, taking the effect of the deviation in the two gains into account. That is,

$$F_d = \frac{(2+\Delta)F_{31} + (2-\Delta)F_{32}}{2(k_0+1)^2} \tag{5.3.10}$$

Observe that for equal gains it follows that $k_0 = 1$ and $\Delta = 0$ and so equation 5.3.10 reduces to equation 5.3.6.

5.4 Experimental Verification of Differential noise factor Extraction

In order to verify the expressions for extracting the differential noise factor from two single-ended noise factor measurements, discussed in section 5.3, the differential LNA network shown in figure 5.22 is simulated in MWO AWR using ideal network elements. The simulated network consists of noise sources connected to the input of two ideal gain elements, representing the noiseless LNAs, and the output of the two gain elements are combined differentially by means of an ideal 180°-Hybrid coupler. The two simulated single-ended networks are shown in figures 5.25, and 5.26.

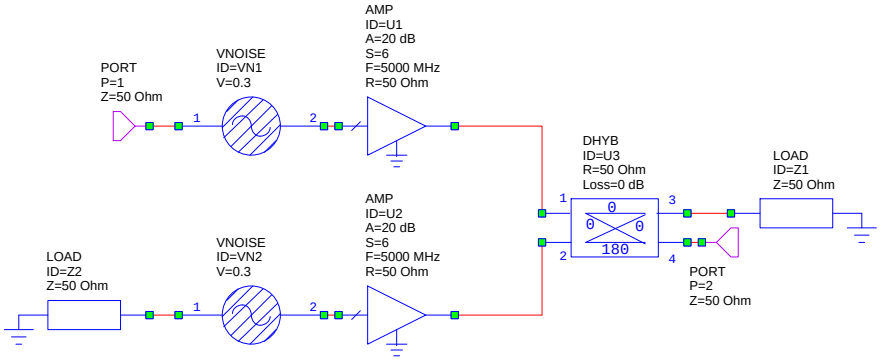

Figure 5.25: Single-ended noise figure measurement with ports 2 and 4 terminated.

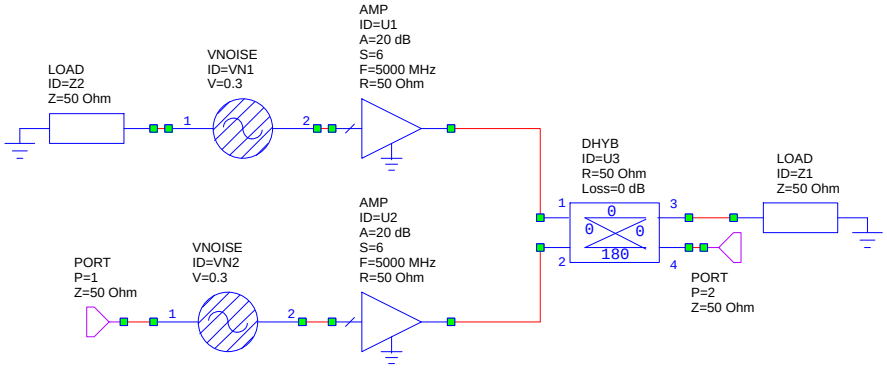

Figure 5.26: Single-ended noise figure measurement with ports 1 and 4 terminated.

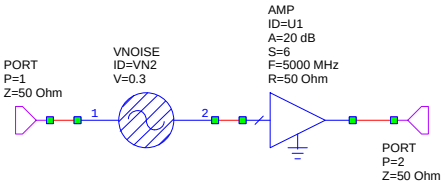

Figure 5.27: Simulated single-ended LNA.

The aim of this investigation is to determine the validity of equation 5.3.10, by comparing the extracted differential noise figure to the differential noise figure simulated using a differential excitation. Figure 5.28 shows the differential LNA excited by a differential source through the implementation of a Mixed Mode Converter. Note that the input port (Port 1) is applied to the differential port of the Mixed Mode Converter, and therefore, applying the theory on mixed mode transmission line theory discussed in Chapter 4, the characteristic impedance of the differential input port is equal to $Z_d = 2Z_0 = 100\Omega$ and common-mode port is terminated in $Z_c = Z_0/2 = 25\Omega$.

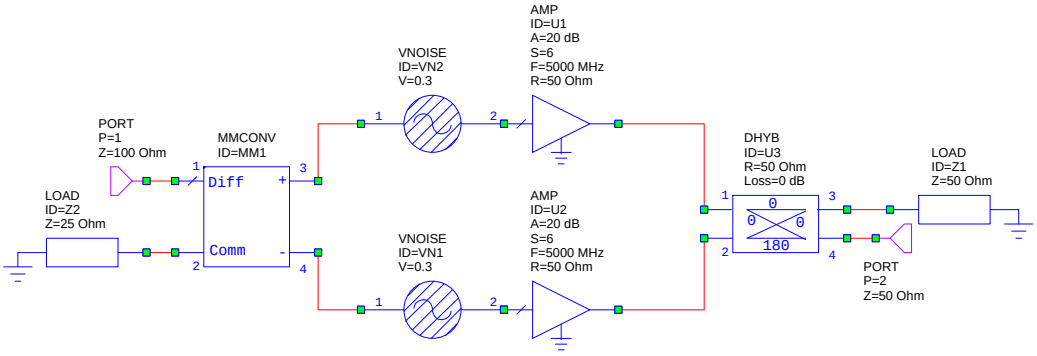

Figure 5.28: Simulated circuit schematic for differentially excited LNA.

5.4.1 Case 1: Equal Gains with Different Noise Contribution

Consider the case where the gains of the amplifiers are equal but have different noise contribution. For equal gains the extracted noise figure calculated from equation 5.3.6 equals the expression for the differential noise factor derived in section 5.2. This is verified when considering the graph in figure 5.29 comparing the extracted differential noise figure solved from the two single-ended noise figures to that of the simulated differential noise figure of the network in figure 5.28.

5.4.2 Case 2: Equal Noise Contribution with Different Gains

As explained in section 5.2 the expression for the differential noise figure given in equation 5.2.41 reduces to the expression for the single-ended noise figure of a single LNA when the noise contribution of the two LNAs are assumed equal. However, using equation 5.3.6, it can be shown that the differential noise figure will deviate from the value of the single-ended noise figure when gains of the two amplifiers in the differential LNA are not equal and therefore equation 5.3.10 is used to de-embed the differential noise figure. The graph in figure 5.30 shows the differential noise figure simulated using the differential excitation of the network in figure 5.28, the single-ended noise figure of the network in figure 5.27, as well as the differential noise figure de-embedded using the relationship in equation 5.3.10. By comparing the extracted and simulated single-ended noise figures, it is clear the equation 5.3.10 provides an accurate theoretical description of the deviation due to unequal amplifier gains, observed in differential noise figure measurement.

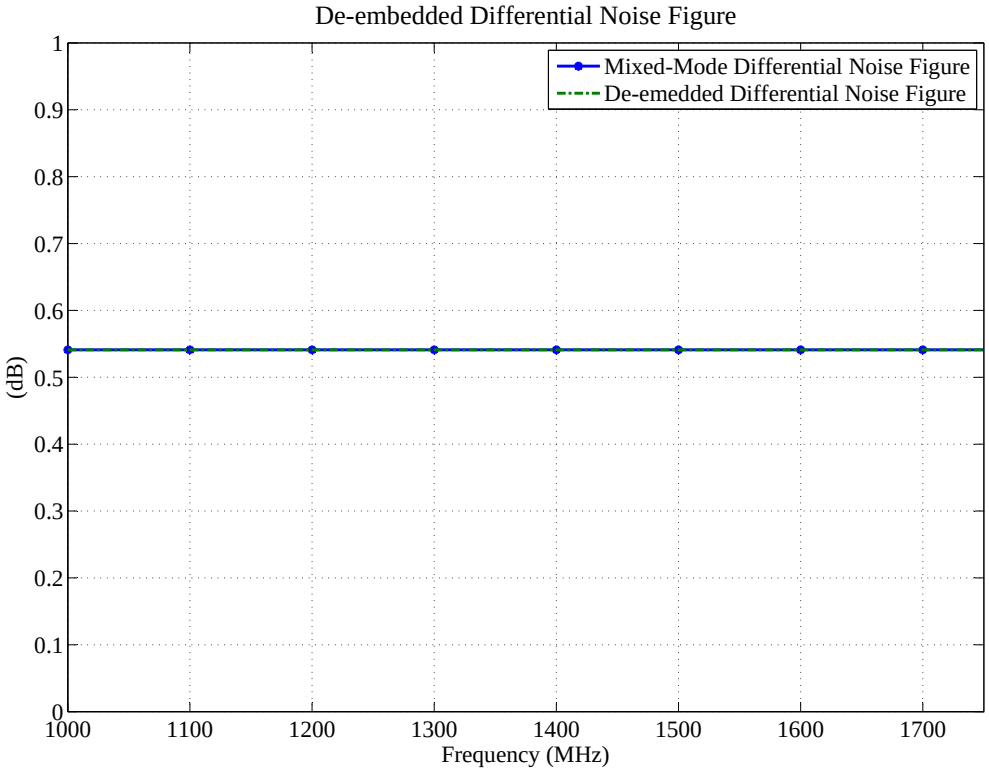

Figure 5.29: Comparing the extracted differential noise figure to the noise figure obtained from a differential excitation.

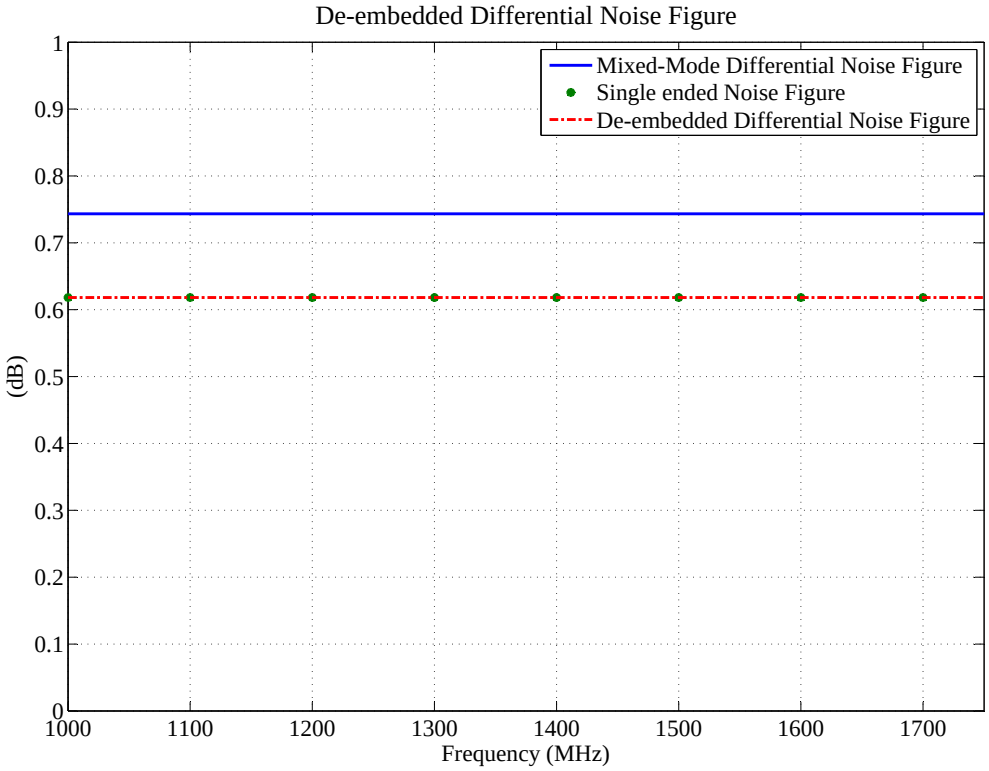

Figure 5.30: De-embedded differential noise figure validated.

5.5 Conclusion

This chapter introduced the theory of the Y-factor noise figure measurement procedure that forms the basis for the internal operation of most single-ended noise figure measurement instruments. The measurement system used to measure the results discussed in Chapter 6 was discussed, as well as methods to increase noise figure measurement accuracy. Then, based on two single-ended measurements an expression for the differential noise figure was derived and verified using two case studies. The first case study confirmed that the differential noise figure can be accurately extracted from two single-ended measurements, when the gain curves of the two amplifiers are considered equal. Whereas the second case study quantified the deviation from the ideal differential noise figure caused by a difference in amplifier gains. The differential noise figure extraction described in this chapter is applied to all the measured results given in Chapter 6.

Chapter 6

Differential Low Noise Amplifier Design and Noise Figure Verification

This chapter applies the signal and noise characteristics of differential circuits discussed in the preceding chapters to the design of L-band Differential Low Noise Amplifiers (dLNAs). The two main topologies of differential amplifiers, balanced and differential, are illustrated in figure 6.1, with the predominant difference between the two topologies being that the differential topology displays inherent common-mode suppression. As mentioned in the Introduction, the subsequent receiver blocks after the low noise gain block in the proposed receiver front end, are all commonly implemented using single ended devices. Therefore, the dLNA implemented in the low noise gain block needs to convert the balanced antenna output into a single ended output that can be connected to the remaining receiver chain. A single ended output is generally realised in differential topology by inserting an active load along the signal path of one of the amplifiers and using the other as an unbalanced output. The use of active loads can realise high open circuit differential gain, that can decrease severely due to loading effects and therefore a gain stage with a high input impedance usually precedes the unbalanced output.

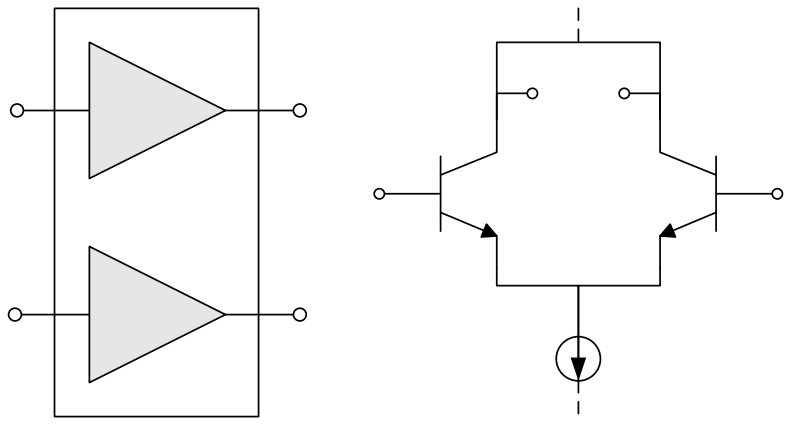

(a) (b)

Figure 6.1: Two main topologies of differential amplifiers: (a) Balanced topology (b) and Differential topology.

The dLNA designs discussed in this chapter consists of a balanced amplifier topology feeding a 180°-Hybrid Coupler in order to convert the balanced output into a single ended output while suppressing common-mode signals. It follows from the theory discussed in Chapter 5 that the noise performance of the dLNA should equal that of its constituent single ended amplifiers, provided that the gains along the two signal paths, as well as the noise contribution of each amplifier, are equal. Therefore, when implementing this design it is essential that the single ended Low Noise Amplifiers (LNAs) are well paired to ensure similar noise contribution and that the insertion loss along the two differential signal paths of the passive coupler are equal in order to measure the same differential noise performance as that of the constituent single ended LNAs. This chapter first considers the operation of narrowband couplers and derives the performance criteria for 180°-Hybrid couplers [15]. Thereafter a number of wideband phase inverting structures are introduced, one of which is implemented in a wideband 180°-Hybrid Ring coupler design that will be incorporated into the final dLNA design. The LNA design methodology as well as the integration of the LNAs and the Hybrid coupler are discussed and in conclusion the measured response of the dLNA design is analysed.

6.1 Planar Four-Port Couplers

Consider the reciprocal four-port network in figure 6.2.

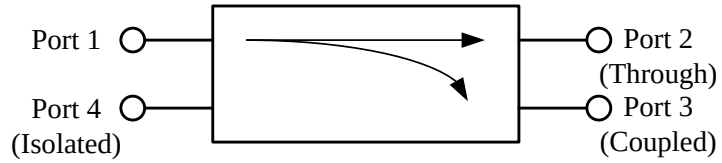

Figure 6.2: Schematic representaion of a reciprocal four-port directional coupler.

Given that the network is lossless and matched at all ports, the scattering matrix of the network is

$$[S] = \begin{bmatrix} 0 & S_{12} & S_{13} & S_{14} \\ S_{21} & 0 & S_{23} & S_{24} \\ S_{31} & S_{32} & 0 & S_{34} \\ S_{14} & S_{24} & S_{34} & 0 \end{bmatrix} \tag{6.1.1}$$

where the matrix $[S]$ is unitary [15] and therefore

$$\sum_{k=1}^{N} S_{ki} S_{kj}^{*} = \delta_{ij} \quad \forall \quad i, j \tag{6.1.2}$$

where

$$\delta_{ij} = 1 \quad if \quad i = j \tag{6.1.3}$$

$$\delta_{ij} = 0 \quad if \quad i \neq j \tag{6.1.4}$$

By assuming ports 1 and 4 and ports 2 and 3 to be completely isolated such that $S_{14} = S_{23} = 0$, the four-port network can be considered as a directional coupler and it can be shown, from the relation of equation 6.1.3, that

$|S_{13}| = |S_{24}|$ and $|S_{12}| = |S_{34}|$. Furthermore, by choosing the phase reference on three of the ports, it follows that $S_{12} = S_{34} = \alpha$, $S_{13} = \beta e^{j\theta}$, and $S_{24} = \beta e^{j\phi}$ where it can readily be shown that the angles θ and ϕ are related to one another by

$$\theta + \phi = \pi \tag{6.1.5}$$

using the unitary conditions of equations 6.1.2 and 6.1.4. Therefore, by choosing the phase references such that $\theta = 0$ equation 6.1.5 implies that $\phi = 180^\circ$, yielding an Anti-symmetrical directional coupler with the following scattering matrix

$$[S] = \begin{bmatrix} 0 & \alpha & \beta & 0 \\ \alpha & 0 & 0 & -\beta \\ \beta & 0 & 0 & \alpha \\ 0 & -\beta & \alpha & 0 \end{bmatrix} \tag{6.1.6}$$

It should be noted that the terms α and β are related to one another by

$$\alpha^2 + \beta^2 = 1 \tag{6.1.7}$$

Let the scattering matrix in equation 6.1.6 define the operation of the four-port network illustrated in figure 6.2. Using this configuration the operation of an Anti-symmetrical coupler can be described. Assuming that the input power is applied to port 1, it follows from equation 6.1.6 that the power coupled to port 3 $|S_{13}|^2 = \beta^2$ and consequently, the output power at port 2 can be solved, from the relation in equation 6.1.7, to be $|S_{12}|^2 = \alpha^2$. The fraction of input power coupled to the output port is indicated by the coupling factor given by

$$C = 10log\frac{P_1}{P_3} = -20log\beta \tag{6.1.8}$$

Two other quantities that characterise the operation of directional couplers are the directivity, D, and the isolation ,I

$$D = 10log\frac{P_3}{P_4} = 20log\frac{\beta}{|S_{14}|} \tag{6.1.9}$$

$$I = 10log\frac{P_1}{P_4} = -20log|S_{14}| \tag{6.1.10}$$

The 180°-Hybrid coupler is a special case of Anti-symmetrical directional coupler where the coupling factor is equal to 3 dB, implying that the input power applied to port 1 is split evenly between ports 2 and 3 and hence $\alpha = \beta = 1/\sqrt{2}$. Therefore, the scattering matrix of an ideal 180°-Hybrid has the following form

$$[S] = \frac{1}{\sqrt{2}} \begin{bmatrix} 0 & 1 & 1 & 0 \\ 1 & 0 & 0 & -1 \\ 1 & 0 & 0 & 1 \\ 0 & -1 & 1 & 0 \end{bmatrix} \tag{6.1.11}$$

6.1.1 The 180°-Hybrid Coupler

The 180°-Hybrid coupler is a four-port device that can split the input power evenly either in-phase or 180° out of phase between two ports. To illustrate this consider the scattering matrix of a 180°-Hybrid expressed in equation 6.1.11. It is clear from equation 6.1.11 that the power applied to port 1 is split evenly and in-phase between output ports 2 and 3 whereas the power applied to port 4 is split evenly but 180° out of phase between ports 2 and 3. Therefore port 1 is referred to as the *sum* port and port 4 as the *difference* port, denoted by $\sum$ and Δ respectively. The schematic representation of the four-port device is illustrated in figure 6.3.

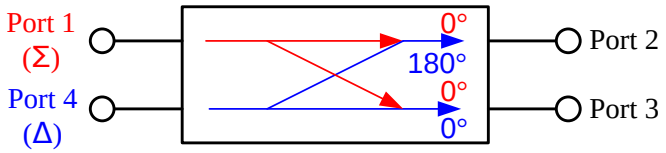

Figure 6.3: Schematic representation of 180°-Hybrid Coupler.

These hybrid couplers are generally implemented in planar form by either a ring structure or tapered coupled lines. Both these structures are illustrated in figure 6.4.

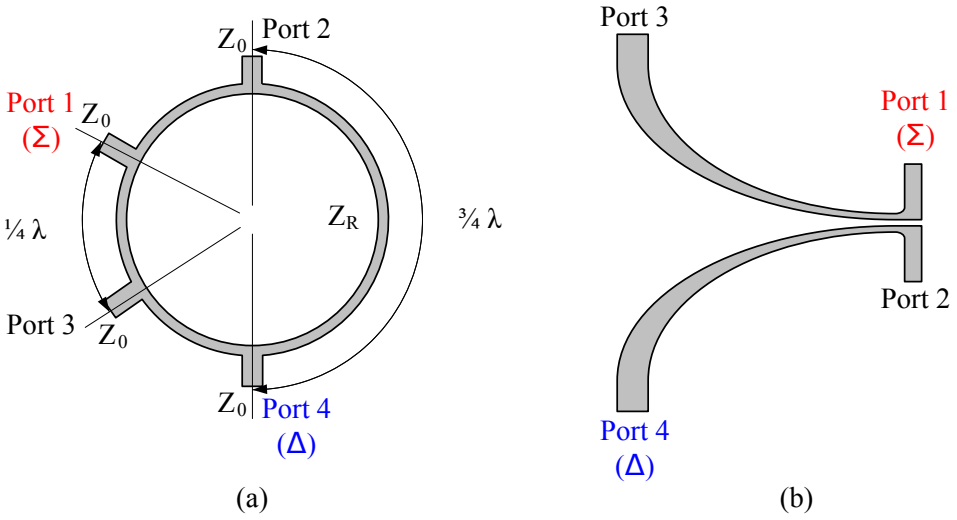

Figure 6.4: Planar (a) 180°-Hybrid Ring and (b) Tapered Coupled Line Coupler.

The Hybrid ring coupler, also referred to as the 'Rat-Race' coupler, consists of four ports with characteristic impedance Z_0, connected to a ring structure with characteristic impedance $Z_R = \sqrt{2}Z_0$ as indicated in figure 6.4.(a). Upon inspection it is apparent that a signal applied to the difference port, port 4, is split evenly between output ports 2 and 3, and due to the added half wavelength delay along the signal path to port 2, these signals are 180° out of phase. Also, a signal applied to the sum port, port 1, is split evenly and in phase between output ports 2 and 3. Conversely, two signals applied to ports 2 and 3 are added to one another at the output of port 1 and subtracted from one another at the output of port 4.

6.1.1.1 Even and Odd Mode Analysis

In order to determine the response at each port when a signal of unit amplitude is applied to port 1, the even and odd mode analysis of symmetrical networks, published by Reed and Wheeler in [48], is used. First consider the symmetric four-port network in figure 6.5.

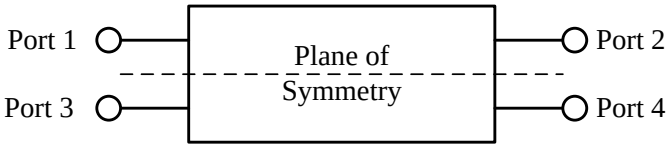

Figure 6.5: Symmetrical four-port network.

If two signals of amplitude of $1/2$ are applied in-phase to ports 1 and 3 the four-port network can be represented by an equivalent two-port network with an open circuit along the plane of symmetry. Similarly, applying two $1/2$ amplitude signals 180° out of phase to ports 1 and 3, the equivalent two-port network is shorted along the plane of symmetry. Note that the superposition of the even and odd mode cases result in a single excitation of unit amplitude at port 1. Therefore denoting the reflection and transmission coefficient of the even mode equivalent two port by $\frac{1}{2}\Gamma_e$, and $\frac{1}{2}T_e$, and that of the odd mode equivalent two port by $\frac{1}{2}\Gamma_o$, and $\frac{1}{2}T_o$, the amplitudes of the scattered waves at each port can be expressed as [15]

$$B_1 = \frac{1}{2}\Gamma_e + \frac{1}{2}\Gamma_o \tag{6.1.12}$$

$$B_2 = \frac{1}{2}T_e + \frac{1}{2}T_o \tag{6.1.13}$$

$$B_3 = \frac{1}{2}\Gamma_e - \frac{1}{2}\Gamma_0 \tag{6.1.14}$$

$$B_4 = \frac{1}{2}T_e - \frac{1}{2}T_o \tag{6.1.15}$$

Applying the even and odd mode analysis to ports 1 and 3 of a four-port Hybrid ring coupler, the two equivalent two-port circuits, shown in figure 6.6, are realised and the amplitudes of the scattered waves at each of the four ports, due to a unit amplitude excitation applied to port 1, can be solved using equations 6.1.12 to 6.1.15.

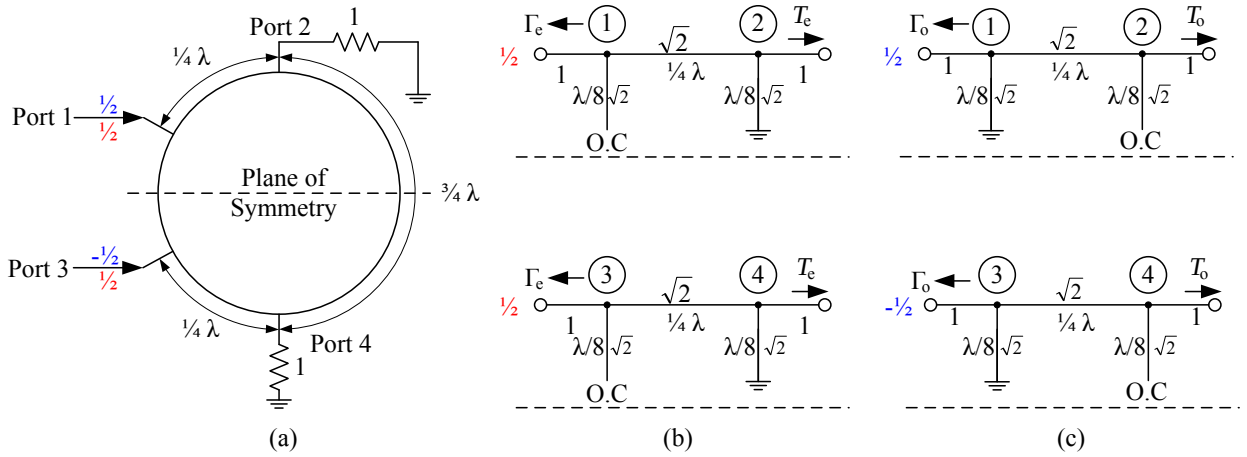

Figure 6.6: (a) Even and odd mode analysis applied to hybrid ring coupler excited at Port 1, (b) Equivalent two-port circuits for Even mode analysis, (c) and Odd mode analysis.

By solving the transmission matrix for the even and odd mode cases, the reflection and transmission coefficients can be determined. That is, by considering each of the equivalent two port circuits for the even and odd mode scenarios as the cascade of three two-port networks, the even and odd mode ABCD-matrices can easily be solved

$$\begin{bmatrix} A & B \\ C & D \end{bmatrix}_e = \begin{bmatrix} 1 & 0 \\ j\frac{1}{\sqrt{2}} & 1 \end{bmatrix} \begin{bmatrix} 0 & j\sqrt{2} \\ j\frac{1}{\sqrt{2}} & 0 \end{bmatrix} \begin{bmatrix} 1 & 0 \\ -j\frac{1}{\sqrt{2}} & 1 \end{bmatrix} = \begin{bmatrix} 1 & j\sqrt{2} \\ j\sqrt{2} & -1 \end{bmatrix} \tag{6.1.16}$$

$$\begin{bmatrix} A & B \\ C & D \end{bmatrix}_o = \begin{bmatrix} 1 & 0 \\ -j\frac{1}{\sqrt{2}} & 1 \end{bmatrix} \begin{bmatrix} 0 & j\sqrt{2} \\ j\frac{1}{\sqrt{2}} & 0 \end{bmatrix} \begin{bmatrix} 1 & 0 \\ j\frac{1}{\sqrt{2}} & 1 \end{bmatrix} = \begin{bmatrix} -1 & j\sqrt{2} \\ j\sqrt{2} & 1 \end{bmatrix} \tag{6.1.17}$$

Then, considering the fact that $\Gamma = S_{11}$ and $T = S_{21}$, the ABCD parameters can be used to solve the even and odd mode reflection and transmission coefficients. That is, given that, for a normalized port impedance

$$\Gamma = S_{11} = \frac{A+B-C-D}{A+B+C+D} \tag{6.1.18}$$

$$T = S_{21} = \frac{2}{A+B+C+D} \tag{6.1.19}$$

the even and odd mode reflection and transmission parameters equal

$$\Gamma_e = \frac{-j}{\sqrt{2}} \tag{6.1.20}$$

$$T_e = \frac{-j}{\sqrt{2}} \tag{6.1.21}$$

$$\Gamma_0 = \frac{j}{\sqrt{2}} \tag{6.1.22}$$

$$T_o = \frac{-j}{\sqrt{2}} \tag{6.1.23}$$

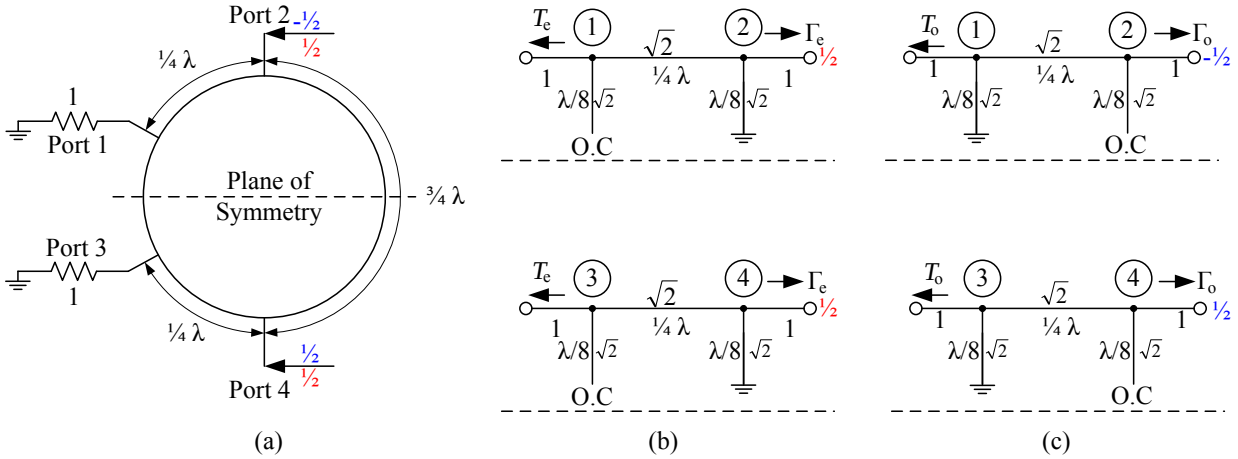

Figure 6.7: (a) Even and odd mode analysis applied to Hybrid ring coupler excited at Port 4, (b) Equivalent two-port circuits for Even mode analysis, (c) and Odd mode analysis.

Substituting equations 6.1.20 to 6.1.23 into equations 6.1.12 to 6.1.15 solves the scattered waves at each of the ports for a unit amplitude excitation applied to port 1,

$$B_1 = 0 \tag{6.1.24}$$

$$B_2 = \frac{-j}{\sqrt{2}} \tag{6.1.25}$$

$$B_3 = \frac{-j}{\sqrt{2}} \tag{6.1.26}$$

$$B_4 = 0 \tag{6.1.27}$$

Equations 6.1.24 to 6.1.27 indicates that port 1 is matched, completely isolated from port 4 and also that a signal applied to port 1 is split evenly and in-phase between ports 2 and 3. In a similar fashion, the response of the Hybrid ring coupler with a unit amplitude excitation applied to port 4 can be solved by considering the superposition of the even and odd mode excitations applied to ports 2 and 4. That is, using the equivalent two-port networks shown in figure 6.7, the scattered waves at the ports are found to be

$$B_1 = 0 \tag{6.1.28}$$

$$B_2 = \frac{j}{\sqrt{2}} \tag{6.1.29}$$

$$B_3 = \frac{-j}{\sqrt{2}} \tag{6.1.30}$$

$$B_4 = 0 \tag{6.1.31}$$

indicating that input difference port 4 is matched, isolated from port 1, and that a signal applied to port 4 is divided evenly and 180° out of phase between ports 2 and 3.

6.1.1.2 Narrowband Design

The 180°-Hybrid coupler considered in the even and odd mode analysis in Section 6.1.1.1 incorporates a 180° phase shift between the outputs at ports 2 and 3 when a signal is applied to the difference port, port 4. This phase shift is realised by the half wavelength added between ports 2 and 4 with respect to the signal path length between ports 3 and 4, making the bandwidth of the coupler very narrow. This is illustrated by considering the transmission line model of a hybrid ring coupler operating at a centre frequency, $f = 1.35$GHz, shown in figure 6.8.

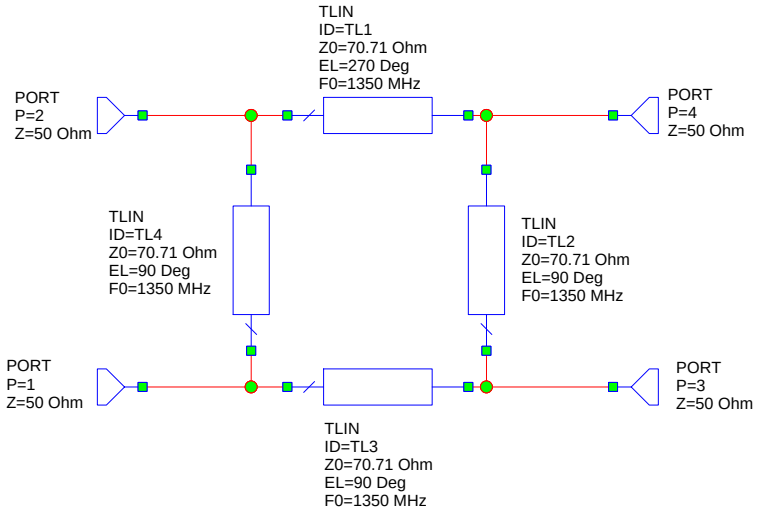

Figure 6.8: Transmission line model of narrowband hybrid ring coupler simulated in Microwave Office AWR.

The S-paramter magnitudes obtained when considering a signal applied to the difference port is shown in figure 6.9, indicating equal power division as well as excellent 50Ω port match for a ring impedance of 70.71Ω at the center frequency.

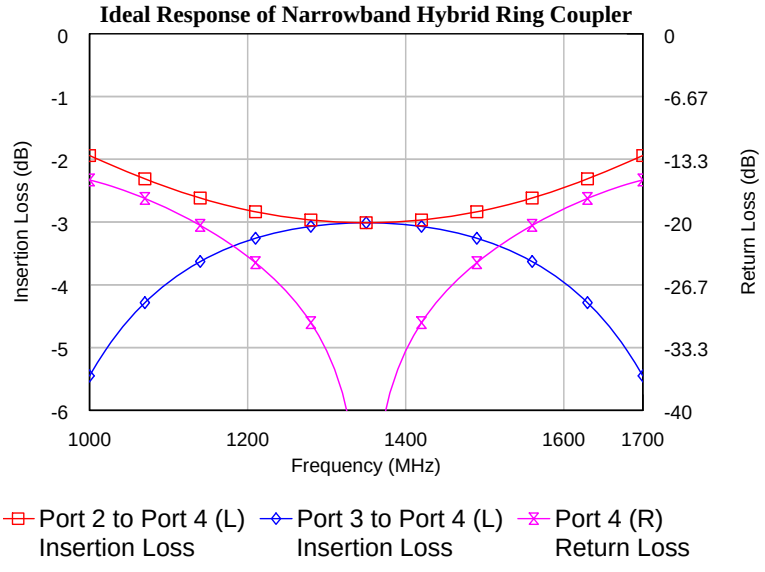

Figure 6.9: S-parameters of ideal hybrid ring coupler transmission line model.

It is clear from the phase comparison in figure 6.10 that the circuit operates ideally only at the designed frequency and that for a minimum phase deviation of only 5° the operating bandwidth is approximately 15% around the center frequency.

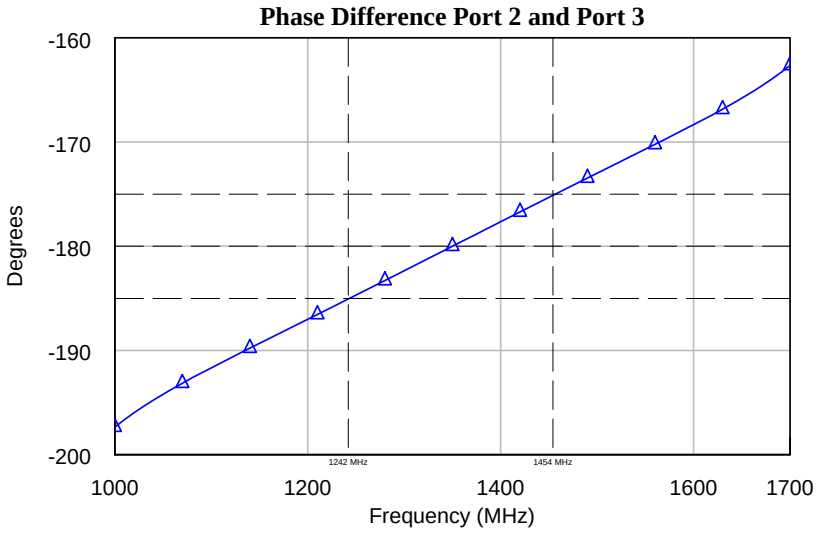

Figure 6.10: Comparison of the phase difference at Ports 2 and 3 for an excitation at Port 4.

The circumference of the narrowband Hybrid ring coupler is one and a half wavelength, which, at a frequency of 1.35GHz, gives a diameter of approximately 100mm when considering the free-space wavelength. When a signal propagates in a medium with a high effective dielectric constant (ε_{eff}), the wavelength shortens according to

$$\lambda_g = \frac{\lambda_0}{\sqrt{\varepsilon_{eff}}} \tag{6.1.32}$$

where λ_g denotes the wavelength in the waveguide and λ_0 the wavelength in free-space. Furthermore, by considering alternative wideband techniques to implement the 180° phase shift the size of the Hybrid ring coupler can be reduced significantly. Some of the techniques for increasing the operating bandwidth while decreasing the coupler diameter are discussed in section 6.1.2.

6.1.2 Wideband Reduced Size 180°-Hybrid Coupler Designs

There are a number of publications that introduce alternative phase inverting structures in order to increase the operating bandwidth of the Hybrid ring coupler. The first of these, introduced by March in [49], replaces the three quarter wavelength section with a pair of quarter wavelength equilateral broadside-coupled transmission lines shorted at opposing ends, thereby reducing the size of the coupler to two thirds of its original size and increasing the bandwidth to an octave. A schematic representation of this coupler design is shown in figure 6.11.

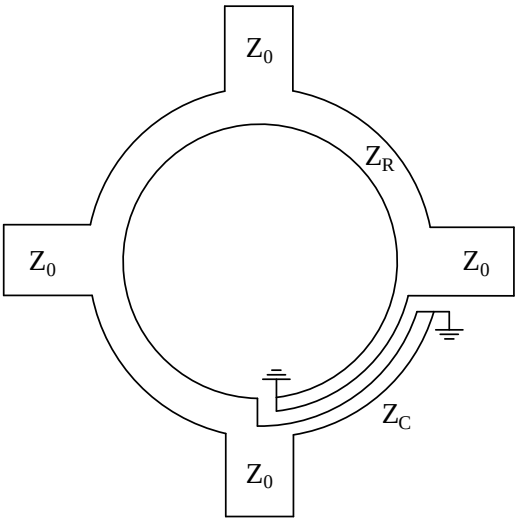

Figure 6.11: Microstrip Hybrid ring coupler incorporating a coupled line phase inverter.

The ABCD matrix of the shorted coupled line section is

$$\begin{bmatrix} -cos\theta & -jZ_r sin\theta \\ -jY_r sin\theta & -cos\theta \end{bmatrix} \tag{6.1.33}$$

It can be shown that the quarter wavelength shorted coupled line segment effectively simulates a 180° phase shift cascaded with a quarter wavelength transmission line segment by considering the cascaded ABCD matrices. That is,

$$\begin{bmatrix} -1 & 0 \\ 0 & -1 \end{bmatrix} \begin{bmatrix} cos\theta & jZ_r sin\theta \\ jY_r sin\theta & cos\theta \end{bmatrix} = \begin{bmatrix} -cos\theta & -jZ_r sin\theta \\ -jY_r sin\theta & -cos\theta \end{bmatrix} \tag{6.1.34}$$

Similar to the conventional narrowband coupler, the ring impedance equals $Z_R = \sqrt{2}Z_o$ where Z_o is the port impedance. This implies that the even and odd mode impedances (Z_{re} and Z_{ro}) of the shorted coupled line segment should equal approximately $Z_{re} = 170\Omega$ and $Z_{ro} = 30\Omega$ in order to achieve the necessary 3dB coupling required for equal power division while maintaining an impedance $Z_C = Z_R$ where

$$Z_C = \sqrt{Z_{re}Z_{ro}} \tag{6.1.35}$$

Due to the fact that these even and odd mode impedances are not easily obtained when implementing microstrip coupled lines, alternative designs are investigated.

Chien-Hsun Ho *et al.* investigated uniplanar CPW Hybrid ring couplers and introduced a novel quarter wavelength CPW-Slotline transition to replace the three-quarter wavelength segment of the conventional coupler [50]. The CPW-Slotline transition incorporated in the design is based on the operation of a reverse-phase microstrip back-to-back balun. The reverse-phase back-to-back tapered balun realised in microstrip, shown in figure 6.12, produces a phase reversal by switching the position of the ground plane from the top layer to the bottom layer.

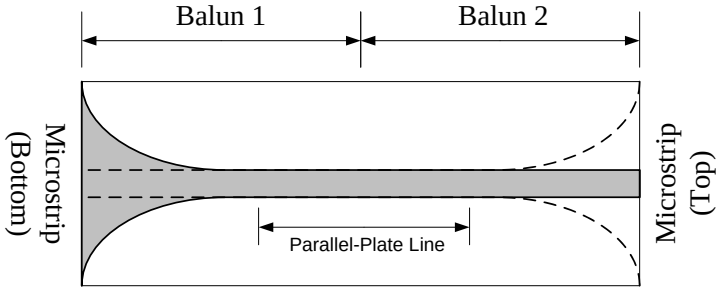

Figure 6.12: Microstrip Back-to-Back Balun phase inverter.

This type of design evidently requires a two sided implementation which would be difficult to implement with the existing Hybrid ring structure. Therefore Chien-Hsun Ho *et al.* introduced a similar back-to-back balun structure realised using a uniplaner CPW-Slotline transition. The proposed uniplanar back-to-back balun, shown in figure 6.13, implements two CPW-Slotline transitions using CPW shorts and slotline radial stubs situated at opposite sides of the internal slotline.

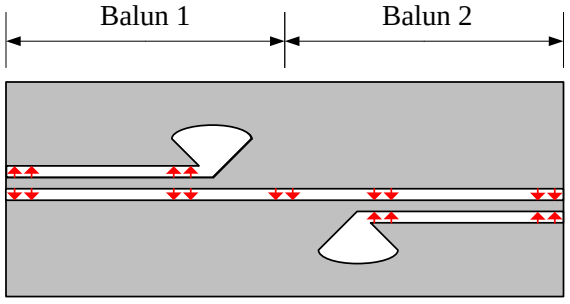

Figure 6.13: Coplanar waveguide to Slotline Back-to-Back Balun phase inverter.

It is clear that two sides of the internal slots connect the inner conductor (or ground plane) of the one balun to the ground plane (or inner conductor) of the other. Thus, considering the electric field distribution for an excitation applied to the CPW port of Balun 1, a 180° phase change is applied to the field direction at the output of the CPW port of Balun 2 due the internal slotline connecting the opposite sides of the CPW gaps of the two Baluns. An illustration of this transition incorporated into a Hybrid ring coupler is shown in figure 6.14.

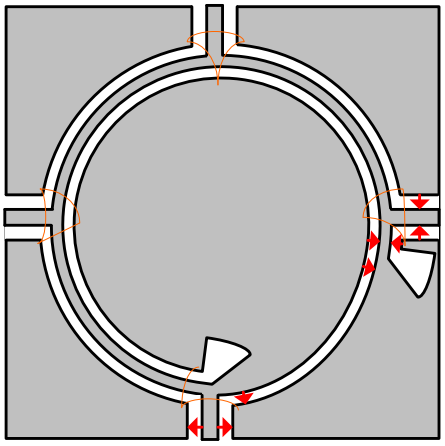

Figure 6.14: Uniplanar Coplanar Hybrid ring coupler with integrated CPW-Slotline Back-to-Back Balun.

Considering the fact that the coupler will be used in a 50Ω system, the ring impedance and therefore the impedance of the slot should equal 70.71Ω, an impedance that is difficult to realise when using substrates with high dielectric constants. Realising the Hybrid ring coupler in CPW leads to the advantage of using FGCPW, which allows for a near ideal phase inversion by a simple crossover between the finite ground conductors and the centre conductor. Such an inverter is shown in figure 6.15 and can be implemented at any point within the ring structure to cause a 180° phase difference between two ports [51].

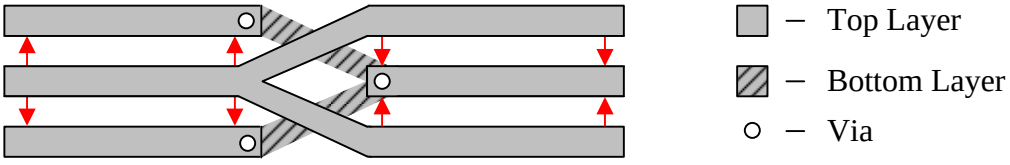

Figure 6.15: Finite Ground Coplanar waveguide phase inverter.

This of course removes the need for the added half wavelength implemented in the narrowband design and reduces the overall size to two thirds of that of the narrowband coupler. The response of a FGCPW Hybrid ring coupler, incorporating the phase inverter shown in figure 6.15, is analysed in section 6.1.3.

6.1.3 Finite Ground Coplanar Waveguide 180°-Hybrid Ring Coupler Design

The Hybrid ring coupler incorporated into the design of the dLNA is implemented using FGCPW, thereby allowing for wideband phase inversion between two of the ports. The response of the FGCPW inverter, depicted in figure 6.15, is investigated in AWR AXIEM. Figure 6.16.(a) shows a 50Ω FGCPW length of transmission line incorporating the phase inverter described in section 6.1.2.

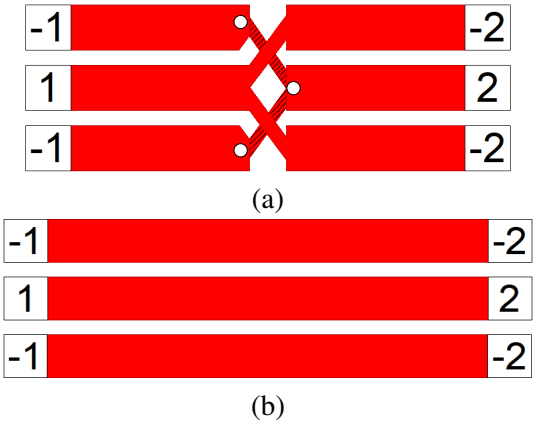

Figure 6.16: (a) Finite Ground Coplanar waveguide phase inverter and (b) through connection simulated in AXIEM.

In order to investigate the phase response of this inverter, the response is compared to a standard FGCPW 50Ω through segment of which the length has been adjusted to account for the length added by the inverting structure. This difference in transmission line length can be seen in figure 6.16. The phase response of these two circuits are compared in the graph shown in figure 6.17, indicating that the FGCPW phase inverter causes a near ideal phase inversion, deviating from 180° by less than half a degree across the entire L-band.

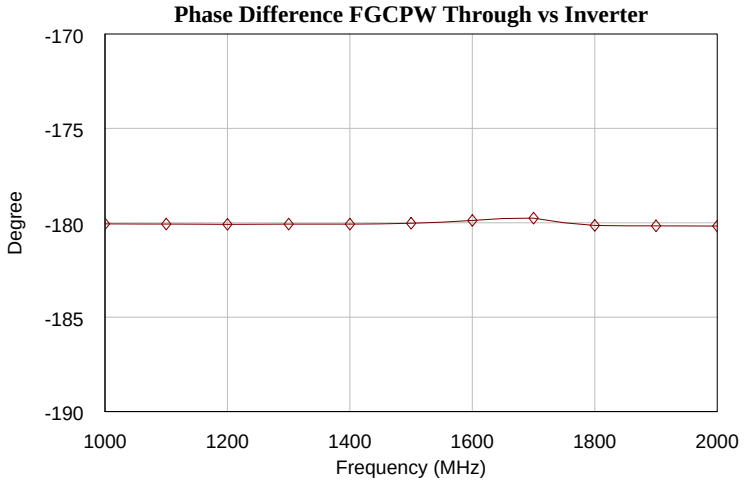

Figure 6.17: Simulated output phase comparison between FGCPW inverter and FGCPW through connection.

As mentioned in section 6.1.1, the size of the Hybrid ring coupler can be reduced significantly if manufactured on a substrate with a high dielectric constant. Therefore, the coupler is designed using Rogers RT/Duroid 6010 high frequency laminate that has a dielectric constant of 10.2. The thickness of the substrate is 0.635mm with half once copper cladding. Using these values, the FGCPW coupler is designed using the same gap width to realise the 50Ω port impedance as well as the 70.71Ω ring impedance. That is, gap width $g = 0.65$mm, port centre conductor width $w_{50} = 3.37$mm, and ring centre conductor width $w_{70.71} = 0.54$mm.

The Hybrid ring coupler with the phase inverter incorporated in one of the quarter wavelength lines as well as bond wires connecting the ground conductors at each port junction is shown in figure 6.18.

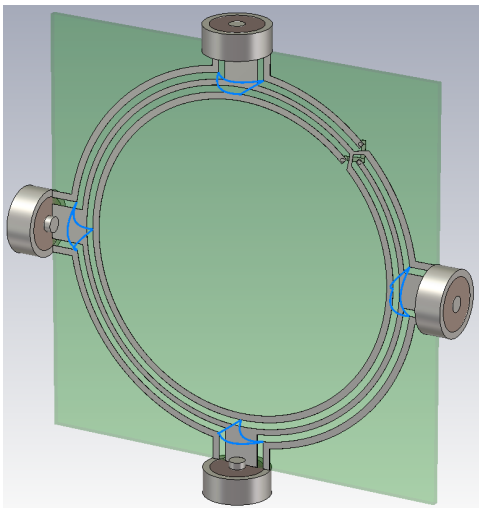

Figure 6.18: FGCPW 180°-Hybrid Ring coupler simulated in CST Microwave Studio.

The coupler depicted in figure 6.18 has been simulated in CST Microwave Studio. Note that, in order to achieve the phase inversion, the coupler is designed with no ground plane. CST allows for the definition of coplanar ports without a ground plane, but it has been found that better results are obtained when including coaxial ports in the simulations, as done in figure 6.18. The response is analysed using the graphs depicted in figures 6.19, 6.20, and 6.21.

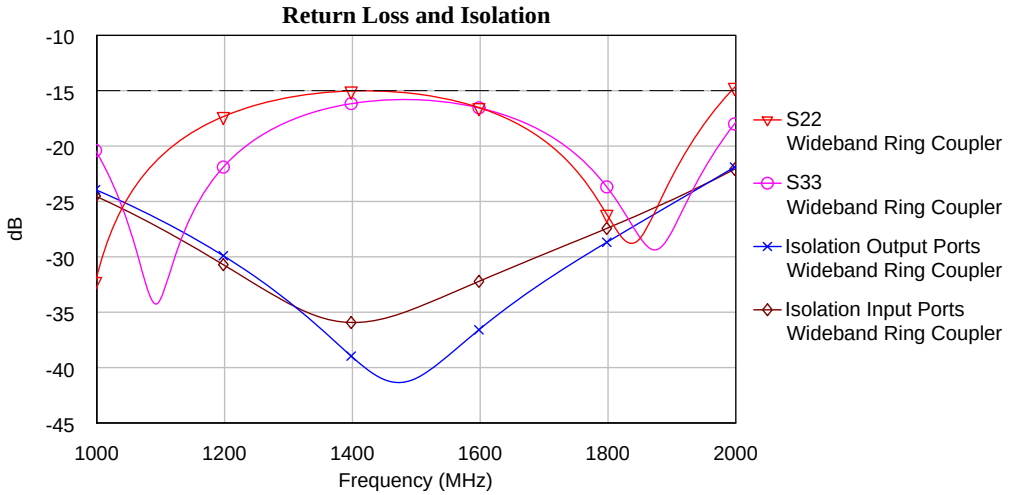

Figure 6.19: Simulated Return loss and Isolation of FGCPW Hybrid ring coupler.

Figure 6.19 indicates that the simulated return loss of the coupler is less than -15 dB, and the isolation between both the sum and difference output ports, as well as the two input ports, is less than -20 dB across the L-band.

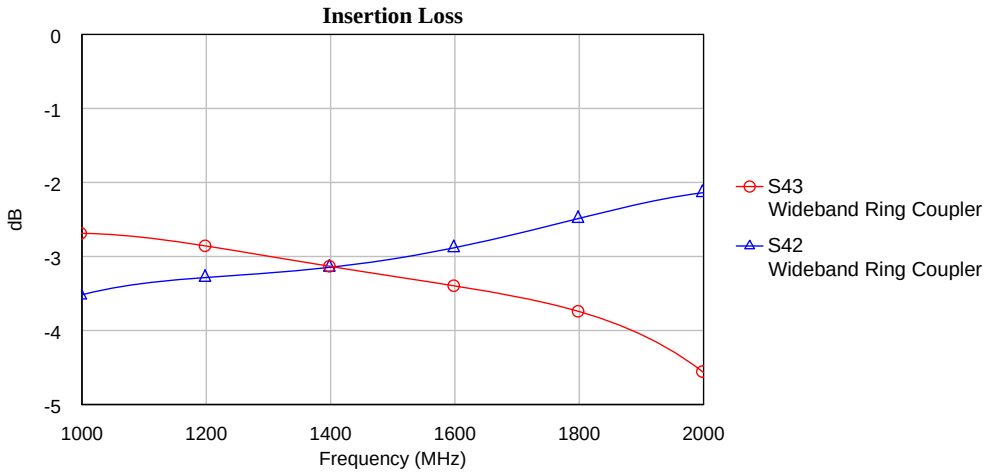

Figure 6.20: Insertion loss of Input Ports 2 and 3 simulated at Difference Port 4.

The insertion loss from each of the respective input ports to the difference port are compared in figure 6.20, indicating equal power division near the center of the L-band while deviating by less than 1 dB over the band of interest. Finally the graph in figure 6.21 shows the phase difference measured at the difference port between the two input ports.

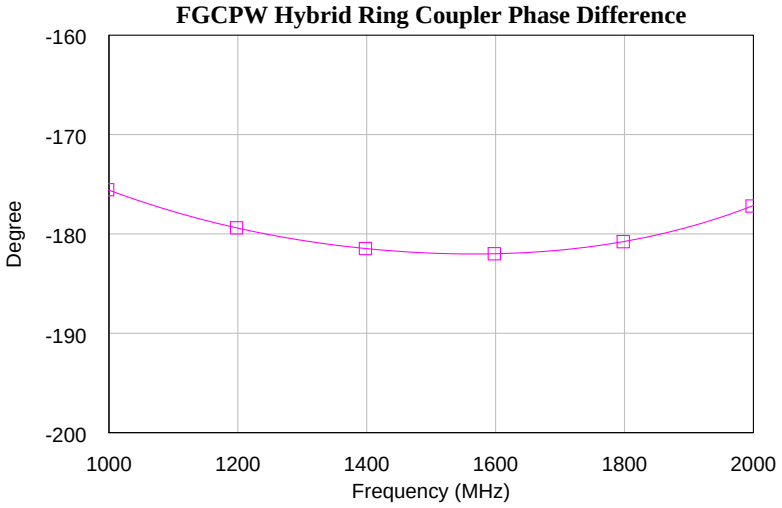

Figure 6.21: Simulated phase difference between Ports 2 and 3 for an excitation at Difference Port 4.

The simulated response indicates that the phase difference deviates from 180° by less than 5° across the band. Comparing this response to that of the narrowband design in section 6.1.1 the bandwidth of the FGCPW Hybrid ring coupler presented in this section is approximately 67% around the centre frequency, proving sufficient to the requirements of the dLNA operating bandwidth given in chapter 1.

6.2 Low Noise Amplifier Design

The differential LNA design consists of two single ended LNAs, configured in a balanced topology, feeding a 180°-Hybrid ring coupler as depicted in figure 6.22.

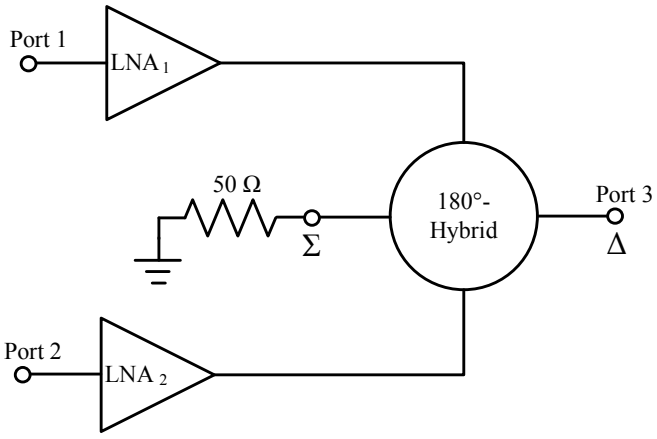

Figure 6.22: Schematic representation of the three-port differential LNA.

Two designs are discussed in this section. Both implement Hybrid coupler designs analogous to the design discussed in section 6.1.3.

6.2.1 Design 1: MAAL-010704

The first differential amplifier incorporates two unpaired LNAs manufactured by MA-COM - MAAL 010704. These LNAs require no external matching components and contains an integrated active biasing circuit allowing device biasing using a single external resistor.

6.2.1.1 Single ended LNA design

The circuit schematic of the single ended LNA design shown in figure 6.23.

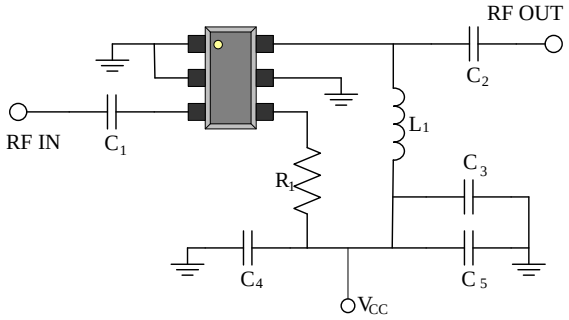

Figure 6.23: MAAL-010704 Single ended LNA circuit schematic.

Using the graph relating the biasing current I_{DQ} to the biasing resistor value in appendix D, the value of R_1 is chosen such that the biasing current ensures minimum noise contribution from the LNA.

Table 6.1 shows a summary of the components used in the single ended LNA design.

Table 6.1: Description of MAAL-010704 single ended LNA design components

Designator	Description	Purpose
R_1	390Ω 0603 resistor	Biasing resistor - ensures $I_D = 30mA$ for $V_{cc} = 3V$
L_1	82nH 0603 Inductor	RF Choke
C_1, C_2	1nF 0402 Capacitor	DC bolck
C_3	1nF 0402 Capacitor	Bypass Capacitor
C_5	10nF 0402 Capacitor	
C_4	1μF 0603 Capacitor	

To ensure device stability the LNA is implemented using grounded CPW transmission lines. Figure 6.24 shows the layout of the single ended LNA designed on Rogers 6010 RT/Duroid substrate.

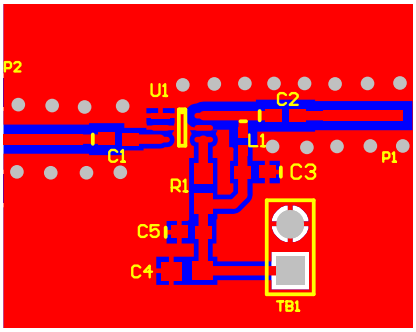

Figure 6.24: MAAL-010704 Single ended LNA layout.

Using the scattering and noise parameters supplied by MA-COM the layout in figure 6.24 is simulated in MWO. Figure 6.25 shows the simulated circuit realised with 50Ω CPW transmission line segments and the measured gain and reflection coefficients are compared to simulated results in the graphs in figure 6.26.

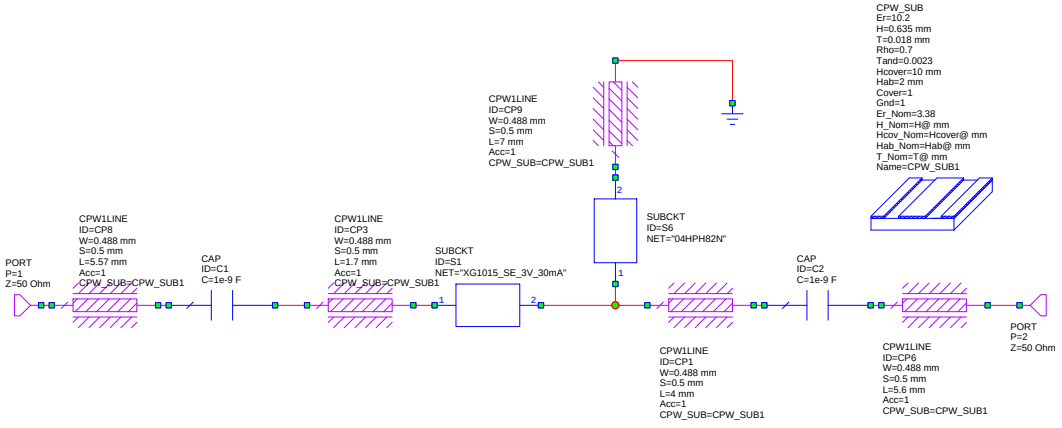

Figure 6.25: MAAL-010704 Single ended LNA layout simulated in MWO.

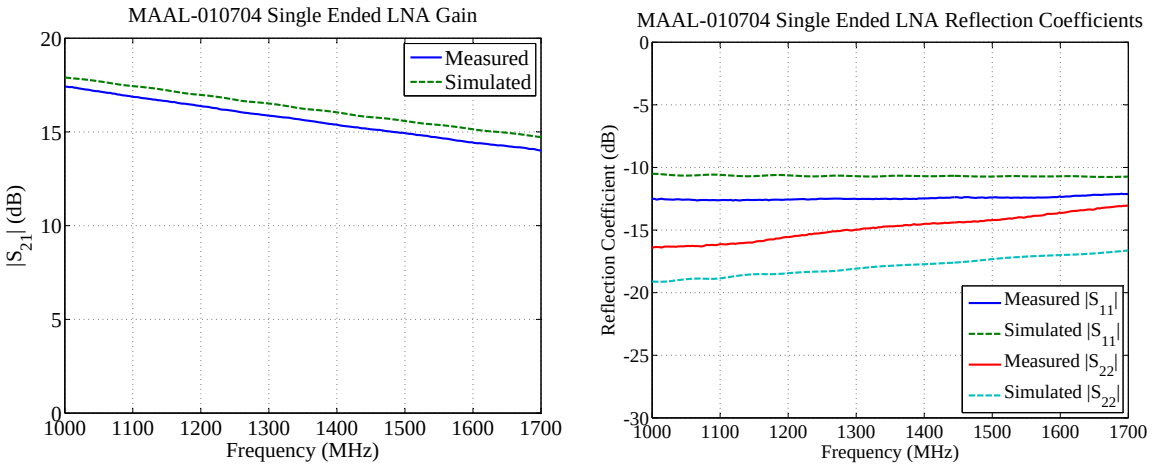

Figure 6.26: Simulated (a) Gain and (b) Reflection Coefficients of MAAL-010704 Single ended LNA.

Due to the low noise figure of the LNA, the noise figure is measured using the configuration depicted in figure 5.13. Figure 6.27 compares the measured narrowband noise figure to the simulated results.

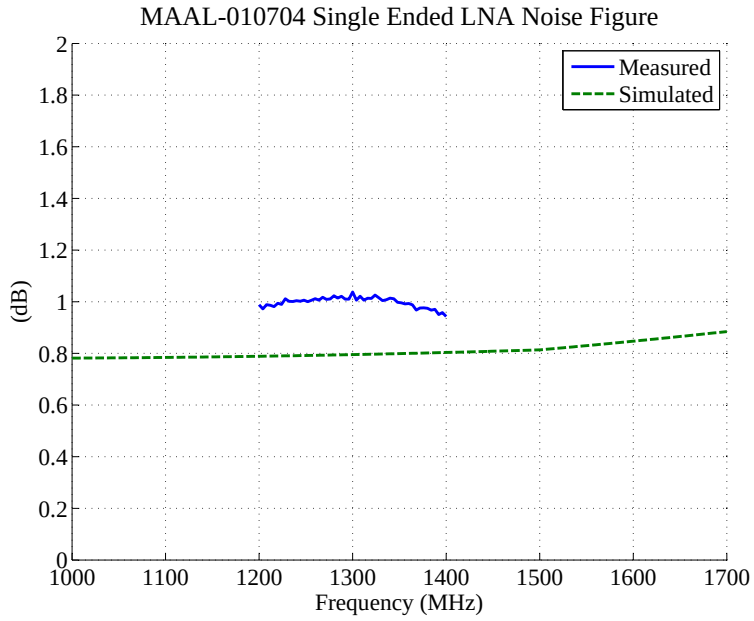

Figure 6.27: MAAL-010704 Single ended LNA noise figure.

The graph comparing the reflection coefficients in figure 6.26(b) indicates that the input and output match of the manufactured LNA differs slightly from that of the simulated circuit. The effect of this mismatch becomes apparent when considering the deviation in gain and noise figure illustrated in figures 6.26(a) and 6.27 respectively.

6.2.1.2 Differential LNA design

Realising the differential LNA requires the integration between a 180°-Hybrid coupler, similar to the structure described in section 6.1.3, and two of the single ended LNA designs outlined above. Since the LNAs are implemented with CPW transmission lines with a bottom ground plane and the Hybrid coupler is implemented in FGCPW that has no ground plane on the bottom layer of the substrate, a transition between the two types of transmission lines is required for the dLNA design. Using 50Ω transmission lines, this transition is investigated in CST. The simulated transition is shown in figure 6.28 and the Insertion Loss and Reflection coefficients are shown in figure 6.29.

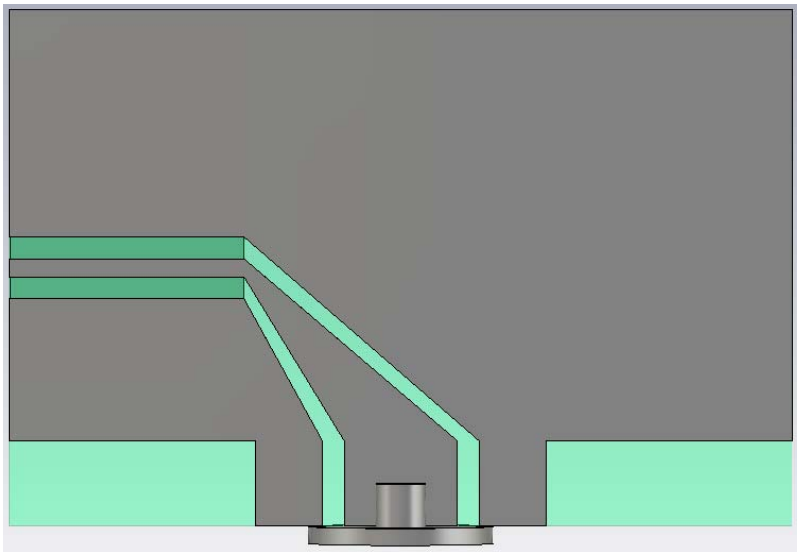

Figure 6.28: Transition between Coplanar Waveguide with bottom ground plane to Finite Ground Coplanar Waveguide without a bottom ground plane.

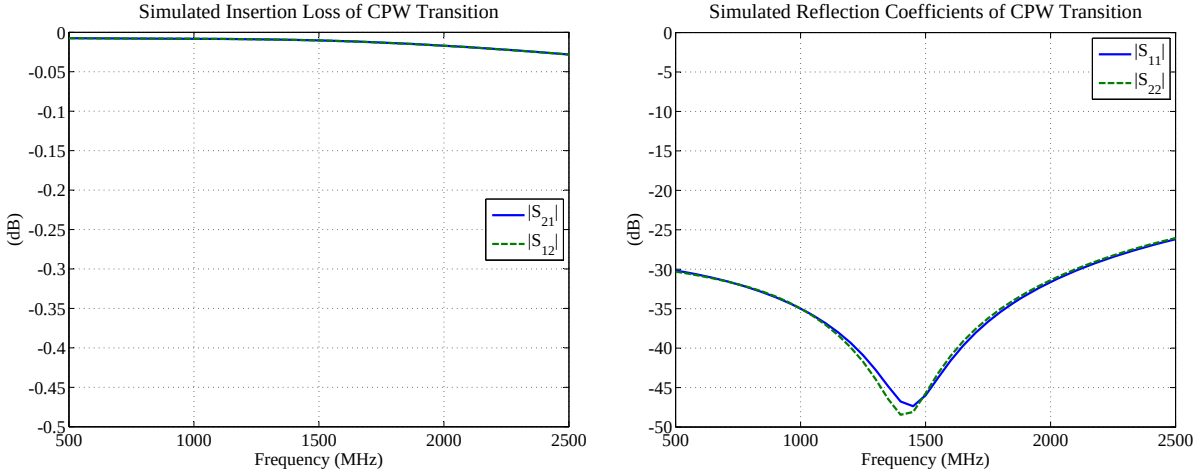

(a) (b)

Figure 6.29: Simulated (a) Insertion Loss and (b) Reflection Coefficients of CPW transition.

The dLNA design consisting of the two single ended LNAs connected to a 180°-Hybrid coupler through a CPW transition is shown in figure 6.30.

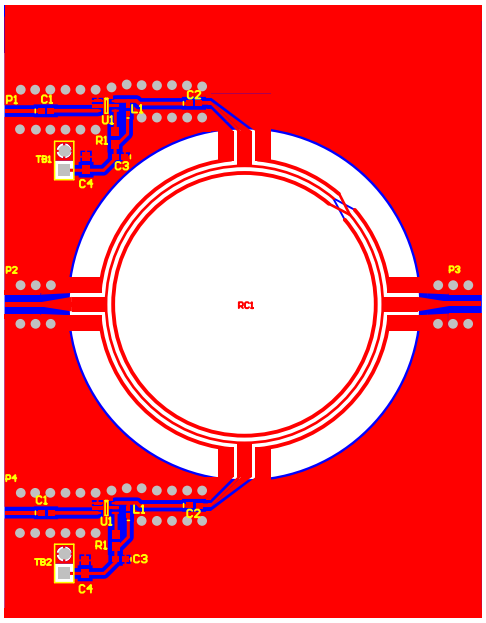

Figure 6.30: MAAL-010704 Differential LNA design layout.

6.2.1.3 Mixed-mode Signal Analysis

The theory on mixed mode S-parameters discussed in Chapter 4 can be applied to the three-port differential LNA to analyse the response of the circuit for differential and common-mode excitation. It follows from the relation in equation 4.3.32 that the mixed mode scattering matrix can be derived from the three-port scattering matrix using the transformation matrix **M**. Where, analogous to equation 4.3.30, the three-port transformation matrix equals

$$[\mathbf{M}] = \frac{1}{\sqrt{2}} \begin{bmatrix} 1 & -1 & 0 \\ 1 & 1 & 0 \\ 0 & 0 & \sqrt{2} \end{bmatrix} \tag{6.2.1}$$

Then, from equation 4.3.32

$$S_{s2d1} = \frac{1}{\sqrt{2}} (S_{31} - S_{32}) \tag{6.2.2}$$

$$S_{s2c1} = \frac{1}{\sqrt{2}} (S_{31} + S_{32}) \tag{6.2.3}$$

$$S_{d1d1} = \frac{1}{2} (S_{22} - S_{21} - S_{12} + S_{11}) \tag{6.2.4}$$

$$S_{c1c1} = \frac{1}{2} (S_{22} + S_{21} + S_{12} + S_{11}) \tag{6.2.5}$$

where the subscripts s, d, and c denote *single ended*, *differential mode*, and *common-mode* excitations. Equation 6.2.2 therefore equates the gain measured at the single ended output port due to a differential excitation applied to the differential input port - comprising of single ended ports 1 and 2.

Similarly equation 6.2.3 determines the gain measured at the single ended output for a common-mode excitation applied to the differential input port. With the values of the differential and common-mode gains known, the CMRR of the dLNA can be solved as the ratio

$$CMRR = \frac{S_{s2d1}}{S_{s2c1}} \tag{6.2.6}$$

Lastly equations 6.2.4 and 6.2.5 can be used to find the input reflection coefficient at the differential input port for a differential and common-mode excitation, respectively.

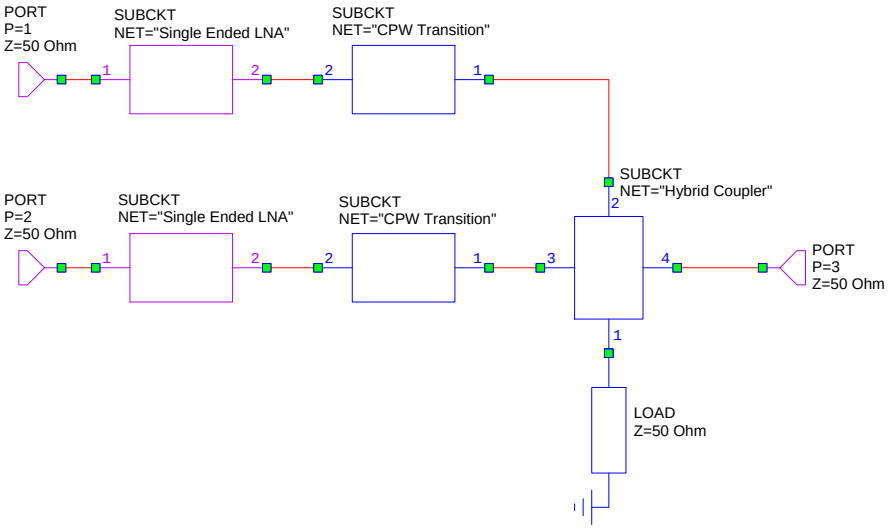

Figure 6.31: Three-port Differential LNA design simulated in MWO AWR using S-parameter and Noise parameter blocks.

Equations 6.2.2 to 6.2.6 can now be applied to the simulated and measured scattering parameters to analyse the mixed mode performance of the dLNA. The performance of the differential LNA design depicted in figure 6.30 is analysed in MWO using the simulated scattering and noise parameters of the single ended LNA design, the CPW transition and the Hybrid coupler design as shown in figure 6.31. Figure 6.32 shows two graphs comparing the measured and simulated gains and reflection coefficients of the MAAL-010704 differential LNA design.
When considering the measured gains of the dLNA, $|S_{31}|$ and $|S_{32}|$, it is apparent that the Hybrid coupler introduced an imbalance, in the gain amplitudes, of approximately 2dB at the higher end of the band - effectively reducing the differential gain of the dLNA. Furthermore, figure 6.32(b) indicates the degrading effect the reflection coefficient of the Hybrid coupler has on the input match of the single ended LNAs when comparing the measured input reflection coefficients of the dLNA to that of the single ended LNA.

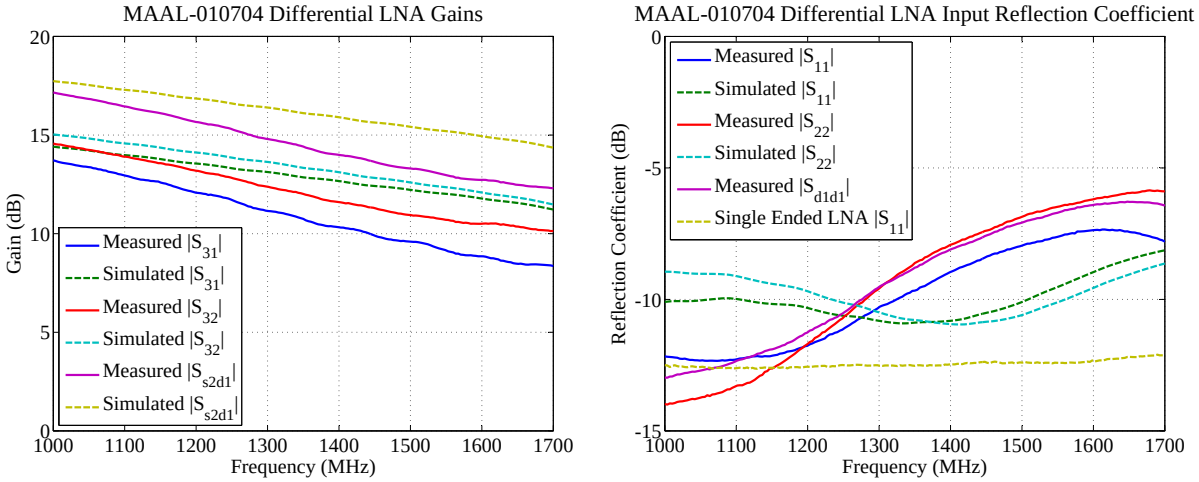

Figure 6.32: Simulated and measured (a) Gains and (b) Reflection Coefficients of the MAAL-010704 dLNA design.

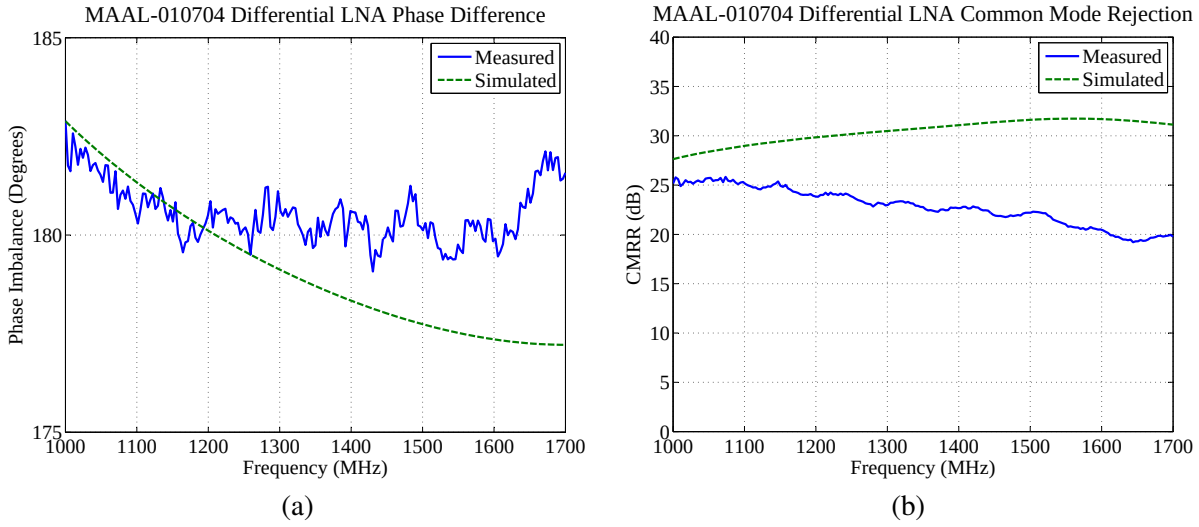

Figure 6.33: Simulated and measured (a) Phase imbalance and (b) CMRR of the MAAL-010704 dLNA design.

The phase imbalance and CMRR of the dLNA are shown in figure 6.33. The effect the deviation in insertion loss of the coupler has on the performance of the dLNA can clearly be seen in the graph comparing the simulated and measured CMRR, in figure 6.33(b). Even though the phase imbalance (figure 6.33(a)) varies by less than three degrees across the band, the amplitude imbalance should ideally be centred around 0 dB to ensure a high CMRR.

6.2.1.4 Mixed-mode Noise Analysis

Next consider the noise performance of the three-port dLNA. Chapter 3 discussed the derivation of the noise correlation matrix for a multi-port network. The theory on mixed mode propagation, introduced in chapter 4, can now be applied to the equivalent noisy three-port network shown in figure 6.34 to derive an expression for the differential noise figure.

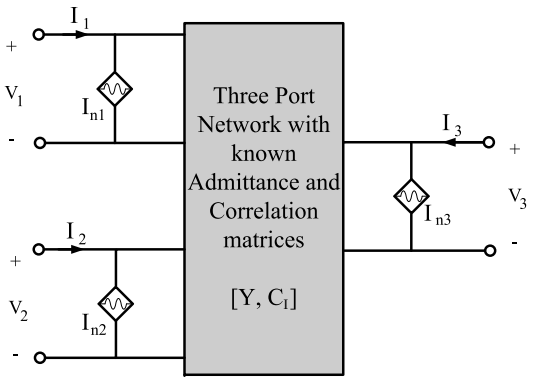

Figure 6.34: Noisy Three-port network.

Using the techniques described in section 3.4 the three-port network can can be represented by a (3 x 3) noiseless admittance matrix (Y) and noise current correlation matrix C_I. As described in chapter 4, the mixed mode voltages and currents of ports 1 and 2 are

$$V_d = V_1 - V_2 \tag{6.2.7}$$

$$V_c = \frac{1}{2}(V_1 + V_2) \tag{6.2.8}$$

$$I_d = \frac{1}{2}(I_1 - I_2) \tag{6.2.9}$$

$$I_c = I_1 + I_2 \tag{6.2.10}$$

where the subscripts d and c denote the differential and common modes, respectively.
Equations 6.2.7 to 6.2.10 can be used to relate the mixed mode port currents ($\mathbf{I}_{MM}$), port voltages ($\mathbf{V}_{MM}$), and noise currents ($\mathbf{i}_{mm}$) to the external port currents and voltages [5]:

$$\mathbf{I} = \mathbf{Y}\mathbf{V} + \mathbf{i}_n \tag{6.2.11}$$

$$\begin{bmatrix} I_1 \\ I_2 \\ I_3 \end{bmatrix} = \begin{bmatrix} Y_{11} & Y_{12} & Y_{13} \\ Y_{21} & Y_{22} & Y_{23} \\ Y_{31} & Y_{32} & Y_{33} \end{bmatrix} \begin{bmatrix} V_1 \\ V_2 \\ V_3 \end{bmatrix} + \begin{bmatrix} i_{n1} \\ i_{n2} \\ i_{n3} \end{bmatrix} \tag{6.2.12}$$

That is,

$$\mathbf{I}_{MM} = \mathbf{M}_I \mathbf{I} \tag{6.2.13}$$

$$\mathbf{V}_{MM} = \mathbf{M}_V \mathbf{V} \tag{6.2.14}$$

$$\mathbf{i}_{mm} = \mathbf{M}_I \mathbf{i}_n \tag{6.2.15}$$

where,

$$\mathbf{M}_I = \begin{bmatrix} \frac{1}{2} & -\frac{1}{2} & 0 \\ 1 & 1 & 0 \\ 0 & 0 & 1 \end{bmatrix} = \left(\mathbf{M}_V^{\dagger}\right)^{-1} \tag{6.2.16}$$

$$\mathbf{M}_V = \begin{bmatrix} 1 & -1 & 0 \\ \frac{1}{2} & \frac{1}{2} & 0 \\ 0 & 0 & 1 \end{bmatrix} = \left(\mathbf{M}_I^{\dagger}\right)^{-1} \tag{6.2.17}$$

Through some algebraic manipulation the following expressions are derived for the mixed-mode admittance and correlation matrices,

$$\mathbf{Y}_{MM} = \mathbf{M}_I \mathbf{Y} \mathbf{M}_I^{\dagger} \tag{6.2.18}$$

$$\mathbf{C}_{Y_{MM}} = \frac{< \mathbf{i}_{mm} \mathbf{i}_{mm}^{*} >}{2\Delta f} = \mathbf{M}_I \mathbf{C}_I \mathbf{M}_I^{\dagger} \tag{6.2.19}$$

Since the mixed-mode correlation matrix is of the form

$$\mathbf{C}_{Y_{MM}} = \frac{1}{2\Delta f} \begin{bmatrix} < i_d i_d^{*} > & < i_d i_c^{*} > & < i_d i_3^{*} > \\ < i_c i_d^{*} > & < i_c i_c^{*} > & < i_c i_3^{*} > \\ < i_3 i_d^{*} > & < i_3 i_c^{*} > & < i_3 i_3^{*} > \end{bmatrix} \tag{6.2.20}$$

the differential mode correlation matrix can be constructed such that

$$\mathbf{C}_{Y_d} = \frac{1}{2\Delta f} \begin{bmatrix} < i_d i_d^{*} > & < i_d i_3^{*} > \\ < i_3 i_d^{*} > & < i_3 i_3^{*} > \end{bmatrix} \tag{6.2.21}$$

Similarly, using the mixed mode admittance matrix ($\mathbf{Y}_{MM}$) the differential mode admittance matrix can be constructed

$$\mathbf{Y}_{MM_d} = \begin{bmatrix} Y_{MM_{dd}} & Y_{MM_{d3}} \\ Y_{MM_{3d}} & Y_{MM_{33}} \end{bmatrix} \tag{6.2.22}$$

Equations 6.2.21 and 6.2.22 defines the equivalent differential-mode two-port of the three-port network. The theory introduced in sections 3.1 and 3.2 can now be applied to transform the differential correlation matrix into its equivalent chain representation using the appropriate transformation matrix. That is,

$$\mathbf{C}_{C_d} = \mathbf{T} \mathbf{C}_{Y_d} \mathbf{T}^{\dagger} \tag{6.2.23}$$

$$\mathbf{T} = \begin{bmatrix} 0 & B_{MM} \\ 1 & D_{MM} \end{bmatrix} \tag{6.2.24}$$

The differential noise parameters of the three-port network (R_{N_d}, Y_{opt_d}, and F_{min_d}) can then be obtained using equations 3.3.14 to 3.3.16 and the differential noise figure of the network, when the network is driven by a source with a differential source admittance $Y_{S_d} = G_{S_d} + jB_{S_d}$, can be solved using

$$F_d = F_{min_d} + \frac{R_{N_d}}{G_{S_d}} |Y_{S_d} - Y_{opt_d}|^2 \tag{6.2.25}$$

Using MATLAB the differential noise figure of the dLNA design discussed in this section is calculated by implementing the mixed mode analysis outlined above for a differential source impedance of 100Ω. The graph in figure 6.35 compares the noise figure and minimum noise figure calculated in MATLAB to the values simulated using an ideal differential excitation in MWO.

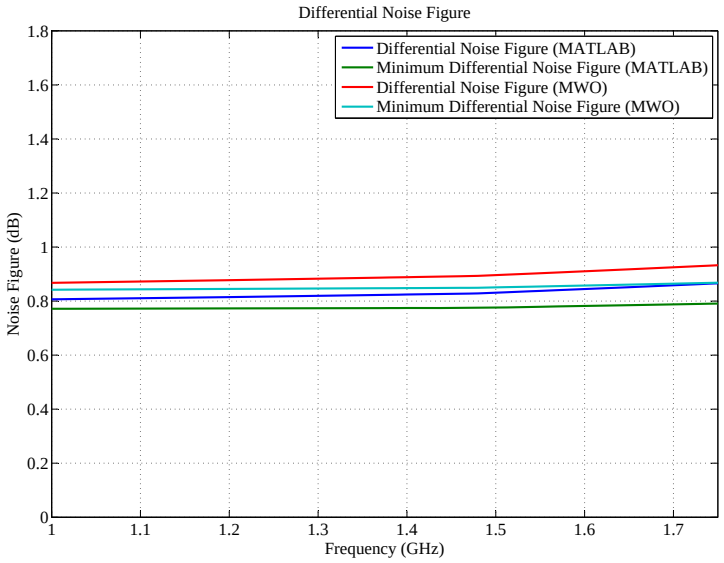

Figure 6.35: Differential noise figure and minimum differential noise figure calculated using mixed-mode analysis compared to simulated values.

Comparing the calculated differential noise figures to the simulated values indicates a discrepancy of approximately 0.1 dB between the values computed using the mixed-mode analysis and the simulated values. This deviation can be ascribed to the accumulation of small rounding errors that occur throughout the implementation of the algorithm. Despite this deviation, the computed analysis still indicate - in agreement to the simulated noise figure - that the dLNA design is well matched to a differential source impedance of 100Ω when considering the calculated and simulated differential noise figures individually compared to their respective minimum noise figures.

Finally the noise performance of the dLNA design is investigated using the de-embedding technique described in Chapter 5. The graph in figure 6.36(a) shows the single ended noise figure simulated when terminating each of the input ports alternately. Then using equation 5.3.10 the simulated and measured differential noise figure of the dLNA is de-embedded and compared to the noise figure of the constituent single ended LNA design in figure 6.36(b). This dLNA design illustrates the importance of symmetry in the Hybrid coupler design. To ensure that the signal performance of the differential LNA remains similar to that of the single ended LNAs it comprises of, the amplitude imbalance of the coupler should ideally be near 0 dB within the band of interest. Despite the deviation in the measured and simulated results, this design still verifies that the relation derived in equation 5.3.10 can be used to de-embed the differential noise figure by taking the gain deviation into account.

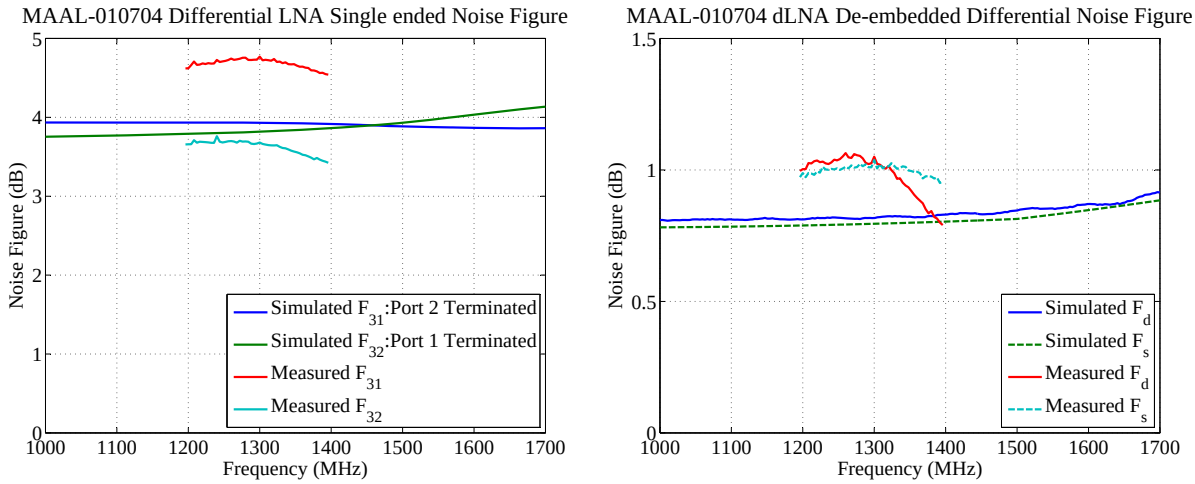

Figure 6.36: Simulated and measured (a) single ended and (b) de-embedded differential noise figure of the MAAL-010704 dLNA design.

6.2.2 Design 2: MGA-16516

Given the results of the first differential LNA discussed in section 6.2.1, the inverter of the Hybrid coupler implemented in the first dLNA has been altered to ensure improved amplitude imbalance. This involved reducing the size of the the inverter gap and also making use of vias and conductor on the bottom layer of the substrate to realise the inverter instead of lengthy bonding wires. The revised Hybrid coupler design is discussed in section 6.1.3 and is implemented in the second dLNA design discussed in this section. Implementing the dLNA using a balanced topology has the advantage of considering the design of the constituent single ended LNAs separately. Instead of using matched LNAs the transistors used for the single ended LNAs of this second dLNA design are a pair of matched GaAs Enhancement-mode pseudomorphic High Electron Mobility Transistors (pHEMTs) packaged in a 16-pin QFN package, manufactured by AVAGO Technologies: MGA-16516. During the design of LNAs there are a number of fundamental constraints that the design must adhere to in order to ensure the desired response, the first and most important of which is device stability.

6.2.3 Stability

A general two-port representation of an amplifier, defined by its S- and noise parameters, connected to a source impedance Z_S and terminated in a load impedance Z_L is shown in figure 6.37.

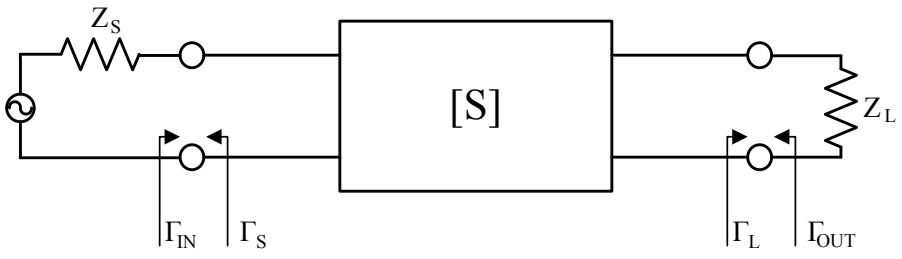

Figure 6.37: General representation of two-port amplifier network.

The gain of the two-port network can be described by three different definitions: Power Gain (G), Available Gain (G_A), and Transducer Gain (G_T). The Power Gain relates the power dissipated in the load to the power supplied to the input of the amplifier, and is therefore independent of the source impedance Z_S. The Available Gain is calculated as the ratio of the gain available at the output of the device to the power available from the source. Available gain is therefore only dependent on the source impedance. Lastly, the Transducer Gain is given by the ratio of the power dissipated in the load to the power available from the source. These gain definitions aid in optimising the source and load matching conditions during amplifier design and it follows that for conjugately matched two-port, $G = G_A = G_T$.

The input and output reflection coefficients can be solved in terms of the device S-parameters and the load and source reflection coefficients, respectively. That is,

$$\Gamma_{in} = S_{11} + \frac{S_{12}S_{21}\Gamma_L}{1 - S22\Gamma_L} \tag{6.2.26}$$

$$\Gamma_{out} = S_{22} + \frac{S_{12}S_{21}\Gamma_S}{1 - S11\Gamma_S} \tag{6.2.27}$$

where the source and load reflection coefficients are solved by

$$\Gamma_S = \frac{Z_S - Z_0}{Z_S + Z_0} \tag{6.2.28}$$

$$\Gamma_L = \frac{Z_L - Z_0}{Z_L + Z_0} \tag{6.2.29}$$

The amplifier network is considered unconditionally stable if $|\Gamma_{in}| < 1$ and $|\Gamma_{out}| < 1$ for all passive source and load impedances. If either $|\Gamma_{in}| > 1$ or $|\Gamma_{out}| > 1$ the network is considered conditionally stable and care should be taken to present the device with a source or load impedance that will ensure stable operation.

For the device to be unconditionally stable the following condition, referred to as the $\mu-$test, must be satisfied

$$\mu = \frac{1 - |S_{11}|^2}{|S_{22} - \Delta S_{11}^*| + |S_{12}S_{21}|} > 1 \tag{6.2.30}$$

This relation should hold over the full frequency range for which the device gain is greater than unity to ensure that the amplifier does not oscillate at a frequency outside of its operating bandwidth. If it is found that $\mu < 1$ over a range of frequencies, it is necessary to plot input and output stability circles in order to find the load and source impedance values that will ensure stable operation. Note that these stability circles only apply to a single frequency and therefore it may be necessary to plot a number of stability circles at intervals throughout the potentially unstable region.

Consider the input stability circle plotted in the Γ_S plane shown in figure 6.38.

The centre point and the radius of the stability circle are given by

$$C_S = \frac{(S_{11} - \Delta S_{22}^*)^*}{|S_{11}|^2 - |\Delta|^2} \tag{6.2.31}$$

$$R_S = \left| \frac{S_{12}S_{21}}{|S_{11}|^2 - |\Delta|^2} \right| \tag{6.2.32}$$

where Δ is defined as the determinant of the device scattering matrix

$$\Delta = S_{11}S_{22} - S12S_{21} \tag{6.2.33}$$

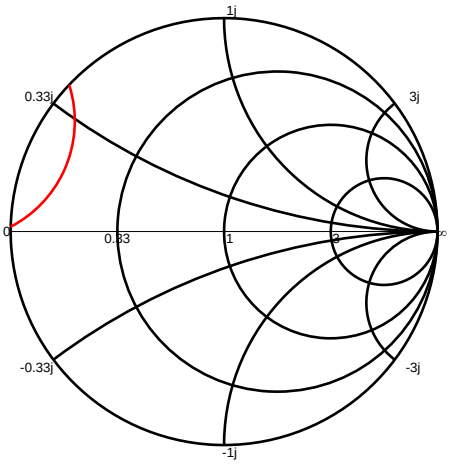

Figure 6.38: Input Stability circle plotted in Γ_S Plane.

It follows from equation 6.2.26 that, if $|S_{22}| < 1$ then $|\Gamma_{in}| < 1$ and hence that $\Gamma_S = 0$ - the centre of the Smith chart - indicates the stable region. Alternatively if $|S_{22}| > 1$, then $|\Gamma_{in}| > 1$ indicating that the region in which $\Gamma_S = 0$ indicates the unstable region and therefore the stable impedances are found in the region of the input stability circle that intersects the Smith chart.
Similarly the output stability circles can be plotted in the Γ_L plane with centre and radius calculated by

$$C_L = \frac{(S_{22} - \Delta S_{11}^*)^*}{|S_{22}|^2 - |\Delta|^2} \tag{6.2.34}$$

$$R_L = \left| \frac{S_{12}S_{21}}{|S_{22}|^2 - |\Delta|^2} \right| \tag{6.2.35}$$

with Δ as in equation 6.2.33. Analogous to the input stability circles the centre of the Smith chart is in the stable region for $|S_{11}| < 1$ and the region where the output stability circle intersects the Smith chart indicates the stable impedances for $|S_{11}| > 1$. Knowing the restrictions for the source and load impedance, if any, the amplifier can be designed to achieve the desired noise and power specifications.

6.2.4 Noise Performance

Unfortunately it is not possible to design an amplifier for both minimum noise and maximum gain, as there exists an optimum source reflection coefficient $\Gamma_S = \Gamma_{opt}$ that ensures minimum noise, which usually does not equal Γ_{in}^* that ensures optimum power match. Using constant gain and noise figure circles a compromise between noise performance and gain can be made. That is, using the device noise parameters F_{min}, Γ_{opt}, and R_n the center and radius of constant noise figure circles can be solved in the Γ_S plane, giving

$$C_F = \frac{\Gamma_{opt}}{N+1} \tag{6.2.36}$$

$$R_F = \frac{\sqrt{N(N+1-|\Gamma_{opt}|^2)}}{N+1} \tag{6.2.37}$$

where N is referred to as the noise figure parameter

$$N = \frac{F - F_{min}}{4R_n Y_0} |1 + \Gamma_{opt}|^2 \tag{6.2.38}$$

Consider the two-port network in figure 6.39, representing the amplifier connected in characteristic port impedances Z_0 through input and output matching networks.

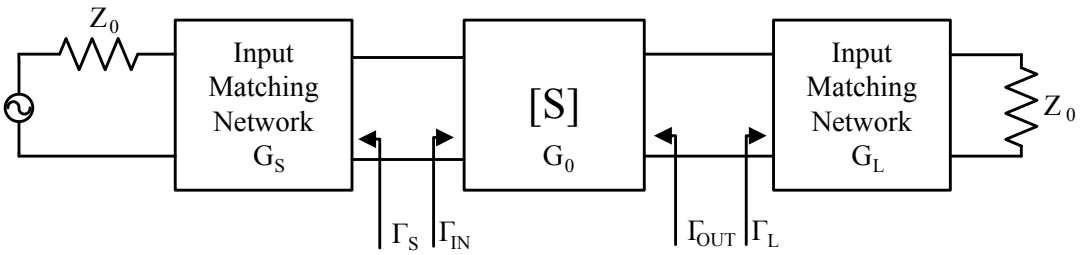

Figure 6.39: General two-port representation of amplifier with matching networks indicating the respective gain terms.

Assuming the device is unilateral ($S_{12} = 0$), the transducer gain can be solved in terms of gain factors

$$G_T = G_S G_0 G_L \tag{6.2.39}$$

where G_S and G_L are the effective gain factors for the source and load matching networks, respectively and G_0 is the gain factor of the transistor itself, given by

$$G_S = \frac{1 - |\Gamma_S|^2}{|1 - S_{11}\Gamma_S|^2} \tag{6.2.40}$$

$$G_0 = |S_{21}|^2 \tag{6.2.41}$$

$$G_L = \frac{1 - |\Gamma_L|^2}{|1 - S_{22}\Gamma_L|^2} \tag{6.2.42}$$

The source and load gain factors are maximised for $\Gamma_S = S_{11}^*$ and $\Gamma_L = S_{22}^*$. That is,

$$G_{S_{max}} = \frac{1}{1 - |S_{11}|^2} \tag{6.2.43}$$

$$G_{L_{max}} = \frac{1}{1 - |S_{22}|^2} \tag{6.2.44}$$

Using the Smith chart contours of constant source gain factor values can be plotted, with constant noise figure circles, in the Γ_S plane. The centre and radius of the constant gain circles can be solved for different gain values using

$$C_{G_S} = \frac{g_s S_{11}^*}{1 - (g_s)|S_{11}|^2} \tag{6.2.45}$$

$$R_{G_S} = \frac{\sqrt{1 - g_s}(1 - |S_{11}|^2)}{1 - (g_s)|S_{11}|^2} \tag{6.2.46}$$

where g_s is defined as the normalised gain factor

$$g_s = \frac{G_S}{G_{S_{max}}} \tag{6.2.47}$$

Thus by choosing values of constant noise figure F in equation 6.2.38 and constant source gain factor G_S in equation 6.2.47, noise figure and gain circles can be plotted in the Γ_S plane as shown in figure 6.40.
Using these circles a compromise can easily be found between gain and noise, by finding the value of the source reflection coefficient at a point of intersect between a noise figure circle and gain circle that adheres to the design specifications.

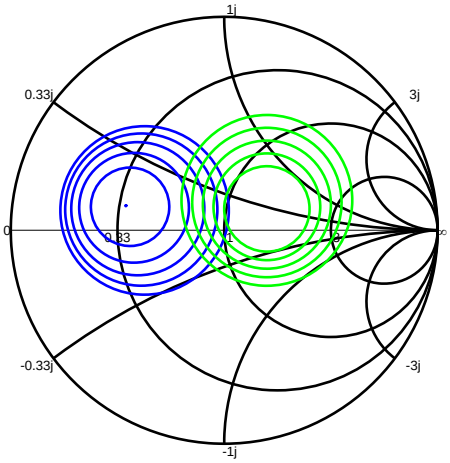

Figure 6.40: Constant Noise Figure (blue) and Gain (green) circles plotted in the Γ_S plane.

6.2.5 Single ended LNA Design

Consider the expression for the output reflection coefficient in equation 6.2.27. It follows that a change in source reflection coefficient influences the value of the load reflection required for optimum power match. It can easily become quite an iterative procedure to find the ideal noise, as well as input and output power match. Fortunately software packages such as MWO AWR allows for the use of TOUCHSTONE files: a text file containing device electrical and noise parameters over a range of frequencies. The design methodology of a single ended LNA in MWO AWR is outlined in this section. Since low noise performance is the primary concern of the amplifier design, the device biasing is chosen such that the minimum noise performance is achieved. According to the MGA-16516 datasheet, the noise contributed by the transistor is at its lowest for a Drain voltage $V_{DD} = 5$V, a Drain current $I_D = 50$mA, and in order to achieve the desired Drain current, a Gate-Source voltage $V_{GS} = 0.57$V is required. The biasing circuit for the LNA, shown in figure 6.41, is designed to meet these specifications.

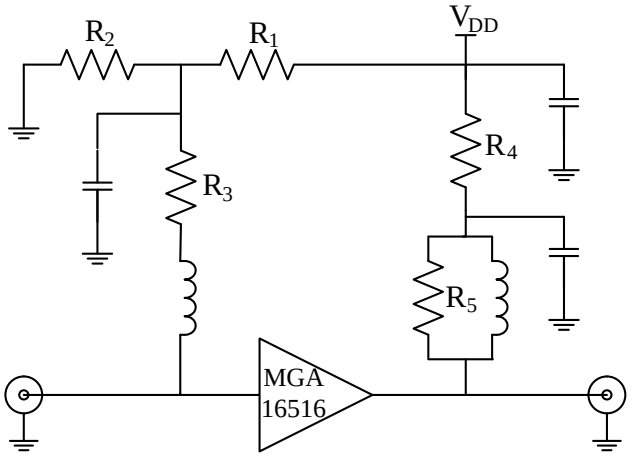

Figure 6.41: Single ended LNA biasing circuit schematic.

Note that only resistors R_1 and R_2 form part of the biasing circuit, whereas resistors R_3, R_4 and R_5 are loading resistors that ensure unconditional stability in the low and high frequency range. The graph in figure 6.42 clearly indicates the effect these loading resistors have on the stability of the network.

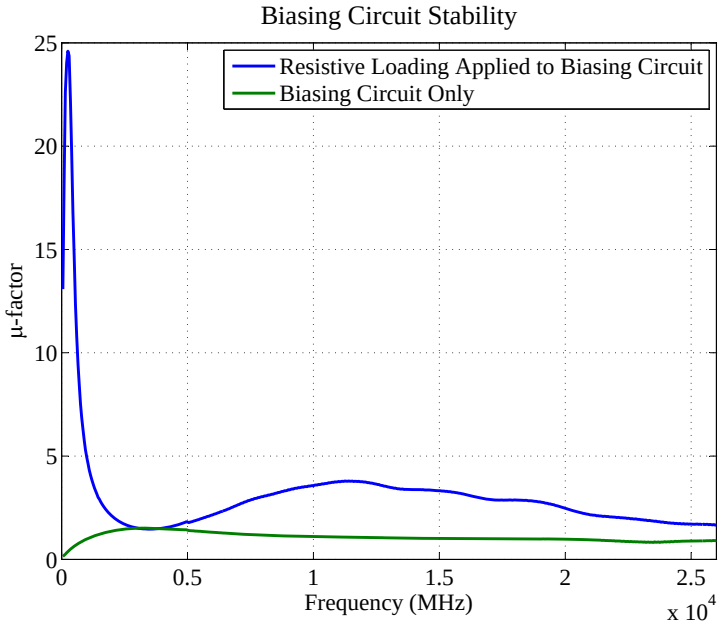

Figure 6.42: Effect of loading resistors on device stability.

With the biasing circuit being unconditionally stable the input and output matching networks can be designed for optimum noise match and maximum available gain, respectively. These matching networks can easily be synthesised using the ideal lossless impedance tuning element available in MWO. Figure 6.43 shows the two-port network of the biasing network connected to two lossless impedance tuners.

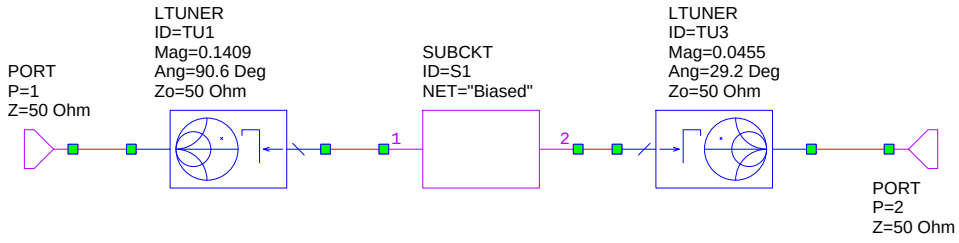

Figure 6.43: Ideal impedance tuners connected to the Biasing circuit used to determine optimum noise and power match.

First consider the output matching network. The amplifier can be matched to ensure maximum available gain by only tuning the impedance of the output matching element such that the simulated gain S_{21} equals the available gain G_A. Thereafter, the input matching network can be tuned to find the impedance match for which the noise figure of the network equals the minimum noise figure at the desired frequency. Using these impedance values, the input and output matching networks can be synthesised with ideal lumped elements as indicated in figure 6.44.

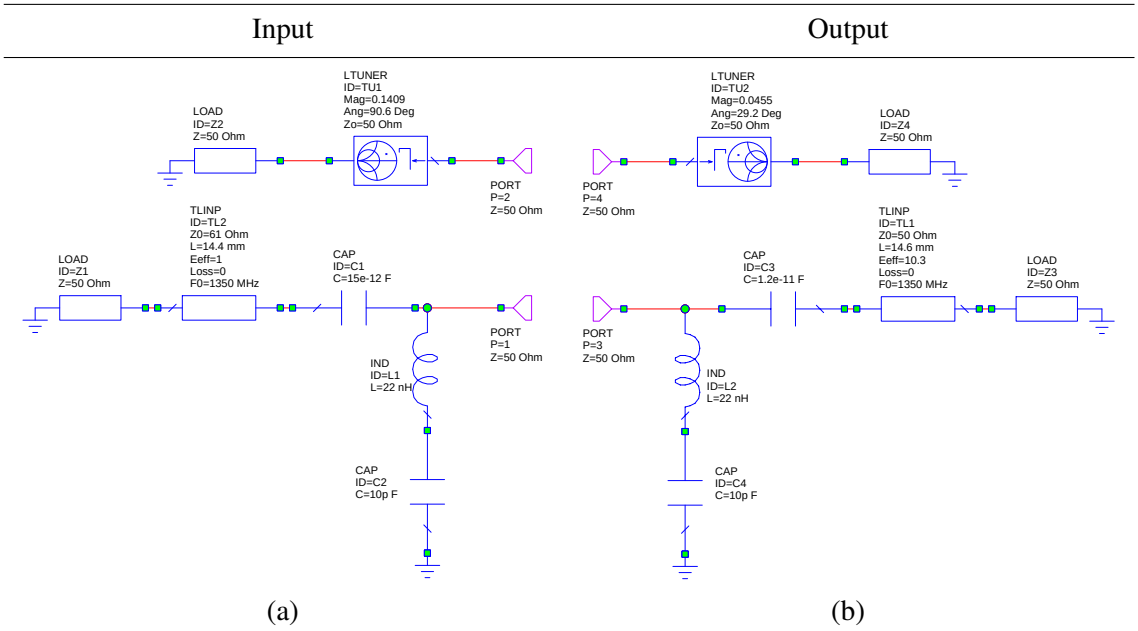

Figure 6.44: Synthesised Input (a) and Output (b) lumped element matching networks.

A schematic of the LNA circuit including the biasing and matching networks is shown in figure 6.45 and a summary of the components is given in table 6.2.

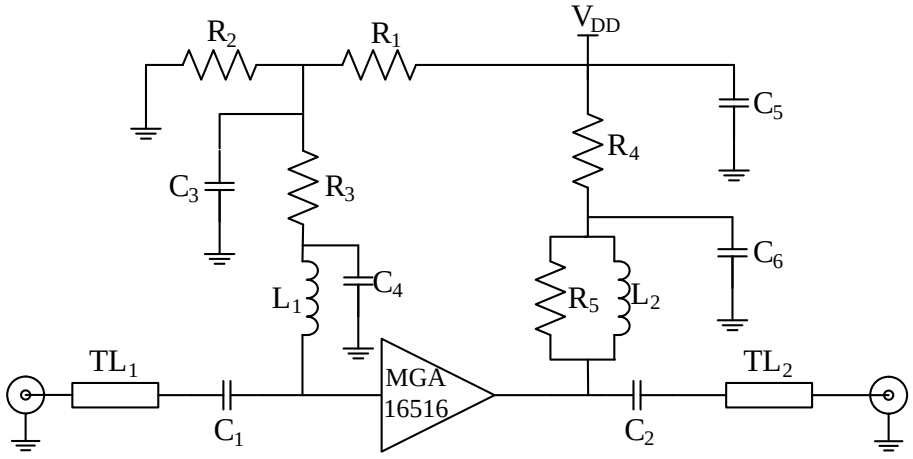

Figure 6.45: Circuit Schematic of the single ended LNA design.

The LNA is realised using SMD components on 0.635mm thick Rogers RT/Duroid 6010 high frequency laminate with half once copper cladding and all the transmission lines are implemented in CPW as indicated in the PCB layout of the LNA in figure 6.46. Table 6.2 gives a summary of the components implemented in the LNA design.

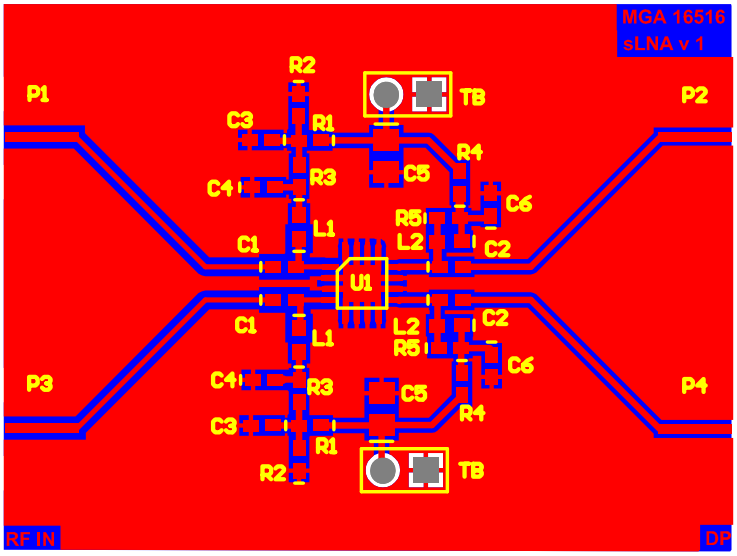

Figure 6.46: Layout of two matched single ended LNAs.

Table 6.2: Description of single ended LNA components

Designator	Description	Purpose
R_1	$10k\Omega$ 0402 resistor	Voltage divider for Gate biasing voltage
R_2	$1k3\Omega$ 0402 resistor	
R_3, R_4	10Ω 0402 resistor	Loading resistor for Low frequency stability
R_5	100Ω 0402 resistor	Loading resistor for High frequency stability
L_1, L_2	22nH 0603 Inductor	Input and Output Matching, RF Choke
C_1	15pF 0402 Capacitor	Input Matching, DC bolck
C_2	12pF 0402 Capacitor	Output Matching, DC block
C_3	10nF 0402 Capacitor	Bypass Capacitor
$C_{4,6}$	10pF 0402 Capacitor	
C_5	1μF 0402 Capacitor	
TL_1	14.4mm 61Ω CPW Transmission line	Input Matching, RF-input connection
TL_2	14.6mm 50Ω CPW Transmission line	RF-Output connection

To analyse the layout in figure 6.46 the circuit is simulated in MWO using coplanar EM-Quasi Static transmission line elements as well as measured S-parameter models for each of the lumped elements implemented in the design. The simulated circuit schematic of the final LNA layout is shown in figure 6.49, and the graphs in figures 6.47(a), 6.47(b) and 6.48 compare the measured Gain, Input and Output Reflection Coefficients as well as the noise figure - measured using the setup depicted in figure 5.13 - of the LNA to that of the circuit simulated in MWO.

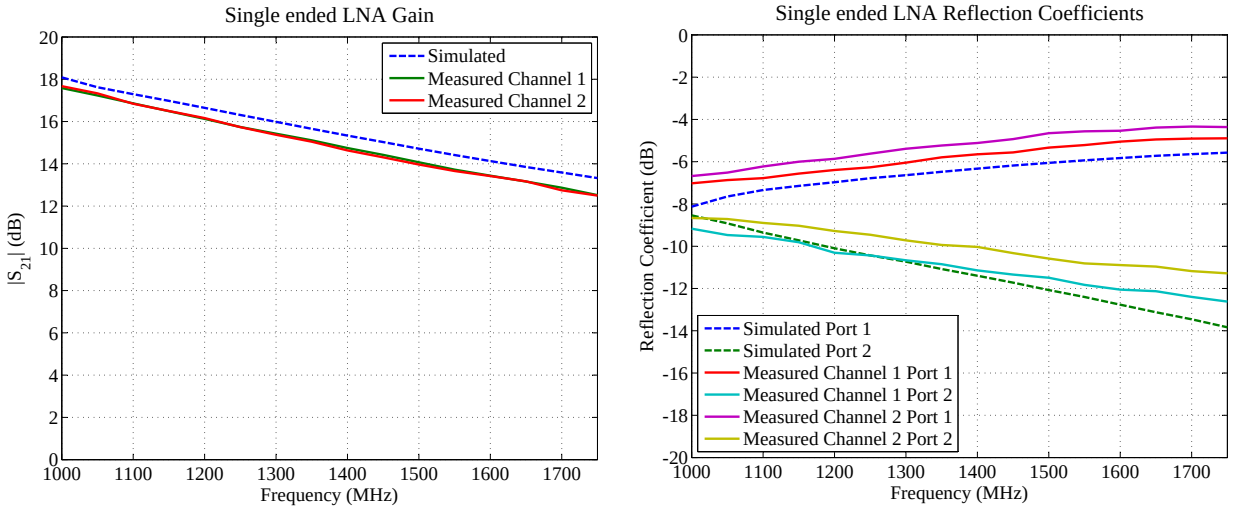

Figure 6.47: Measured and simulated (a) Gain and (b) Input and Output Reflection Coefficients of the MGA-16516 single ended LNA.

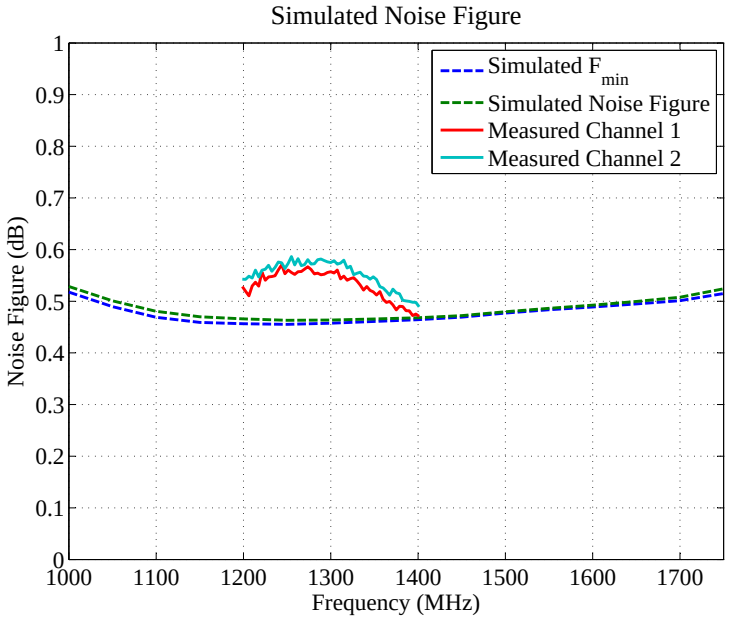

Figure 6.48: Simulated and measured noise figure of single ended LNAs.

6.2.6 Differential Low Noise Amplifier Design

The graphs in figures to 6.47 and 6.48 indicate that the measured results of the single ended LNA conform well to the simulated results and that the response of the two channels, especially the gains and noise figures, of the paired LNAs are very similar. The major discrepancies from the simulated response can be ascribed to the fact that the Drain current of the manufactured LNA is slightly less than the 50mA it was designed for. As discussed in Chapter 5, equal gain and noise performance of the two LNAs are the critical requirements for the dLNA design and therefore the measured results indicate that the single ended LNA design can be implemented in the differential design.

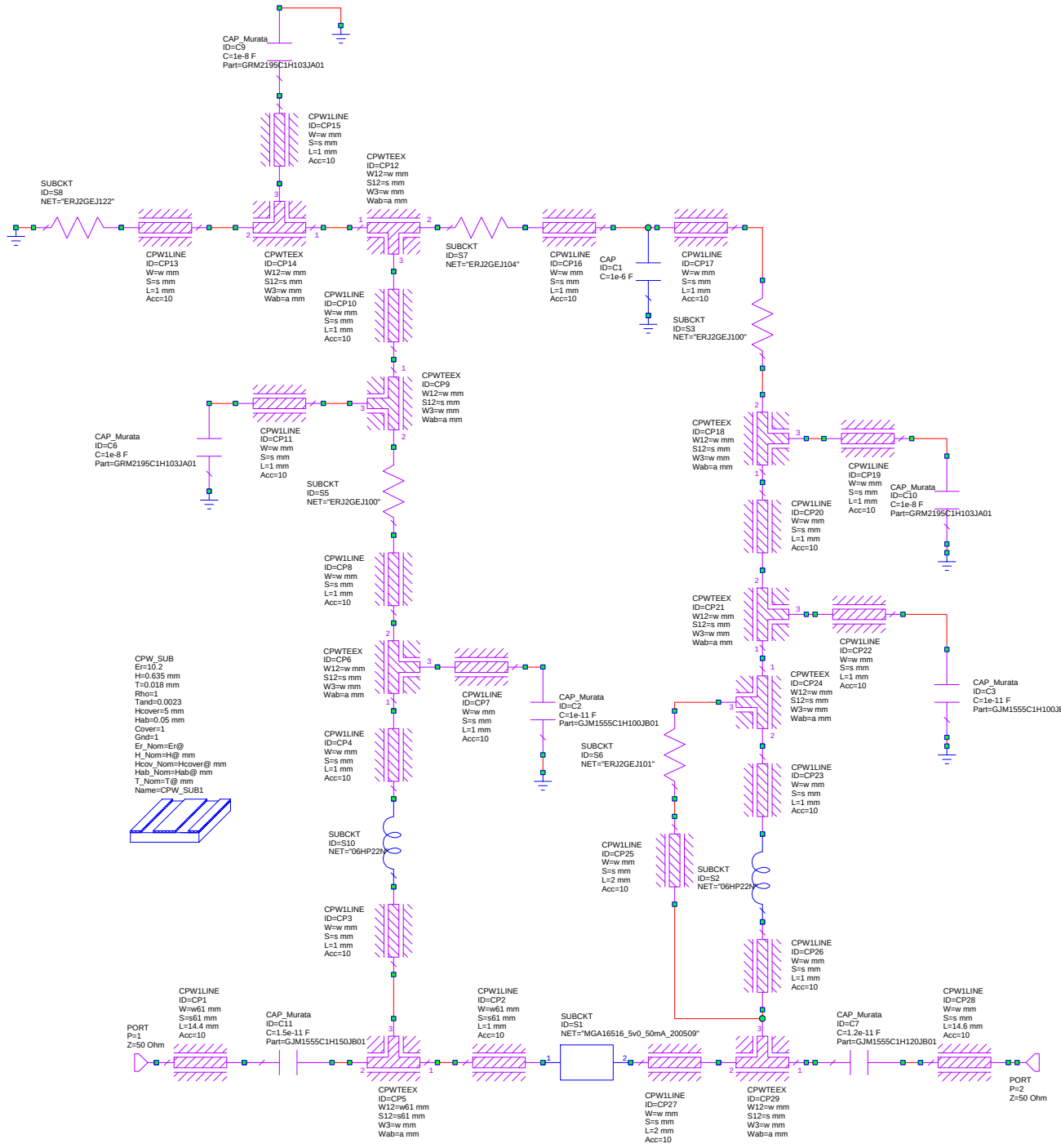

Figure 6.49: Single ended LNA coplanar layout simulated in MWO.

The differential LNA design layout consisting of the matched single ended LNAs connected to the 180°-Hybrid coupler through a CPW transition, analogous to the transition implemented in the first dLNA design, is shown in figure 6.50.

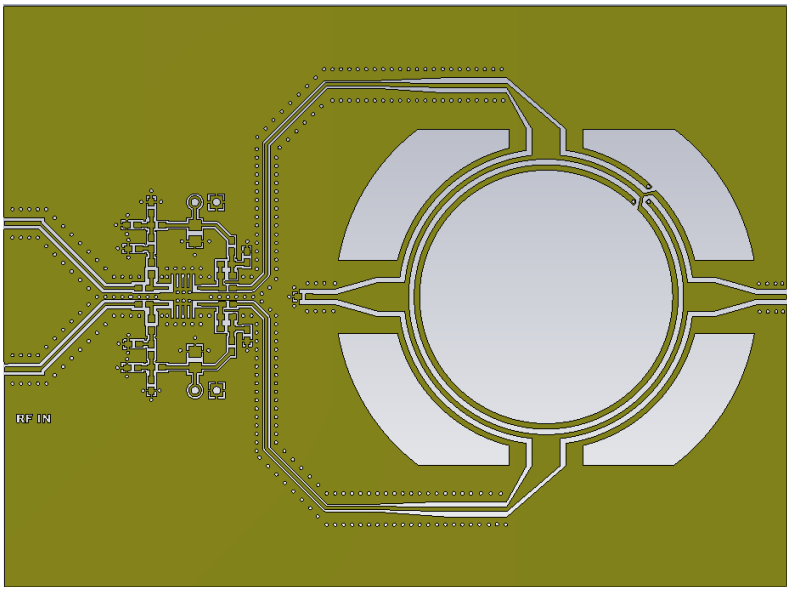

Figure 6.50: PCB layout of Differential Low Noise Amplifier.

Using the simulated S-parameters of the 180°-Hybrid coupler and the CPW transition the response of the differential LNA is analysed in MWO AWR. The simulated schematic network is similar to the schematic used for the first dLNA design shown in figure 6.31, where the 'Single Ended LNA' two-port network contains the S- and noise parameters of the single ended LNA design depicted in figure 6.49. Note that the length of the output transmission line segment has been extended to 50.4mm to correspond to the layout depicted in figure 6.50.

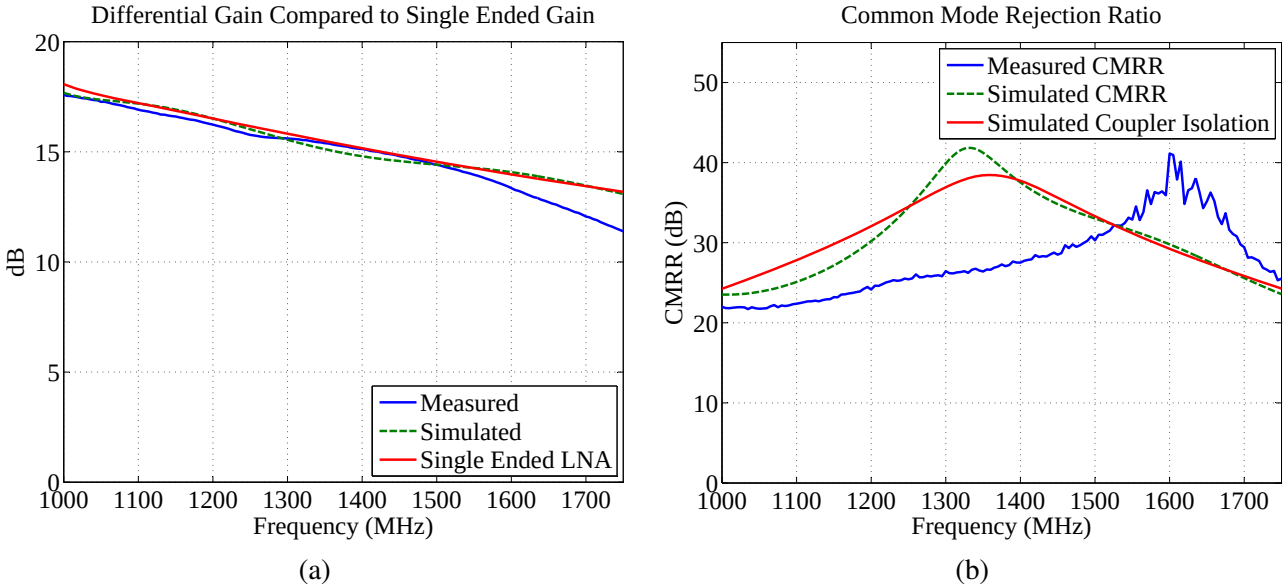

Figure 6.51: Measured and simulated (a) Gains and (b) CMRR of the MGA-16516 differential LNA.

Applying equations 6.2.2 to 6.2.6 to the scattering parameters of the measured and simulated three-port differential LNA, the mixed-mode performance of the dLNA can be investigated. Starting with the device gain, the graph in figure 6.51(a) shows the simulated and measured differential gains as calculated using equation 6.2.2, and compares these gain values to that of the single ended LNA design. The graph indicates that although there is approximately a 3 dB loss in gain along each of the respective signal paths, when considering a differential excitation the differential gain of the dLNA nearly equals that of its constituent single ended LNAs.
The simulated and measured CMRR of the dLNA is compared in the graph in figure 6.51(b). Included in the graph is the isolation between the sum and difference ports of the 180°-Hybrid coupler and comparing the simulated isolation of the coupler to the CMRR clearly indicates that the isolation of the coupler determines the CMRR of this dLNA design topology.

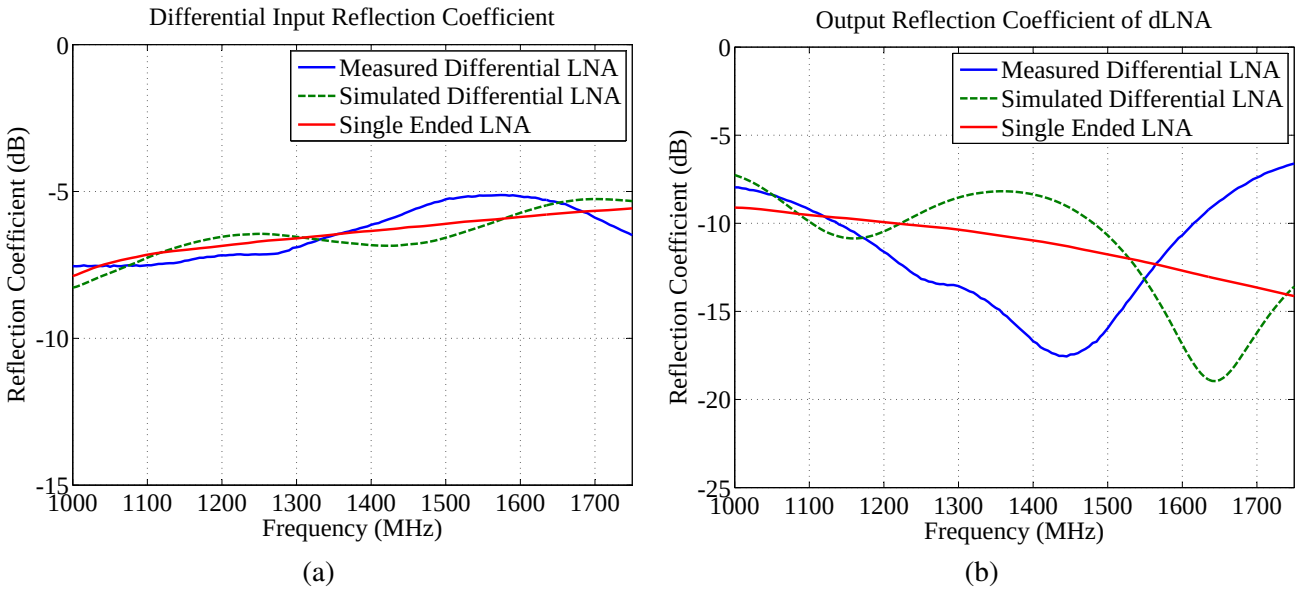

Figure 6.52: Simulated (a) Input and (b) Output Reflection Coefficients of Differential LNA.

Figure 6.52 shows the simulated and measured differential input reflection coefficients as well as the reflection coefficient simulated at the single ended output port. The graph shows that the input reflection for a differential input port is similar to that of each of the constituent single ended input ports. Furthermore, it can be seen that the cascaded connection of the 180°-Hybrid coupler with the single ended LNA causes a slight degradation in the output reflection of the dLNA when comparing it to that of the single ended LNA.
The amplitude and phase difference between the signals along the two respective signal paths is shown in the graph in figure 6.53. As expected from the simulated response of the 180°-Hybrid coupler, figures 6.20 and 6.21, the amplitude of the gains along the two signal paths of the dLNA differ by less than 1 dB, and the phase difference deviates from 180° by less than 5° across the band.

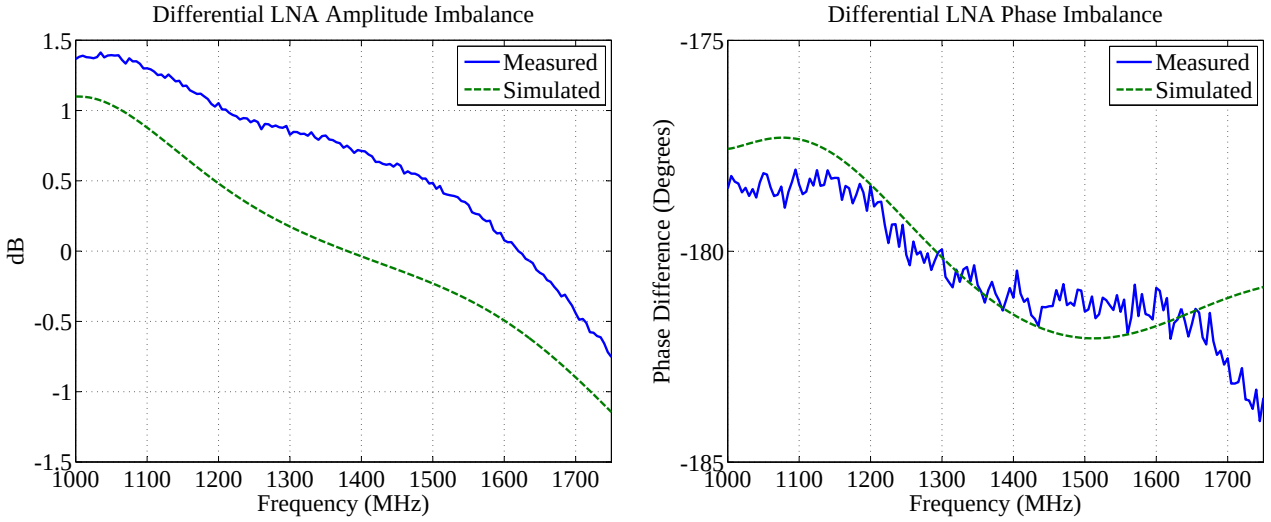

Figure 6.53: Simulated and measured (a) Amplitude and (b) Phase Imbalance of Differential LNA.

Lastly, using the de-embedding technique described in chapter 5 the noise performance of the dLNA design is investigated. The graph in figure 6.54 shows the simulated and measured single ended noise figure determined by terminating each of the input ports alternately. The simulated and measured differential noise figure de-embedded using equation 5.3.10 are compared to the simulated and measured noise figure of the constituent single ended LNA design in figure 6.55.

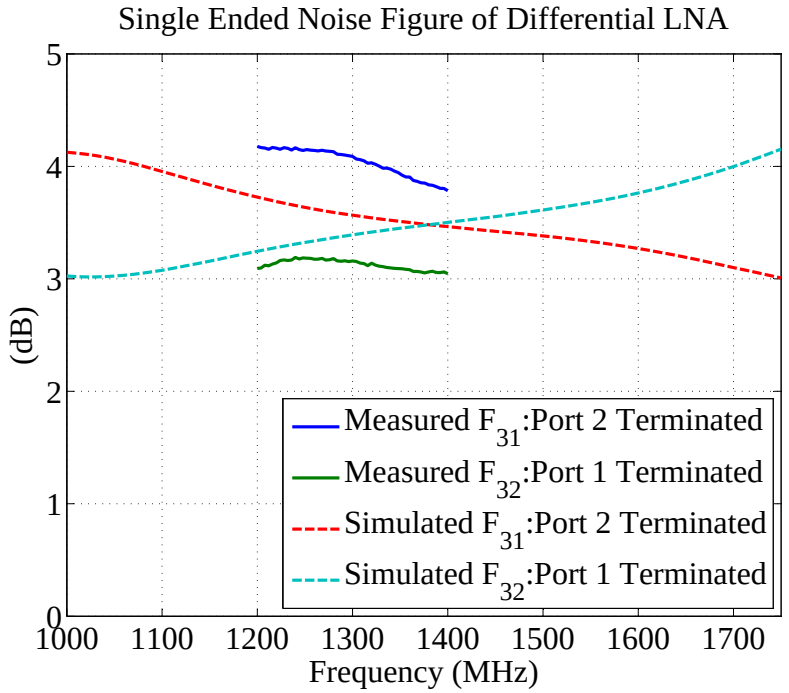

Figure 6.54: Simulated Single Ended Noise Figure of Differential LNA.

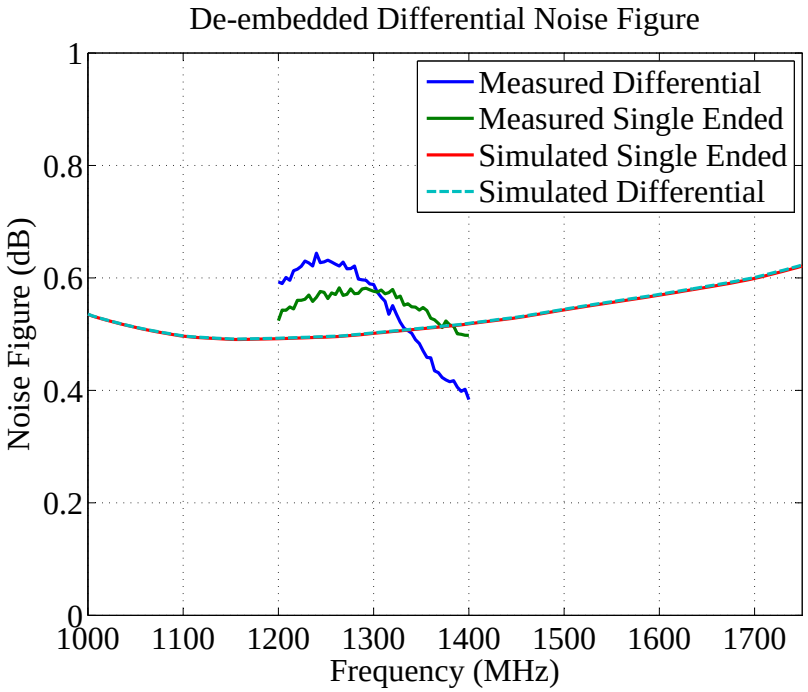

Figure 6.55: De-embedded Differential Noise Figure compared to the Noise Figure of the Single Ended LNA.

6.3 Conclusion

This chapter discussed the various aspects of the differential LNA designed in order to verify the method, introduced in Chapter 5, on de-embedding the differential noise figure from single ended measurements. The design implements a balanced amplifier topology feeding a 180°-Hybrid Ring Coupler and the fundamental theory on LNA design as well as novel techniques on reducing the size of Hybrid couplers and increasing their operating bandwidth is discussed. Software packages such as CST and MWO are used to investigate the response of the wideband Hybrid coupler design, the paired single ended LNA design, as well as the integration of CPW transmission lines with bottom ground plane with FGCPW transmission lines with no bottom ground. Using the simulated S-parameters of the Hybrid Ring Coupler and the CPW to FGCPW transition, the response of the dLNA is analysed in MWO. The mixed-mode S-parameters, introduced in Chapter 4, of the dLNA are investigated, indicating that - provided that the insertion loss along the two differential signal paths of the Hybrid coupler are sufficiently equal - the gain of the differential LNA is very similar to that of its constituent single ended LNAs when considering a differential input port . Furthermore, the mixed-mode analysis is used to quantify the common-mode suppression introduced by the Hybrid coupler. Lastly the differential noise figure determined from two single ended noise figure measurements, using the techniques discussed in Chapter 5, is shown to equal the noise figure of its constituent single ended LNAs.

Chapter 7

Conclusion

As stated in the introduction, the characterisation of differential Low Noise Amplifiers (LNAs) is not a trivial task. This thesis aimed to provide the reader with the necessary background regarding the noise performance of microwave circuits. This entailed a brief history of the discovery of noise in electronic circuits and a detailed description of the physical origin of the two predominant sources of noise namely Shot Noise and Thermal Noise. Knowing the physical origin of these sources of noise, the familiar equivalent small signal models of two widely used active devices - Bipolar Junction Transistors (BJTs) and FET - were adapted to include their associated noise generators. Various authors have published work on the noise and signal performance of these equivalent noise models, each ascribing unique noise generators to the existing small signal models. Chapter 2 introduced two noise models for BJTs, one considering correlated noise sources in section 2.3.2.2 and another assuming uncorrelated noise generators in section 2.3.2.1. These models were compared to one another and the effect of neglecting the correlation between sources was made clear. Noise models developed for Field Effect Transistors (FETs) were introduced and the model proposed by Pospieszalski was validated in section 2.4.2. Including the noise generators in equivalent small signal models can quickly complicate the analysis of even the simplest circuits. Therefore methods were introduced by which two-port devices can be represented by a noiseless two-port network with two equivalent noise generators connected to the external ports. By representing a noisy two-port in this manner the noise and signal performance of the two-port network can be described by an equivalent electrical matrix and its corresponding noise matrix, referred to as the correlation matrix, introduced in chapter 3. Correlation matrices for three of the most common two-port electrical representations were introduced, namely the Admittance, Impedance and Chain representations and the methods for transforming between various representation were discussed - significantly simplifying two-port noise analysis. The real importance of the correlation matrix was made clear by the elegant relationship derived between the chain representation and the noise parameters of a linear two-port device. This relation together with the transformation matrices provided the means by which the noise performance of multi-port networks could be derived. Chapter 4 introduced the concept of differential and common-mode signals, referred to as mixed-mode signals, that can propagate in multi-port networks. Using the analysis of coupled transmission lines a simple relation between the mixed-mode and general scattering parameters was derived. It was later shown that the same analysis applies to the noise within multi-port networks, when the mixed-mode correlation matrix was derived in section 6.2.1 making it possible to completely characterise the noise and signal performance of differential microwave networks.

Chapter 5 introduced a number of noise figure measurement techniques for both two-port and differential devices and investigated the effect various proposed measurement improvement techniques have on the calibration of an N8975A NFA when using a high ENR noise source. This investigation illustrated the uncertainty any mismatch between the noise source and DUT, or the DUT and the NFA, can introduce when performing low noise figure measurements and it was shown that circulators at the input and the output of the DUT provided the most reliable measurements. Furthermore, based on the de-embedding technique proposed by Belostotski an expression was derived by which the differential noise figure of a three-port device can be de-embedded from two single ended noise figure measurements and it was shown that the differential noise figure of a dLNA equals that of its constituent single ended LNAs. To verify these expressions two differential LNAs were designed, manufactured and measured. The LNA designs discussed in chapter 6 illustrated the viability of implementing a differential LNA using a balanced amplifier topology feeding a 180°-Hybrid coupler and showed that, provided that the insertion loss along the two differential signal paths of the coupler are near equal, the differential gain of the dLNA equals the single ended gain of its constituent single ended LNAs. More importantly, the two designs illustrate the validity of using equation 5.3.10 to de-embed the differential noise figure from two single ended measurements.

It seems as though, despite the lack of definitive definitions and measurement procedures, the signal and noise performance of an L-band differential LNA can be accurately characterised using the methods outlined in this thesis. One thing is certain, the characterisation of differential LNAs at the higher frequency range of the MeerKAT receivers - 8 to 14.5 GHz - will bring forth exciting challenges. The author hopes that the work presented in this thesis would aid in the pursuit of finding alternative techniques by which the nuisance that is noise can be better prevented, cured or endured.

Appendix A

BFG425W Data

A.1 Data Sheet Extracts

Noise data

V_{CE} = 2 V; typical values.

f (MHz)	I_C (mA)	F_{min} (dB)	Γ_{mag}	Γ_{angle}	r_n (Ω)
900	1	0.7	0.67	19.1	0.40
	2	0.8	0.48	17.8	0.27
	4	1	0.28	11.7	0.24
	10	1.4	0.02	–63.9	0.19
	15	1.6	0.11	–162.4	0.18
	20	1.9	0.19	–165.5	0.18
	25	2.1	0.25	–166.3	0.19
	30	2.3	0.29	–166.5	0.19
2000	1	1.3	0.56	57.5	0.36
	2	1.2	0.43	57.2	0.25
	4	1.2	0.22	60.8	0.18
	10	1.6	0.06	137.4	0.19
	15	1.9	0.13	–162.1	0.20
	20	2.2	0.17	–155.5	0.20
	25	2.5	0.22	–152.2	0.21
	30	2.8	0.27	–150.8	0.25

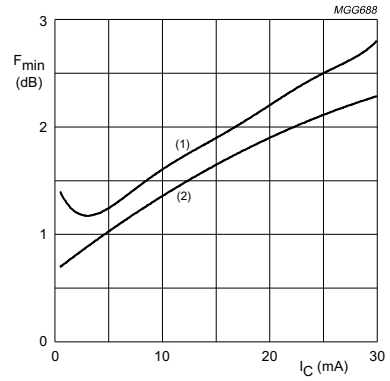

(1) V_{CE} = 2 V; f = 2 GHz.
(2) V_{CE} = 2 V; f = 900 MHz.

Fig.13 Minimum noise figure as a function of the collector current; typical values.

SPICE parameters for the BFG425W die

SEQUENCE No.	PARAMETER	VALUE	UNIT
1	IS	47.17	aA
2	BF	145.0	–
3	NF	0.993	–
4	VAF	31.12	V
5	IKF	304.0	mA
6	ISE	300.2	fA
7	NE	3.000	–
8	BR	11.37	–
9	NR	0.985	–
10	VAR	1.874	V
11	IKR	0.121	A
12	ISC	484.8	aA
13	NC	1.546	–
14	RB	14.41	Ω
15	IRB	0.000	A
16	RBM	6.175	Ω
17	RE	177.9	mΩ
18	RC	1.780	Ω
19 (1)	XTB	1.500	–
20 (1)	EG	1.110	eV
21 (1)	XTI	3.000	–
22	CJE	310.9	fF
23	VJE	900.0	mV
24	MJE	0.346	–
25	TF	4.122	ps
26	XTF	68.20	–
27	VTF	2.004	V
28	ITF	1.525	A
29	PTF	0.000	deg
30	CJC	137.7	fF
31	VJC	556.9	mV
32	MJC	0.207	–
33	XCJC	0.500	–
34 (1)	TR	0.000	ns
35 (1)	CJS	667.5	fF
36 (1)	VJS	418.3	mV
37 (1)	MJS	0.239	–
38	FC	0.550	–
39 (2)(3)	C_{bp}	145	fF
40 (2)	R_{sb1}	25	Ω
41 (3)	R_{sb2}	19	Ω

Notes

1. These parameters have not been extracted, the default values are shown.
2. Bonding pad capacity C_{bp} in series with substrate resistance R_{sb1} between B′ and E′.
3. Bonding pad capacity C_{bp} in series with substrate resistance R_{sb2} between C′ and E′.

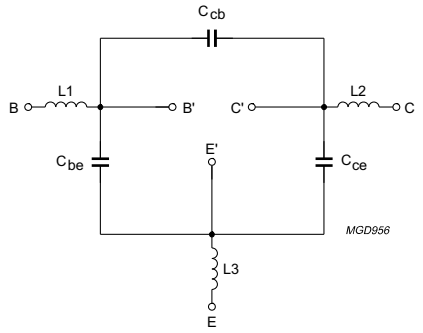

$QL_B = 50$; $QL_E = 50$; $QL_{B,E}(f) = QL_{B,E}\sqrt{(f/f_c)}$
f_c = scaling frequency = 1 GHz.

Fig.14 Package equivalent circuit SOT343R2.

List of components (see Fig.14)

DESIGNATION	VALUE	UNIT
C_{be}	80	fF
C_{cb}	2	fF
C_{ce}	80	fF
L1	1.1	nH
L2	1.1	nH
L3 (note 1)	0.25	nH

Note

1. External emitter inductance to be added separately due to the influence of the printed-circuit board.

A.2 Touchstone Data

```
                                    BFG425W
! Filename: 25bfg425.001
! BFG425W Field C1
! V1=8.298E-001V,V2=2.000E+000V, I1=6.614E-005A, I2=5.000E-003A
# GHz   S   MA   R 50
!              S11              S21              S12              S22
!Freq(GHz)  Mag     Ang      Mag     Ang      Mag     Ang      Mag     Ang
   1.000    0.567 -81.910   10.277 113.589    0.044  47.988    0.720 -44.028
   1.100    0.543 -88.354    9.760 108.883    0.047  45.593    0.691 -46.856
   1.200    0.521 -94.563    9.272 104.380    0.049  43.540    0.663 -49.519
   1.300    0.500 -100.541    8.816 100.164    0.051  41.682    0.637 -51.993
   1.400    0.480 -106.351    8.397  96.144    0.053  40.039    0.612 -54.269
   1.500    0.463 -112.066    7.999  92.308    0.054  38.567    0.590 -56.428
   1.600    0.447 -117.771    7.635  88.594    0.056  37.199    0.569 -58.521
   1.700    0.433 -123.099    7.289  85.040    0.057  35.994    0.549 -60.543
   1.800    0.421 -128.336    6.969  81.649    0.059  34.871    0.530 -62.480
!     DEEMBEDDED NOISE DATA
!FREQUENCY    FMIN    GAMMA OPT        Rn
!  (GHz)      (dB)    Mag    Ang   (NORMALIZED)
1       0.9958  0.4683  10.638  0.34
1.1     1.0204  0.4579  11.795  0.34
1.2     1.0464  0.4471  12.979  0.34
1.3     1.0737  0.4359  14.194  0.34
1.4     1.1022  0.4245  15.444  0.34
1.5     1.1316  0.4128  16.731  0.34
1.6     1.1619  0.4011  18.059  0.34
1.7     1.193   0.3893  19.431  0.34
1.8     1.2247  0.3776  20.852  0.34
```

Appendix B

VMMK1218 Data

B.1 Small Signal Parameters

Parameter	Value	Parameter	Value	Parameter	Value	Parameter	Value
Vd (V)	3	Vd (V)	3	Vd (V)	3	Vd (V)	3
Id (mA)	5	Id (mA)	10	Id (mA)	15	Id (mA)	20
Gm	0.1112	Gm	0.193	Gm	0.258	Gm	0.3119
tau	0.00249	tau	0.0025	tau	0.00252	tau	0.002487
Cgs	0.6365	Cgs	0.8786	Cgs	1.08192	Cgs	1.26
Rgs	0.007447	Rgs	0.1353	Rgs	0.01	Rgs	0.0271
Cgd	0.06521	Cgd	0.0582	Cgd	0.053	Cgd	0.04772
Cds	0.1603	Cds	0.1595	Cds	0.1601	Cds	0.1595
Rds	438.90	Rds	260.60	Rds	209.10	Rds	172.90

B.2 Scattering and Noise Parameters

VMMK-1218 Typical Scattering Parameters and Noise Parameters, T_A=25°C, Vds=3V, Ids=20mA [1]

Freq	S11		S21			S12		S22		MSG/MAG
GHz	Mag.	Ang.	dB	Mag.	Ang.	Mag.	Ang.	Mag.	Ang.	dB
2	0.90	-78.41	20.88	11.07	129.30	0.05	44.78	0.59	-45.41	29.71
3	0.85	-106.62	19.27	9.19	111.50	0.06	29.68	0.50	-61.56	26.11
4	0.82	-129.23	17.67	7.65	96.89	0.07	17.84	0.43	-74.78	23.29
5	0.80	-146.90	16.21	6.47	84.82	0.07	8.51	0.38	-85.37	21.29
6	0.79	-161.57	14.90	5.56	74.28	0.07	0.60	0.35	-94.96	19.70
7	0.78	-173.94	13.71	4.85	64.67	0.07	-6.02	0.32	-103.77	18.32
8	0.78	175.49	12.63	4.28	55.85	0.07	-12.05	0.31	-112.18	17.17
9	0.78	166.35	11.62	3.81	47.60	0.07	-17.59	0.30	-120.67	16.14
10	0.78	158.10	10.70	3.43	39.76	0.07	-22.09	0.29	-128.21	15.23
11	0.79	150.68	9.87	3.11	32.39	0.07	-26.72	0.29	-135.58	14.44
12	0.79	143.93	9.09	2.85	25.16	0.07	-30.99	0.30	-142.88	13.76
13	0.79	137.47	8.38	2.62	18.21	0.07	-34.81	0.31	-149.97	13.11
14	0.80	131.33	7.71	2.43	11.48	0.06	-38.24	0.31	-156.46	12.54
15	0.80	125.54	7.11	2.27	4.87	0.06	-40.97	0.33	-162.44	12.02
16	0.80	119.64	6.53	2.12	-1.87	0.06	-44.55	0.34	-168.20	11.55
17	0.81	113.80	6.00	2.00	-8.47	0.06	-46.49	0.35	-174.07	11.14
18	0.81	108.24	5.48	1.88	-14.69	0.06	-49.45	0.36	-179.63	10.72

Typical Noise Parameters

Freq	Fmin	Γ opt	Γ opt	Rn/50	Ga
GHz	dB	Mag.	Ang.		dB
2	**0.16**	**0.72**	**30.40**	**0.10**	**20.29**
3	0.23	0.62	45.50	0.10	18.62
4	0.30	0.53	60.30	0.09	17.08
5	0.37	0.45	74.80	0.08	15.69
6	0.44	0.39	89.10	0.08	14.44
7	0.50	0.34	103.00	0.07	13.34
8	0.57	0.30	116.70	0.07	12.37
9	0.64	0.28	130.10	0.07	11.55
10	0.71	0.27	143.20	0.06	10.87
11	0.77	0.27	156.00	0.06	10.34
12	0.84	0.29	168.60	0.06	9.95
13	0.91	0.31	-179.20	0.06	9.70
14	0.98	0.36	-167.20	0.06	9.59
15	1.05	0.41	-155.50	0.06	9.63
16	1.11	0.48	-144.10	0.07	9.81
17	1.18	0.56	-132.90	0.08	10.13

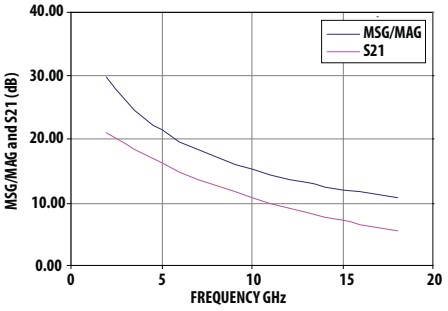

Figure 14. MSG/MAG and S21 vs. Frequency at 3V 20 mA

Note:
1. S-parameters are measured in 50 Ohm test environment.

Appendix C

Narrowband Hybrid Coupler Design

At the time of this work Stellenbosch university could manufacture Printed Circuit Boards (PCBs) using either an etching or milling process. For the etching process, a monochrome image of the layout is printed and transferred to the copper surface of the board using a negative dry film photoresist. The dry film photoresist is placed over the copper surface and exposed to ultraviolet light, polymerising the photoresist. The board is then soaked in developer (washing soda) leaving resist on only the copper exposed to the ultraviolet light. The board is then spray etched using ammonium persulphate and phosphoric acid mixed with a catalyst as etchant [52]. The milling process on the other hand is far less labour intensive. Layouts are exported as a Gerber - indicating the copper regions - and an NC-Drill file, that contains the positions of all the vias and holes as well as their diameters. These files are imported into Circuit CAM which generates milling and drilling data that can be interpreted by LPKF BoardMaster, the software package that controls the milling machine (LPKF S62). Once the milling and drilling data of the layout is available in BoardMaster, the LPKF S62 is loaded with the required drill bits - as indicated in BoardMaster. The LPKF S62 then removes the unwanted copper from the board along the milling paths set up in BoardMaster, each time selecting the required milling bit automatically. The narrowband Hybrid coupler design - discussed in chapter 6 - implemented in CST using CPW transmission lines is shown in figure C.1

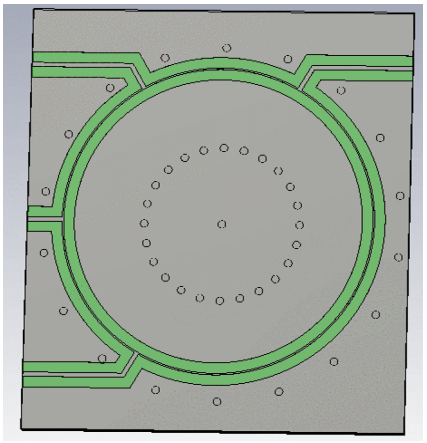

Figure C.1: CPW Hybrid coupler simulated in CST.

Two narrowband Hybrid couplers were manufactured, one etched and one milled. The measured response of these couplers are compared to the simulated response as well as one another in the graphs in figure C.2. The graph in figure C.2(a) shows the normalised phase imbalance measured between output ports 2 and 3 when a signal is applied to the difference port (port 4) - refer to section 6.1.1 for the port designations. Note that an imbalance of 0° indicates that the output signals at ports 2 and 3 are exactly out of phase to one another. Figure C.2(b) compares the amplitude imbalance between ports 2 and 3 for the same excitation.

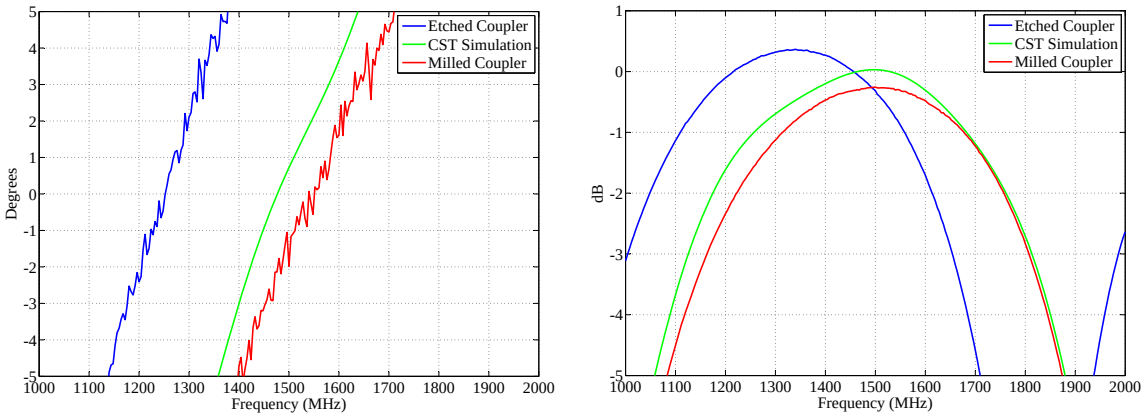

(a) (b)

Figure C.2: Manufactured Hybrid coupler (a) Phase and (b) Amplitude imbalances compared to simulated results.

Consider the phase imbalance of the milled and the etched couplers. The graph indicates that there is a 300 MHz difference in the response of the milled and the etched coupler. Upon investigation it was found that the milling machine had cut approximately 100μm into the substrate.

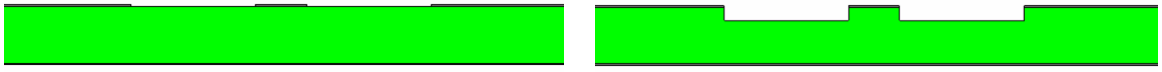

(a) (b)

Figure C.3: Cross sections of (a) Etched and (b) Milled CPW transmission lines.

The effect of this was analysed by simulating a cross section of each of the milled and etched CPW transmission lines using CST. Figure C.3 shows the cross sections of the CPW transmission lines indicating the substrate removed by the milling process (figure C.3(b)). The graph in figure C.4 compares the effective dielectric constant of the milled and etched waveguides.

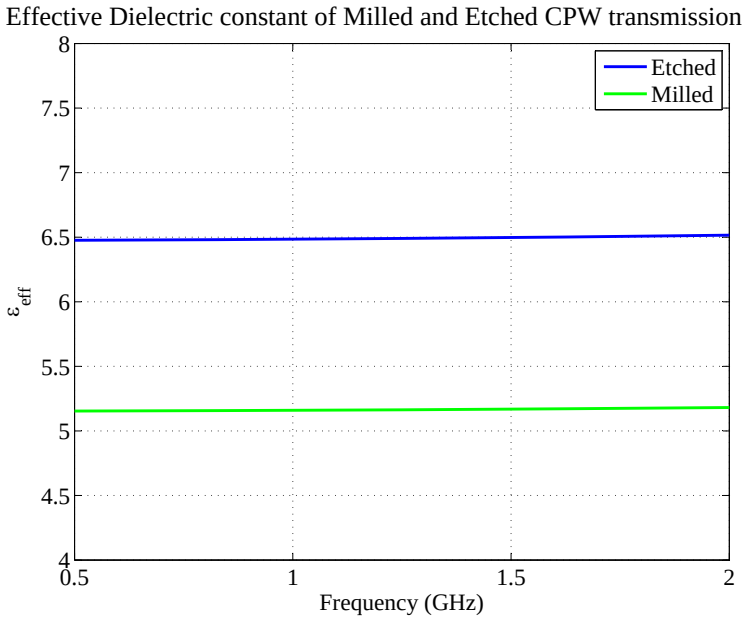

Figure C.4: Simulated effective dielectric constant of etched and milled CPW transmission lines.

As expected, the milling away of the substrate had decreased the effective dielectric constant of the guide, thereby increasing the guided wavelength at the operating frequency - refer to equation 6.1.32. The quarter wavelength transmission line segments of the milled coupler are therefore shorter than the segments of the etched coupler, in effect increasing the operating frequency as seen in the measured results.

Appendix D

MAAL-010704 Data

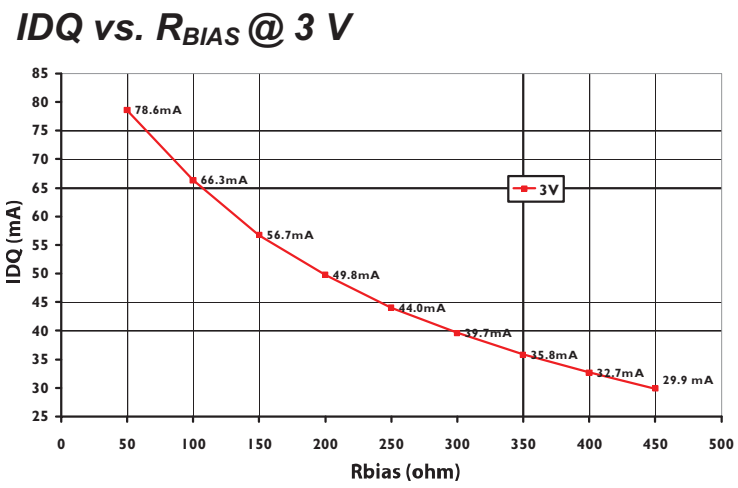

Appendix E

Photos of LNA Designs

E.1 MAAL-010704 Single Ended LNA

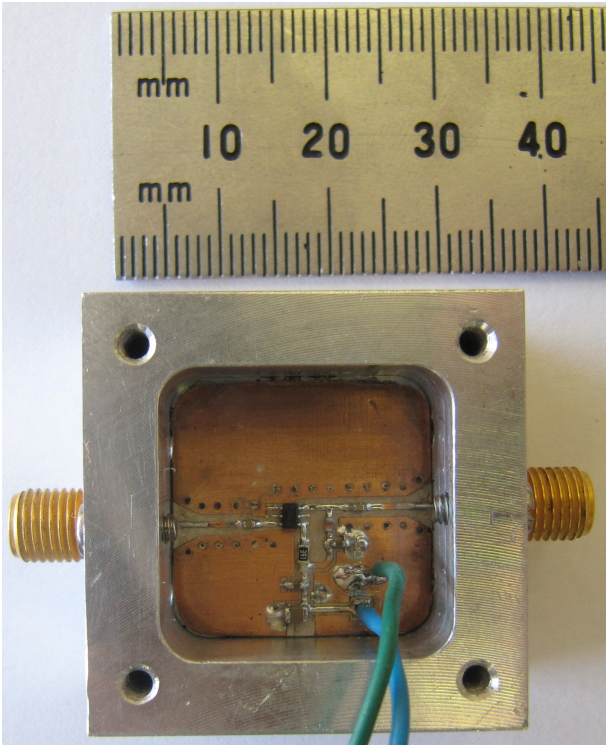

E.2 MAAL-010704 Differential LNA

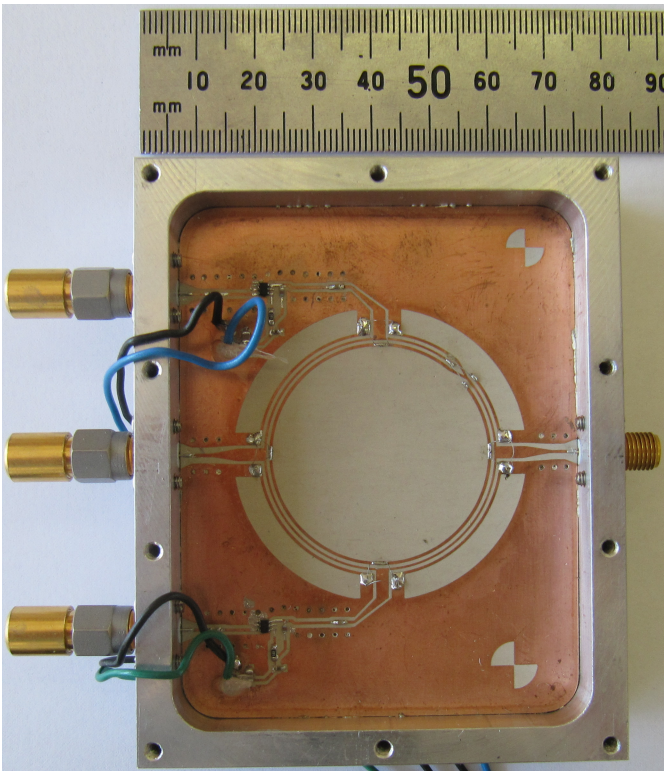

E.3 MGA-16516 Single Ended LNA

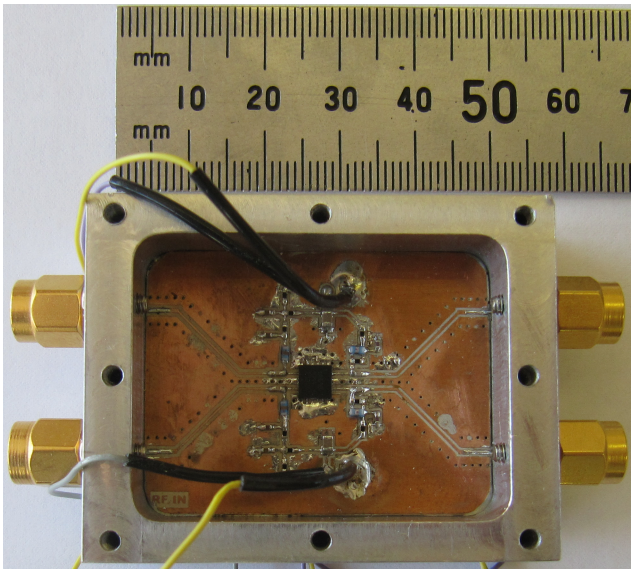

E.4 MGA-16516 Differential LNA

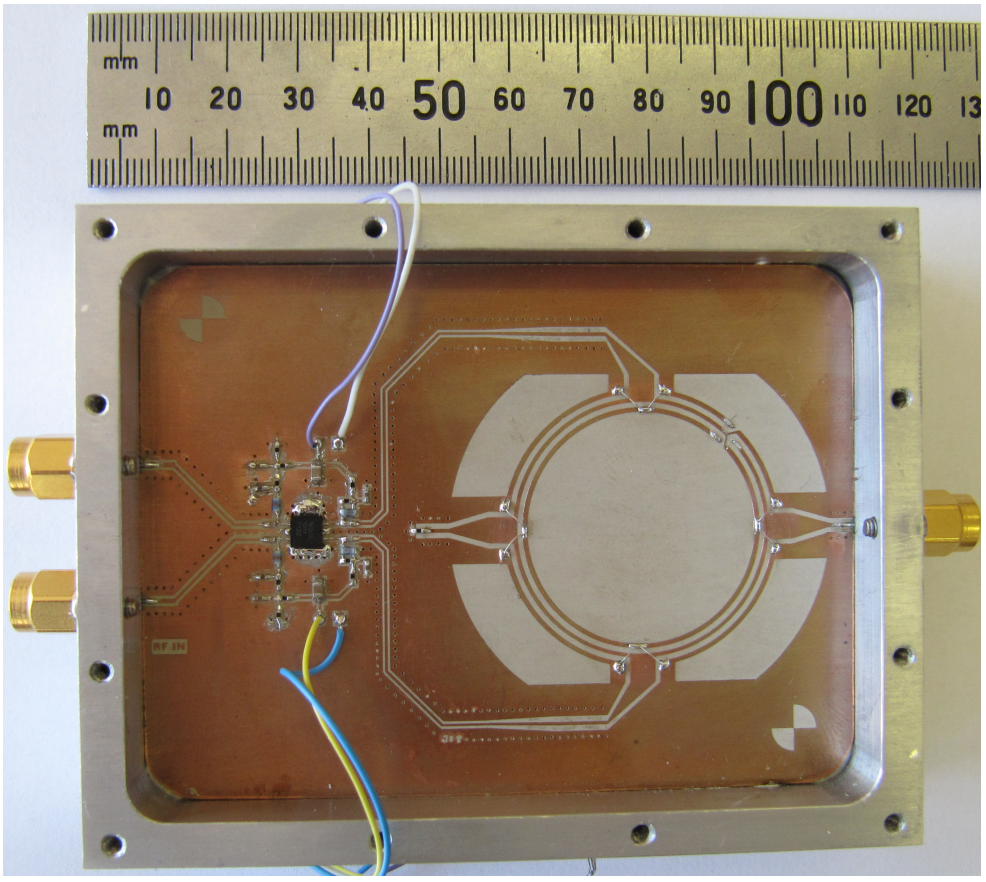

List of References

[1] SPDO. (2011, May) The square kilometer arry fact sheet for industry. [Online]. Available: http://www.skatelescope.org/wp-content/uploads/2011/03/SKA_Factsheet-for-Industry_May2011_web.pdf ix, 2

[2] Agilent, "Fundamentals of rf and microwave noise figure measurement: Application note 57-1," Agilent Technologies, Tech. Rep., 2006. x, 55, 57

[3] L. Tiemeijer, R. Havens, R. de Kort, and A. Scholten, "Improved y-factor method for wide-band on-wafer noise-parameter measurements," *Microwave Theory and Techniques, IEEE Transactions on*, vol. 53, no. 9, pp. 2917 – 2925, sept. 2005. x, 66, 67

[4] A. Abidi and J. Leete, "De-embedding the noise figure of differential amplifiers," *Solid-State Circuits, IEEE Journal of*, vol. 34, no. 6, pp. 882 –885, jun 1999. x, 68, 69

[5] L. Tiemeijer, R. Pijper, and E. van der Heijden, "Complete on-wafer noise-figure characterization of 60-ghz differential amplifiers," *Microwave Theory and Techniques, IEEE Transactions on*, vol. 58, no. 6, pp. 1599 –1608, 2010. x, 4, 71, 104

[6] (2011, January) Meerkat specifications and science. [Online]. Available: http://www.ska.ac.za/meerkat/specsci.php 3

[7] (2011, January) Askap technologies. [Online]. Available: http://www.atnf.csiro.au/projects/askap/technology.html 3, 4

[8] SKA. (2011) Precursors, pathfinders and design studies. [Online]. Available: http://www.skatelescope.org/the-organisation/precursors-pathfinders-design-studies/ 3

[9] O. Garcia-Perez, L. Garcia-Munoz, J. Serna-Puente, V. Gonzalez-Posadas, J. Vazquez-Roy, and D. Segovia-Vargas, "Differential active antennas for the ska project," in *Antennas and Propagation, 2009. EuCAP 2009. 3rd European Conference on*, march 2009, pp. 1316 –1319. 4

[10] J. de Vaate, L. Bakker, E. Woestenburg, R. Witvers, G. Kant, and W. van Cappellen, "Low cost low noise phased-array feeding systems for ska pathfinders," in *Antenna Technology and Applied Electromagnetics and the Canadian Radio Science Meeting, 2009. ANTEM/URSI 2009. 13th International Symposium on*, feb. 2009, pp. 1 –4. 4

[11] D. MacDonald, "The brownian movement and spontaneous fluctuations of electricity," *Res. Appl. in Industry*, vol. 1, pp. 194–203, 1948. 6, 8

[12] B. Oliver, "Thermal and quantum noise," *Proceedings of the IEEE*, vol. 53, no. 5, pp. 436 – 454, may 1965. 6, 8

[13] J. B. Johnson, "Electronic noise: the first two decades," *Spectrum, IEEE*, vol. 8, no. 2, pp. 42 –46, feb. 1971. 6, 8

[14] J. Ragazzini and S. Chang, "Noise and random processes," *Proceedings of the IRE*, vol. 50, no. 5, pp. 1146 –1151, may 1962. 7

[15] D. Pozar, *Microwave Engineering*, 3rd ed. John Wiley & Sons, Inc., 2005. 8, 33, 45, 47, 57, 83, 86

[16] G. Vasilescu, *Electronic Noise and Interfering Signals: Principles and Applications*. Springer, 2005. 9, 10

[17] J. Motchenbacher, C.D. Connelly, *Low-Noise Electronic System Design*. John Wiley & Sons, Inc., 1993. 9, 10, 11, 20, 21

[18] W. Shockley, "The path to the conception of the junction transistor," *Electron Devices, IEEE Transactions on*, vol. 31, no. 11, pp. 1523 – 1546, nov 1984. 10

[19] A. van der Ziel, "Theory of shot noise in junction diodes and junction transistors," *Proceedings of the IRE*, vol. 43, no. 11, pp. 1639 –1646, nov. 1955. 10

[20] D. Peterson, "Noise performance of transistors," *Electron Devices, IRE Transactions on*, vol. 9, no. 3, pp. 296 –303, may 1962. 10

[21] H. Fukui, "The noise performance of microwave transistors," *Electron Devices, IEEE Transactions on*, vol. 13, no. 3, pp. 329 – 341, mar 1966. 10, 21

[22] A. Van Der Ziel, "Thermal noise in field-effect transistors," *Proceedings of the IRE*, vol. 50, no. 8, pp. 1808 –1812, aug. 1962. 14

[23] ——, "Gate noise in field effect transistors at moderately high frequencies," *Proceedings of the IEEE*, vol. 51, no. 3, pp. 461 – 467, march 1963. 14

[24] R. Pucel, D. Masse, and C. Krumm, "Noise performance of gallium arsenide field-effect transistors," *Solid-State Circuits, IEEE Journal of*, vol. 11, no. 2, pp. 243 – 255, apr 1976. 15, 24

[25] A. Cappy, "Noise modeling and measurement techniques [hemts]," *Microwave Theory and Techniques, IEEE Transactions on*, vol. 36, no. 1, pp. 1 –10, jan 1988. 15

[26] H. Fukui, "Design of microwave gaas mesfet's for broad-band low-noise amplifiers," *Microwave Theory and Techniques, IEEE Transactions on*, vol. 27, no. 7, pp. 643 – 650, jul 1979. 15

[27] M. Pospieszalski, "Modeling of noise parameters of mesfets and modfets and their frequency and temperature dependence," *Microwave Theory and Techniques, IEEE Transactions on*, vol. 37, no. 9, pp. 1340 –1350, sep 1989. 15, 30

[28] ——, "Interpreting transistor noise," *Microwave Magazine, IEEE*, vol. 11, no. 6, pp. 61 –69, oct. 2010. 15

[29] F. Danneville, "Microwave noise and fet devices," *Microwave Magazine, IEEE*, vol. 11, no. 6, pp. 53 –60, oct. 2010. 17

[30] H. Rothe and W. Dahlke, "Theory of noisy fourpoles," *Proceedings of the IRE*, vol. 44, no. 6, pp. 811 –818, june 1956. 17

[31] H. Haus, W. Atkinson, G. Branch, W. Davenport, W. Fonger, W. Harris, S. Harrison, W. McLeod, E. Stodola, and T. Talpey, "Representation of noise in linear twoports," *Proceedings of the IRE*, vol. 48, no. 1, pp. 69 –74, jan. 1960. 18

[32] H. Friis, "Noise figures of radio receivers," *Proceedings of the IRE*, vol. 32, no. 7, pp. 419 – 422, 1944. 18, 58

[33] "Ire standards on methods of measuring noise in linear twoports, 1959," *Proceedings of the IRE*, vol. 48, no. 1, pp. 60 –68, jan. 1960. 18

[34] S. Voinigescu, M. Maliepaard, M. Schroter, P. Schvan, and D. Harame, "A scalable high frequency noise model for bipolar transistors with application to optimal transistor sizing for low-noise amplifier design," in *Bipolar/BiCMOS Circuits and Technology Meeting, 1996., Proceedings of the 1996*, 29 1996, pp. 61 –64. 20, 21

[35] E. Nielsen, "Behavior of noise figure in junction transistors," *Proceedings of the IRE*, vol. 45, no. 7, pp. 957 –963, july 1957. 21

[36] A. Van Der Ziel, "Noise in junction transistors," *Proceedings of the IRE*, vol. 46, no. 6, pp. 1019 –1038, june 1958. 21

[37] H. Cooke, "Microwave transistors: Theory and design," *Proceedings of the IEEE*, vol. 59, no. 8, pp. 1163 – 1181, aug. 1971. 21

[38] G. Dambrine, H. Happy, F. Danneville, and A. Cappy, "A new method for on wafer noise measurement," *Microwave Theory and Techniques, IEEE Transactions on*, vol. 41, no. 3, pp. 375 –381, mar 1993. 21

[39] H. Hillbrand and P. Russer, "An efficient method for computer aided noise analysis of linear amplifier networks," *Circuits and Systems, IEEE Transactions on*, vol. 23, no. 4, pp. 235 – 238, apr 1976. 32

[40] G. D. Vendelin, A. Pavio, and U. Rohde, *Microwave Circuit Design Using Linear and Nonlinear Techniques*, 2nd ed. John Wiley & Sons, Inc., 2005. 34, 37

[41] V. Rizzoli and A. Lipparini, "Computer-aided noise analysis of linear multiport networks of arbitrary topology," *Microwave Theory and Techniques, IEEE Transactions on*, vol. 33, no. 12, pp. 1507 – 1512, Dec. 1985. 39

[42] D. Bockelman and W. Eisenstadt, "Combined differential and common-mode scattering parameters: theory and simulation," *Microwave Theory and Techniques, IEEE Transactions on*, vol. 43, no. 7, pp. 1530 –1539, Jul. 1995. 45, 47, 49

[43] V. Tripathi, "Asymmetric coupled transmission lines in an inhomogeneous medium," *Microwave Theory and Techniques, IEEE Transactions on*, vol. 23, no. 9, pp. 734 – 739, sep 1975. 48

[44] S. Cohn, "Shielded coupled-strip transmission line," *Microwave Theory and Techniques, IRE Transactions on*, vol. 3, no. 5, pp. 29 –38, 1955. 48

[45] Y. Zhou and Y. Chen, "Exploration of the properties of the mixed-mode s-parameters," in *Microwave and Millimeter Wave Technology, 2008. ICMMT 2008. International Conference on*, vol. 1, 2008, pp. 25 –28. 51

[46] A. Davidson, B. Leake, and E. Strid, "Accuracy improvements in microwave noise parameter measurements," *Microwave Theory and Techniques, IEEE Transactions on*, vol. 37, no. 12, pp. 1973 –1978, dec 1989. 65, 66, 67

[47] L. Belostotski and J. Haslett, "A technique for differential noise figure measurement of differential lnas," *Instrumentation and Measurement, IEEE Transactions on*, vol. 57, no. 7, pp. 1298 –1303, july 2008. 73

[48] J. Reed and G. Wheeler, "A method of analysis of symmetrical four-port networks," *Microwave Theory and Techniques, IRE Transactions on*, vol. 4, no. 4, pp. 246 –252, october 1956. 86

[49] S. March, "A wideband stripline hybrid ring (correspondence)," *Microwave Theory and Techniques, IEEE Transactions on*, vol. 16, no. 6, p. 361, jun 1968. 91

[50] C.-H. Ho, L. Fan, and K. Chang, "New uniplanar coplanar waveguide hybrid-ring couplers and magic-t's," *Microwave Theory and Techniques, IEEE Transactions on*, vol. 42, no. 12, pp. 2440 –2448, dec 1994. 92

[51] T. Wang and K. Wu, "Size-reduction and band-broadening design technique of uniplanar hybrid ring coupler using phase inverter for m(h)mic's," *Microwave Theory and Techniques, IEEE Transactions on*, vol. 47, no. 2, pp. 198 –206, feb 1999. 93

[52] R. Khandpur, *Printed Circuit Boards Design, Fabrication and Assembly*. McGraw-Hill, 2006. 128